



Report No.: CSM/MT/CWJCR/010/018

FINAL PROJECT REPORT

**Measurement of the Effect of Magnetization on
Hydrogen Cracking Susceptibility of Pipeline Steels**

*Contract Number: DTPH56-06-T-000019
CSM Project No. 4-42928*

Submitted to

MICHAEL ELSE
Bureau of Ocean Energy Management, Regulation, and Enforcement
US DEPARTMENT OF THE INTERIOR
Technology Assessment and Research Branch
381 Elden St., MS 4700
Herndon, VA 20170-4817

[Performance Period: September 1, 2008 – August 31, 2010]



Submitted by
**John Roubidoux
Brajendra Mishra
David L. Olson**

**CENTER FOR WELDING, JOINING & COATINGS RESEARCH
DEPARTMENT OF METALLURGICAL & MATERIALS ENGINEERING
DECEMBER 2010**

The view, opinions, and/or findings contained in this report are those of the author(s) and should not be construed as an official Government position, policy or decision, unless so designated by other documentation.

HIGHLIGHTS

The integrity of pipelines is monitored using intelligent inspection tools (known as intelligent pigs). The material state of a pipeline is assessed by determining the localized magnetic flux leakage (MFL). The MFL technique is performed by magnetizing the steel pipe near the saturation flux density and then detecting a local flux leakage caused by surface anomalies. In addition to magnetic fields, electric fields are often present due to cathodic protection currents, which are utilized in many pipelines to decrease the corrosion rate.

In this study, the effect of a magnetic field on the hydrogen absorption and corrosion behavior of API X80, X70, and X52 linepipe steel grades was analyzed. The purpose of this work was to determine the fundamental mechanisms by which a magnetic field alters the corrosion and hydrogen absorption behavior of these steels. In the original work by Sanchez (2005), a constant magnetic field strength of 2.0 Tesla was used. However, in this research, three magnetic field strengths were used: 0.0, 0.3, 0.5, and 0.7 Tesla. These magnetic field strengths were chosen based upon experimental measurements made in the field at the Battelle pipeline research facility in Ohio. From these experiments, it was determined that the remnant magnetic field strength was approximately 0.3-0.6 Tesla. The main results from this work are the following:

- (1) Hydrogen content increases with increasing magnetic field strength (see Figure 4.5)**
- (2) A magnetic field alters the kinetics of the system (see Figure 5.23)**
- (3) Cathodic hydrogen charging in the presence of a magnetic field results in passive film formation (see Figure 5.11)**
- (4) Thermodynamic model is presented in Chapter 5**
- (5) Magnetic field enhances mass transport to the electrode surface as shown in Chapter 6**
- (6) Magnetic field alters the corrosion behavior of X80, X70, and X52 by shifting the passivation potential in the positive direction causing delayed passivation and, therefore, an increase in corrosion susceptibility.**
- (7) Hydrogen absorption under magnetism leads to increased surface pitting and hydrogen cracking**

Further Required Work

There are four main areas of this research that need to be further investigated more thoroughly to provide the guidelines for industry:

- (1) Quantification of the formation of passive films at cathodic potentials.**
- (2) Quantification of the effect of magnetic field on electrode kinetics.**
- (3) Development of protocol for the industry for *insitu* measurement of hydrogen and magnetic field remanence.**
- (4) Development of procedure to mitigate generation of remnant magnetic fields in pipelines.**

These additional tasks will require two years of concentrated research effort.

EXECUTIVE SUMMARY

The integrity of pipelines is monitored using intelligent inspection tools (known as intelligent pigs). The material state of a pipeline is assessed by determining the localized magnetic flux leakage (MFL). The MFL technique is performed by magnetizing the steel pipe near the saturation flux density and then detecting a local flux leakage caused by surface anomalies. In addition to magnetic fields, electric fields are often present due to cathodic protection currents, which are utilized in many pipelines to decrease the corrosion rate.

In this study, the effect of a magnetic field on the hydrogen absorption and corrosion behavior of API X80, X70, and X52 linepipe steel grades was analyzed. The purpose of this work was to determine the fundamental mechanisms by which a magnetic field alters the corrosion and hydrogen absorption behavior of these steels. The conditions that a pipeline experiences in the field were simulated in a laboratory setting using permanent magnets and cathodic potentials. Two one Tesla permanent magnets were used to simulate the remanent magnetic field present in a pipeline after a pigging operation. The cathodic protection return currents were simulated by polarizing the working electrode (steel sample) to cathodic potentials. Using experimental electrochemical methods and theoretical modeling, it was found that a magnetic field changes the passivation behavior, shifts the corrosion potential to more anodic potentials, and increases the total absorbed hydrogen content.

Potentiodynamic polarization experiments were performed in the presence of a magnetic field to show that a magnetic field acts to shift the passivation potential and the corrosion potential to more anodic values. The shift in passivation potential of API X80 is due to magneto-convection. Magneto-convection is a result of three forces: Lorentz force, concentration gradient force, and magnetic field gradient force. These three forces increase mass transport to and from the metal/electrolyte interface and act to eliminate concentration gradients in the diffusion layer next to the electrode.

At the corrosion potential (open circuit potential) there is no current flowing, and the shift in corrosion potential due to a magnetic field is a purely thermodynamic phenomenon. A thermodynamic model, which is based on the Nernst equation, is given to account for the potential shift. The thermodynamic model accounts for the shift in potential by the addition of a magnetic work term onto the Nernst equation.

Electrochemical impedance spectroscopy (EIS) experiments were performed in the presence of a magnetic field to show that the charge transfer resistance increases with increasing magnetic field strength and the double layer capacitance decreases with increasing magnetic field strength. The EIS experiments also show one high frequency capacitive loop which is indicative of a charge transfer reaction and cathodic film formation. Evidence of cathodic film formation from the EIS experiments is an important result, since it is believed that the formation of a cathodic film is responsible for erratic hydrogen charging results. The EIS spectra were modeled using an equivalent circuit model with a constant phase element (CPE).

Three different types of cathodic hydrogen charging experiments were performed: (1) variation in time at a constant magnetic field strength, (2) variation in stress level, and (3) variation in magnetic field strength at constant time. From the hydrogen charging experiments it was found that the hydrogen content increases with increasing magnetic field strength. The increase in hydrogen content is attributed to an increase in the magnetostatic energy of the steel.

Lastly, theoretical modeling was done to show the effect of a magnetic field on mass transport. Two models were developed to model the fluid flow and mass transport next to a vertical electrode in the presence of magnetic field. Both models are based upon the boundary layer equations for magnetohydrodynamics; however, the solutions to the boundary layer equations are obtained by two different methods. The first solution method used was the Adomian decomposition method (ADM) and the second solution method was scaling analysis. The modeling results show that a magnetic field enhances mass transport to the metal/electrolyte interface and that as the magnetic field strength increases so too does the mass transport.

In Chapter 1 of this Final Report, a review of prior work performed at the Colorado School of Mines on the subject of magnetism, hydrogen absorption, and corrosion of API X80, X70, and X52 steel grades will be given. In addition, a literature review of magneto-electrochemistry, magnetocorrosion, and magnetohydrodynamics will be given.

The purpose of Chapter 2 is to present the experimental observations, and state the problem to be solved. Throughout the course of this project many experimental observations have been made. The interaction of the magnetic field with the electric current generates magnetohydrodynamic forces which manifest in three forms; the Lorentz force, the concentration gradient force, and the magnetic field gradient force. These three forces act upon the species in the electrolyte which lead to complex fluid motion and electrochemical phenomena.

Chapter 3 presents the experimental materials that were used for this investigation and the various experimental techniques employed for this research work. Experimental techniques include potentiostatic methods (cathodic hydrogen charging), electrochemical impedance

spectroscopy (EIS), and potentiodynamic polarization. Lastly, an analytical mathematical modeling technique known as Adomian Decomposition Method (ADM) is presented and discussed.

In Chapter 4 the results for the hydrogen charging experiments are presented and discussed. Cathodic hydrogen charging experiments were performed on API X80, X70, and X52 linepipe steel with and without a magnetic field present in the electrochemical cell. Time, magnetic field strength, and stress were varied to determine their effect on hydrogen absorption. The first series of hydrogen charging experiments were performed on API steel grades X80, X70, and X52 at a magnetic field strength of 0.7 Tesla and the time was varied from two to twelve hours. API X80 linepipe steel was the only steel grade examined for the variation in magnetic field strength experiments and the stress experiments. For the variation in magnetic field strength experiments, the magnetic field was varied from 0.0 to 0.7 Tesla. Each API X80 linepipe steel specimen was charged for two hours at their respective field strength. For the stress effect experiments, API X80 linepipe steel E8 tensile samples were stressed to three different levels and then cathodically charged for times ranging from two to twelve hours. The three stress levels were 90 ksi pre-UTS, ultimate tensile strength (UTS), and 90 ksi post-UTS. The total hydrogen content was measured with the LECO Hydrogen Determinator.

In Chapter 5 the experimental results for the corrosion experiments performed in the presence of a magnetic field will be presented and discussed. Two main experimental techniques were used to assess the corrosion behavior of API X80 linepipe steel in the presence of a magnetic field: (1) Potentiodynamic polarization and (2) Electrochemical Impedance Spectroscopy (EIS).

In Chapter 6, three fluid flow models are presented. The models are based upon the boundary layer equations for magnetohydrodynamics. The first model accounts for a nonuniform magnetic field. The second model accounts for coupled fluid flow and mass transport in the boundary layer region of a vertical electrode. In the second model, the magnetic field is assumed constant. The purpose of the first model is two-fold: (1) present and discuss the effects of a magnetic field on the boundary layer structure and velocity profiles, and (2) introduce and discuss some of the finer points of the modeling technique used to solve the transport equation. The purpose of the third model is to derive relationships for the boundary layer thickness and transport correlations which take into account the magnetic field. These relationships are derived by the use of scaling analysis.

Chapter 7 gives the conclusions and recommendations for future work. The driving force behind this project was to gain a fundamental understanding of the effect of a magnetic field on

the hydrogen absorption and corrosion behavior of API X80, X70, and X52 linepipe steel grades. In the original work by Sanchez (2005), a constant magnetic field strength of 2.0 Tesla was used. However, in this research, three magnetic field strengths were used: 0.0, 0.3, 0.5, and 0.7 Tesla. These magnetic field strengths were chosen based upon experimental measurements made in the field at the Battelle pipeline research facility in Ohio. From these experiments, it was determined that the remanent magnetic field strength was approximately 0.3 Tesla. The main results from this work are the following: (1) Hydrogen content increases with increasing magnetic field strength see Figure 4.5; (2) A magnetic field alters the kinetics of the system see Figure 5.23; (3) Cathodic hydrogen charging in the presence of a magnetic field results in passive film formation; see Figure 5.11 and the thermodynamic model presented in Chapter 5; (4) a magnetic field enhances mass transport to the electrode surface as shown in Chapter 6 and (5) a magnetic field alters the corrosion behavior of X80, X70, and X52 by shifting the passivation potential.

TABLE OF CONTENTS

CHAPTER 1 INTRODUCTION AND LITERATURE REVIEW	1
1.1 Overview.....	1
1.2 Review of Prior Work.....	1
1.2.1 Results of Initial Work	2
1.2.2 Thermodynamic Model	2
1.2.3 Experimental Hydrogen Charging Results	4
1.2.4 Theoretical Explanation for Increased Hydrogen Absorption in a Magnetic Field	5
1.2.5 Results for the Magnetization Effect on Hydrogen Concentration and Coldwork	6
1.2.6 Results for the Magnetization Effect on Hydrogen Induced Cracking...	7
1.2.7 Conclusions Determined by Initial Hydrogen Absorption Research	8
1.3 Review of Magnetic Field Effects on Magnetocorrosion	9
1.3.1 Thermodynamics of Magnetocorrosion.....	10
1.3.2 Kinetics of Magnetocorrosion.....	11
1.4 Magnetochemistry	13
1.4.1 Magnetochemistry (MHD).....	14
1.4.1.1 Important Parameters of MHD	14
1.4.1.2 Governing Equations of MHD.....	15
1.4.2 Magnetochemical Forces.....	16
1.4.3 The Effect of Magnetism on Mass Transport and Electrodeposition ...	18
1.4.3.1 The Effect of Magnetism on Mass Transport	18
1.4.3.2 The Effect of Magnetism on Electrodeposition	22
CHAPTER 2 EXPERIMENTAL OBSERVATIONS AND STATEMENT OF PROBLEM TO BE SOLVED	24
2.1 Introduction.....	24
2.2 The Effect of a Magnetic Field on the Open Circuit Potential (OCP).....	24

2.3 Erratic Hydrogen Charging Results with a Magnetic Field	26
2.4 The Effect of a Magnetic Field on Film Formation.....	28
2.5 Enhanced Pitting and Cracking Behavior with a Magnetic Field.....	32
2.6 Electrolyte Stirring with a Magnetic Field.....	33
2.7 The Effect of a Magnetic Field on Passivation Behavior.....	36
2.7.1 Polarization Results for X52, X70, and X80	38
2.8 Research Problem to be Solved.....	41
CHAPTER 3 EXPERIMENTAL METHODS AND MATERIALS	43
3.1 Introduction.....	43
3.2 Experimental Materials.....	43
3.3 Hydrogen Charging Environment	45
3.3.1 Solution Concentration Calculations	46
3.4 Electrochemical Cell.....	47
3.4.1 Magnet Towers	47
3.4.2 Reference Electrode	49
3.4.3 Counter Electrode (Anode).....	49
3.4.4 Working Electrode (Cathode).....	49
3.5 Cathodic Hydrogen Charging Experiments	49
3.5.1 Hydrogen Charging: Variation in Magnetic Field Strength.....	51
3.5.2 Hydrogen Charging: The Effect of Stress on Hydrogen Absorption ...	52
3.6 Potentiodynamic Polarization Experiments	53
3.7 Electrochemical Impedance Spectroscopy Experiments.....	54
3.8 Adomian Decomposition Method	54
CHAPTER 4 RESULTS AND DISCUSSION: HYDROGEN CHARGING	57
4.1 Introduction.....	57
4.2 Hydrogen Charging Results for API X80, X70, and X52 Linepipe Steel Grades	57
4.3 Hydrogen Charging Experiments: Stress Effects	60
4.4 Hydrogen Charging Experiments: Magnetic Field Effects	61

4.5 Discussion: Hydrogen Charging Results	62
4.5.1 Hydrogen Absorption Mechanism	62
4.5.2 Magnetic Forces Present in the Electrolyte	65
4.5.3 Cathodic Film Formation.....	67
CHAPTER 5 RESULTS AND DISCUSSION: ELECTROCHEMICAL CORROSION STUDIES FOR X80	69
5.1 Introduction.....	69
5.2 Corrosion Studies: Potentiodynamic Polarization Experiments.....	69
5.3 Corrosion Studies: Electrochemical Impedance Spectroscopy (EIS)	74
5.4 Discussion: Potentiodynamic Polarization Experiments	78
5.4.1 Magnetic Field Effects on the Open Circuit Potential (OCP).....	79
5.4.2 Magnetic Field Effects on the Limiting Current Density	81
5.4.3 Magnetic Field Effects on the Passivation Potential	84
5.4.3.1 Model for Passivation Potential Shift	85
5.5 Discussion: Electrochemical Impedance Spectroscopy Experiments.....	89
5.5.1 Review of Electrochemical Impedance Spectroscopy.....	90
5.5.2 Interpretation of Impedance Spectra	92
5.5.3 Equivalent Circuit Modeling of the Experimental EIS Spectra	94
5.6 Summary and Concluding Remarks	106
CHAPTER 6 RESULTS AND DISCUSSION: MAGNETOHYDRODYNAMIC FLUID FLOW MODEL.....	107
6.1 Introduction.....	107
6.2 Mathematical Formulation for a Nonuniform Magnetic Field.....	107
6.2.1. Solution by Adomian Decomposition Method (ADM)	109
6.2.2. Pade Approximants and Boundary Conditions at Infinity	112
6.3 Coupled Fluid Flow and Mass Transport at a Vertical Electrode.....	120
6.3.1 Mathematical Formulation of the Coupled Model	121
6.4 Solution by Adomian Decomposition Method.....	124
6.4.1. Pade Approximants for a Coupled System of Equations.....	128

6.5 Scaling Analysis	131
6.5.1. Coupled Fluid Flow and Mass Transport	131
6.5.2. Mathematical Formulation of the Scaling Solution.....	132
6.6 Discussion of the Modeling Results	135
6.6.1 Discussion of Nonlinearly Varying Magnetic Field Model.....	135
6.6.2 Discussion of the Coupled fluid flow and Mass Transport Model.....	137
6.6.3 Discussion of the Scaling Analysis Model	138
CHAPTER 7 CONCLUSIONS AND FUTURE WORK	140
7.1 Introduction	140
7.2 Answers to Guiding Questions	140
7.3 Future Work	147
REFERENCES CITED.....	150

LIST OF FIGURES

Figure 1.1 Schematic plot of Equation 2.8. The slope of the line is a material property; the y-intercept is the concentration of hydrogen in the steel without a magnetic field.....	4
Figure 1.2 Comparison plot of steel grades X52, X70, and X80 with and without a magnetic field.....	5
Figure 1.3 Plot of hydrogen concentration as a function of bending angle for X80 linepipe steel. The bottom region is a region of non-magnetization and the upper region in the plot is a region of magnetization.....	7
Figure 1.4 Schematic of Helmholtz double layer, Gouy-Chapman layer, and the Larmor loop effect from combined electrical and magnetic fields, Jackson (2008).....	12
Figure 1.5 Schematic Evans diagram indicating increased hydrogen production and corrosion current due to cathodic protection and Helmholtz-Layer-controlled effects on hydrogen content, Jackson (2008).....	13
Figure 1.6 Cathode-magnetic field orientations studied by Mori et al. (2002). Their work showed that the mass transport effects caused by the magnetic field had strong orientation dependence.....	19
Figure 1.7 Plot of Sherwood number as a function of magnetic mass transfer enhancement factor.....	20
Figure 2.1 Open circuit potential measurements for X80 linepipe steel grade with and without a magnetic field. The quantity ΔV_M is the difference in open circuit potential after two hours of immersion in 1 N H_2SO_4 solution.....	25
Figure 2.2 Schematic Pourbaix diagram for the iron-water system. The blue arrow indicates the direction in which the potential can shift when a magnetic field is applied to the system. A strong magnetic field could push the potential into region A (passive film formation), while a weak magnetic field could shift the potential into region C (active corrosion), and region D would be no magnetic field (immunity).....	29
Figure 2.3 Schematic representation of an Evans diagram for the iron-water system. The black lines represent the original iron and hydrogen lines and the blue lines represent the iron and hydrogen lines shifted by the application of a magnetic field.....	30
Figure 2.4 SEM image of X100 steel that was charged in a magnetic field. The image depicts cracking of the passivating film.....	31
Figure 2.5 SEM image of X100 steel showing cracks in the passivating film. The crack in the film would give regions of increased current density and therefore increased hydrogen absorption.....	32
Figure 2.6 SEM image of X70 linepipe steel showing pitting and cracking behavior.....	33

Figure 2.7 Bubble flow pattern without a magnetic field. The bubbles nucleated at the bottom of the steel sample and followed vertical flow path. There are no magnetic forces to alter the bubble trajectory.	34
Figure 2.8 Schematic representation of the experimentally observed bubble flow with a magnetic field present in the electrochemical cell. When a magnetic field is present in the cell two distinct zones are present; stir zone and a non-stir zone.	34
Figure 2.9 Schematic of metal surface with different diffusion layer thicknesses. δ represents the diffusion layer thickness. The bottom curve in the schematic represents the diffusion layer thickness without a magnetic field. The top curve represents the diffusion layer thickness when the magnetic field is applied.	35
Figure 2.10 Schematic representation of a potentiodynamic polarization curve (anodic branch) for iron in a buffered solution of $\text{pH} = 7$. The letters (A – E) correspond to the electrochemical reactions given above, Stansbury et al. (2000).	38
Figure 2.11 Potentiodynamic polarization curve for X80 linepipe steel with and without a magnetic field 1 N H_2SO_4	40
Figure 2.12 Potentiodynamic polarization curve for X52 linepipe steel with and without a magnetic field 1 N H_2SO_4	40
Figure 2.13 Potentiodynamic polarization curve for X70 linepipe steel with and without a magnetic field 1 N H_2SO_4	41
Figure 3.1 API X52 linepipe steel micrograph showing ferritic microstructure with small islands of peralite at the grain boundaries.	44
Figure 3.2 API X70 linepipe steel micrograph showing a fine-grained microstructure.	44
Figure 3.3 API X80 linepipe steel micrograph showing an irregular fine-grained ferritic microstructure.	45
Figure 3.4 Magnet tower assembly, each magnet tower produces a magnetic field strength of 1.0 T. (a) the overall height of an individual magnet tower is two inches. Each tower consists of a 2 inch x 2 inch x 1 inch (50.8 mm x 50.8 mm x 25.4 mm) base and a 2 inch x 2 inch x 1 inch (50.8 mm x 50.8 mm x 25.4 mm) pyramid. (b) Top view of the magnet towers. (c) View of the magnet stack used to bring the magnetic field strength to 1.0 T. (d) The two magnet towers separated by a piece of PVC. The PVC was used to achieve the desired field strength of 0.7 T. Changing the length of the PVC separator will change the strength of the magnetic field. The magnets were isolated from the solution by coating them in a silicone caulking and then in acrylic paint. The poles of the magnet towers, separated by the PVC, were covered in a two-part epoxy resin.	48
Figure 3.5 This figure shows the geometry and dimensions of the hydrogen charging samples. The size of the hydrogen charging sample was dictated by the LECO Hydrogen Determinator. Hydrogen charge samples tested in the LECO cannot have a mass greater than one gram.	50
Figure 3.6 Typical plot for a hydrogen charging experiment. This data shows the current transient for a two hour hydrogen charging experiment on X80 linepipe steel. The magnets were in the electrochemical cell for this experiment.	51

Figure 3.7 The strength of the magnetic field is controlled by changing the length of PVC between the poles of the magnets.	52
Figure 3.8 E8 tensile sample that has been sectioned is on the left of the figure. Below the penny is the hydrogen charging sample. All hydrogen charging samples for the stress experiments were taken from the neck of the tensile sample.	53
Figure 4.1 Hydrogen charging results for API X80 linepipe steel. This plot shows total hydrogen concentration as a function of time. The triangles represent experiments done in the presence of a magnetic field and the black circles are experiments done without a magnetic field.	58
Figure 4.2 Hydrogen charging results for API X70 linepipe steel. This plot shows total hydrogen concentration as a function of time. The triangles represent experiments done in the presence of a magnetic field and the black circles are experiments done without a magnetic field.	59
Figure 4.3 Hydrogen charging results for API X52 linepipe steel. This plot shows total hydrogen concentration as a function of time. The triangles represent experiments done in the presence of a magnetic field and the black circles are experiments done without a magnetic field.	59
Figure 4.4 Comparison plot of all Hydrogen charging results for API X80 linepipe steel. This plot shows total hydrogen concentration as a function of time. All of the stress levels are represented on this plot. The open-circles represent the pre-UTS experiments, the open-squares represent the UTS experiments, and the open-triangles represent the post-UTS experiments.	60
Figure 4.5 Hydrogen charging results for API X80 linepipe steel. This plot shows total hydrogen concentration as a function of magnetic field strength. The magnetic field strengths used for this series of experiments were 0.0, 0.3, 0.5, and 0.7 T. A magnetic field strength of 0.7 T appears to have the largest effect on hydrogen absorption.	61
Figure 4.6 Schematic diagram of the free energy curves associated with an electrochemical reaction; (a) schematic corresponding to equilibrium, (b) schematic corresponding to a more positive potential promoting oxidation, and (c) schematic corresponding to a more negative potential promoting reduction.	64
Figure 4.7 Schematic diagram showing the possible reaction paths for hydrogen absorption into a metal electrode. H_m represents a hydrogen atom that has been absorbed directly into the metal and is free to diffuse into the bulk of the lattice.	65
Figure 4.8 Shift in the open circuit potential when a magnetic field is applied during cathodic hydrogen charging experiments.	68
Figure 4.9 Schematic Pourbaix diagram for the iron-water system. The blue arrow indicates the direction in which the potential can shift when a magnetic field is applied to the system. A strong magnetic field could push the potential into region A (passive film formation), while a weak magnetic field could shift the potential into region C (active corrosion), and region D would be no magnetic field (immunity).	68

Figure 5.1 Potentiodynamic polarization experimental results for API X80 linepipe steel. The solid line represents a polarization experiment performed at a magnetic field strength of 0.0 Tesla and the dashed line represents a polarization experiment performed at a magnetic field strength of 0.3 Tesla.....	70
Figure 5.2 Potentiodynamic polarization experimental results for API X80 linepipe steel. The solid line represents a polarization experiment performed at a magnetic field strength of 0.0 Tesla and the dashed line represents a polarization experiment performed at a magnetic field strength of 0.5 Tesla.....	71
Figure 5.3 Potentiodynamic polarization experimental results for API X80 linepipe steel. The solid line represents a polarization experiment performed at a magnetic field strength of 0.0 Tesla and the dashed line represents a polarization experiment performed at a magnetic field strength of 0.7 Tesla.....	71
Figure 5.4 Potentiodynamic polarization experimental results for API X80 linepipe steel. This plot gives a comparison of the polarization experiments at all magnetic field strengths. The important elements to notice from this plot are the shifts in passivation potential and decrease in limiting current density with applied magnetic field.	72
Figure 5.5 This plot shows the variation in open circuit potential and corrosion current with applied magnetic field.....	72
Figure 5.6 This plot shows the cathodic branch of the potentiodynamic polarization curve. Note the decrease in limiting current density with increasing strength of magnetic field. The largest decrease in limiting current density occurs at a magnetic field strength of 0.7 Tesla..	73
Figure 5.7 Variation in corrosion current with magnetic field. These results are for API X80 linepipe steel in 1N H ₂ SO ₄	73
Figure 5.8 Results from the electrochemical impedance spectroscopy experiments; (a) Nyquist plots, (b) Phase angle and Impedance magnitude. (a) Comparison of the Nyquist plots at 0.0 and 0.3 Tesla, the single capacitive loop is indicative of a charge transfer process occurring on the surface of the electrode.	75
Figure 5.9 Results from the electrochemical impedance spectroscopy experiments; (a) Nyquist plots, (b) Phase angle and Impedance magnitude. (a) Comparison of the Nyquist plots at 0.0 and 0.5 Tesla, the single capacitive loop is indicative of a charge transfer process occurring on the surface of the electrode.	76
Figure 5.10 Results from the electrochemical impedance spectroscopy experiments; (a) Nyquist plots, (b) Phase angle and Impedance magnitude. (a) Comparison of the Nyquist plots at 0.0 and 0.7 Tesla, the single capacitive loop is indicative of a charge transfer process occurring on the surface of the electrode.	77
Figure 5.11 Comparison of the Nyquist plots at all of the different field strengths. The data given by the Nyquist plots is indicative of a single charge transfer process occurring on the surface of the electrode. From this data it can be seen that a magnetic field increases the charge transfer resistance.	78
Figure 5.12 Plot depicting the shift in open circuit potential (OCP) with an applied magnetic field. The shift in OCP with an applied magnetic field is a thermodynamic phenomenon.	79

Figure 5.13 Open circuit potential measurements for X80 linepipe steel grade with and without a magnetic field. The solid line is the OCP measurement with the magnetic field. The dashed line is the OCP measurement without the magnetic field. The quantity ΔV_M is the difference in open circuit potential after two hours of immersion in 1 N H_2SO_4 solution. The magnetic field strength is 0.7 Tesla.	80
Figure 5.14 Plot of the cathodic branch of the potentiodynamic polarization curve. The limiting current density is shown as decreasing with increasing magnetic field strength. The limiting current density is where the polarization curves intersect the x-axis (current density).....	82
Figure 5.15 Schematic showing how an applied magnetic field can decrease the thickness of the concentration gradient in front of the electrode. The top schematic shows the thickness of the concentration gradient with a magnetic field and the bottom schematic shows the thickness of the concentration gradient without a magnetic field.....	83
Figure 5.16 Potentiodynamic polarization curves for API X80 linepipe steel with and without a magnetic field. The plot has characteristic potentials and currents labeled, illustrating the difference in corrosion behavior with and without a magnetic field.....	85
Figure 5.17 Schematic showing the anodic dissolution of iron; (a) without an applied magnetic field, and (b) with an applied magnetic field.	87
Figure 5.18 Potentiodynamic polarization curve for API X80 at a magnetic field strength of 0.7 Tesla. F_L represents the Lorentz force and this schematic shows regions on the polarization curve where the Lorentz force is dominant. On the anodic branch, the Lorentz force is greatest at the passivation potential.	88
Figure 5.19 Variation in passivation potential as a function of magnetic field strength for API X80 linepipe steel in 1 N H_2SO_4	89
Figure 5.20 Block diagram for a hypothetical linear system. The ratio of the Laplace transform of the output to the Laplace transform of the input is the transfer function of the system.	90
Figure 5.21 Circuit used to model the impedance behavior of the electrode/electrolyte interface. The letters CPE represent a constant phase element.....	92
Figure 5.22 Results from the electrochemical impedance spectroscopy experiments; (a) Nyquist plots, (b) Phase angle and Impedance magnitude. (a) Comparison of the Nyquist plots at 0.0 and 0.7 Tesla, the single capacitive loop is indicative of a charge transfer process occurring on the surface of the electrode.	93
Figure 5.23 Variation in charge transfer resistance as a function of magnetic field strength for API X80 linepipe steel in 1 N H_2SO_4	96
Figure 5.24 Comparison of the phase angle plots at the four different magnetic field strengths for API X80 linepipe steel in 1 N H_2SO_4 . The arrows show the effect of changing the system parameters: R_{ct} , R_Ω , C_{dl}	96
Figure 5.25 Comparison of the impedance magnitude plots at the four different magnetic field strengths for API X80 linepipe steel in 1 N H_2SO_4	97

Figure 5.26 Nyquist plot comparing experimental data (triangles) and model data (black/white circles) using the equivalent circuit given in Figure 5.21. This data is for API X80 linepipe steel in 1 N H ₂ SO ₄	98
Figure 5.27 Impedance magnitude plot comparing experimental data (triangles) and model data (black/white circles) using the equivalent circuit given in Figure 5.21. This data is for API X80 linepipe steel in 1 N H ₂ SO ₄	98
Figure 5.28 Phase angle plot comparing experimental data (triangles) and model data (black/white circles) using the equivalent circuit given in Figure 5.21. This data is for API X80 linepipe steel in 1 N H ₂ SO ₄	99
Figure 5.29 Plot of the imaginary impedance as a function of frequency. The high frequency impedance data converge to approximately the same slope, the slope gives the value of α .	100
Figure 5.30 Linear regression analysis of the high frequency impedance data for API X80 linepipe steel at magnetic field strengths of: (a) 0.0 Tesla, and (b) 0.3 Tesla.	101
Figure 5.31 Linear regression analysis of the high frequency impedance data for API X80 linepipe steel at magnetic field strengths of: (a) 0.5 Tesla, and (b) 0.7 Tesla.	102
Figure 5.32 Variation in double layer capacitance as a function of magnetic field strength for API X80 linepipe steel in 1 N H ₂ SO ₄	103
Figure 5.33 Nyquist plot of API X80 linepipe steel at a magnetic field strength of 0.7 Tesla in 1 N H ₂ SO ₄ . The low frequency tail is shown in the box labeled 'Tail'. This behavior is due to a decreasing corrosion rate as the experiment progresses.	105
Figure 5.34 Nyquist plot of API X80 linepipe steel at a magnetic field strength of 0.7 Tesla in 1 N H ₂ SO ₄ . The low frequency asymmetry is shown in the box labeled 'Asymmetry'. This behavior is due to an increasing corrosion rate as the experiment progresses. This behavior is evident at lower magnetic field strengths as well; see Figure 8(a).	105
Figure 6.1 Plots of boundary layer thickness as a function of distance down the plate. The solid line represents the analytical solution while the open circles represent the exact solution. (a) $\beta = 1$ and $M = 0$, (b) $\beta = 1$ and $M = 1$, (c) $\beta = 1$ and $M = 2$, (d) $\beta = 1$ and $M = 3$. The analytical solution is in very good agreement with exact solution.	113
Figure 6.2 Plot of the boundary layer thickness as a function of distance down the plate. The solid line represents the analytical solution while the open circles represent the exact solution. (a) $\beta = 1$ and $M = 4$, (b) $\beta = 1$ and $M = 5$, (c) $\beta = 1$ and a comparison of all M values. Note the good agreement between the analytical and exact solution for all cases. The overall effect of a magnetic field is to decrease the boundary layer thickness.	114
Figure 6.3 Plot velocity profiles as a function of distance down the plate. The solid line represents the analytical solution and open circles represent the exact solution. (a) $\beta = 1$ and $M = 2$, (b) $\beta = 1$ and $M = 3$, (c) $\beta = 1$ and $M = 2$, (d) $\beta = 1$ and $M = 1$. The analytical solution is in very good agreement with exact solution.	115

Figure 6.4 Plots of the velocity profiles as a function of distance down the plate. The solid line represents the analytical solution and open circles represent the exact solution. (a) $\beta = 1$ and $M = 4$, (b) $\beta = 1$ and $M = 5$, (c) Comparison of all velocity profiles for all values of M . Note the good agreement between the analytical and exact solution for all cases. 116

Figure 6.5 Plots of boundary layer thickness as a function of distance down the plate. The solid line represents the analytical solution. No exact solution exists for $\beta \neq 1$. (a) $\beta = 5$ and $M = 0$, (b) $\beta = 5$ and $M = 1$, (c) $\beta = 5$ and $M = 2$, (d) $\beta = 10$ and $M = 10$. Note the decreased range of validity for the last case (d). 117

Figure 6.6 Schematic representation of natural convective boundary layer on a vertical electrode. The magnetic field is parallel to the electrode surface. 120

Figure 6.7 Velocity and concentration profiles for different values of the magnetic parameter N and Schmidt number, Sc ; (a) velocity profile: $N = 0$ and $Sc = 1$, (b) concentration profile: $N = 0$ and $Sc = 1$, (c) velocity profile: $N = 0.5$ and $Sc = 5$, (d) concentration profile: $N = 0.5$ and $Sc = 5$. 129

Figure 6.8 Velocity and concentration profiles for different values of the magnetic parameter, N and Schmidt number, Sc ; (a) velocity profile: $N = 0$ and $Sc = 10$, (b) concentration profile: $N = 1$ and $Sc = 10$, (c) velocity profile: $N = 5$ and $Sc = 10$, (d) concentration profile: $N = 5$ and $Sc = 10$. 130

Figure 6.9 This shows a schematic of a natural convective boundary layer on a vertical electrode. The magnetic field is parallel to the electrode surface. 132

Figure 6.10 This plot gives the boundary layer profiles for a nonlinearly varying magnetic field over a flat plate at $\beta = 1$ and $M = 0, 1, 2, 3, 4$, and 5 (increasing in the direction of the arrow). 136

Figure 6.11 This plot gives the velocity profiles for a nonlinearly varying magnetic field over a flat plate at $\beta = 1$ and $M = 5, 4, 3, 2$, and 1 (decreasing in the direction of the arrow). 137

Figure 7.1 Plot showing hydrogen concentration as a function of magnetic field strength. The magnetic field strength was varied from 0.0 to 0.7 Tesla. A magnetic field strength of 0.7 Tesla alters the hydrogen absorption behavior most significantly. This data is for API X80 linepipe steel in 1 N H_2SO_4 . 141

Figure 7.2 Comparison plot of all Hydrogen charging results for X80 high-strength linepipe steel in 1 N H_2SO_4 . This plot shows total hydrogen concentration as a function of time. All of the stress levels are represented on this plot. 142

Figure 7.3 These figures show; (a) Nyquist plots of API X80 linepipe steel at different magnetic field strengths, (b) variation in charge transfer resistance with magnetic field strength of API X80 linepipe steel. 143

Figure 7.4 This is a plot of corrosion current as a function of magnetic field strength for API X80 linepipe steel in 1 N H_2SO_4 . 144

Figure 7.5 This plot shows the variation in open circuit potential and corrosion current with applied magnetic field. 145

Figure 7.6 Potentiodynamic polarization curve for API X80 at a magnetic field strength of 0.7 Tesla. F_L represents the Lorentz force and this schematic shows regions on the polarization curve where the Lorentz force is dominant. On the anodic branch, the Lorentz force is greatest at the passivation potential. 146

LIST OF TABLES

Table 1.1 Cracking results for X70 and X80 linepipe steel..... 18

Table 1.2 Table of MHD parameters 15

Table 1.3 Dimensionless groups for MHD..... 16

Table 1.4 Magnetic field strength and limiting current densities, Fahidy (1973)..... 21

Table 2.1 Hydrogen charging results for X52, X70, and X80 steels with and without a magnetic field for twelve hours 27

Table 2.2 Comparison of corrosion parameters for X52, X70, and X80 steels. The letter M stands for magnet. 38

Table 3.1 Chemical compositions of X52, X70, and X80 linepipe steels; all compositions in weight percent..... 43

Table 5.1 Current densities and potentials from a polarization experiment performed on API X80 linepipe steel with and without a 0.7 Tesla magnetic field. M stands for magnet..... 84

Table 5.2 Equivalent circuit modeling results for API X80 linepipe steel in 1 N H_2SO_4 104

Table 6.1 Percent error for $\beta = 1$ and $M = 1$ velocity profile given in Figure 6.3(d) 118

Table 6.2 Percent error for $\beta = 1$ and $M = 2$ velocity profile given in Figure 6.3(a) 119

CHAPTER 1

INTRODUCTION AND LITERATURE REVIEW

1.1 Introduction

This Chapter will begin with a review of the previous work performed at the Colorado School of Mines (CSM) on the corrosion and hydrogen absorption behavior of API X80, X70, and X52 linepipe steels in the presence of a magnetic field. Lastly, a review and analysis of the literature pertaining to magneto-electrochemistry will be presented.

1.2 Review of Prior Work

The focus of the initial research work was to demonstrate experimentally that the magnetic induction generated by MFL inspection tools affects the hydrogen content in linepipe steels (as-received and cold-worked) and its influence on the hydrogen induced cracking susceptibility in pipeline steels. The initial work quantitatively measured the increase in hydrogen activity in high strength steels due to magnetization, Sanchez (2005).

Hydrogen may be introduced into a steel lattice from a variety of sources, such as welding, heat treatment, pickling, and in-service operations (oil and gas processing). The most common service source of hydrogen is the cathodic reduction of water, which is present during cathodic protection of steel pipelines, Sanchez (2005). The integrity of pipelines is monitored using intelligent inspection tools, also known as intelligent pigs (pipeline inspection gauge). To assess the integrity of a pipeline, a nondestructive technique known as Magnetic Flux leakage (MFL) is used. MFL magnetizes a steel pipeline to near the saturation flux density and then detects a local flux leakage caused by surface anomalies, such as cracks or dents. For a review of industrial pigging technology and operations see Hiltcher et al. (2003) and for a review of Magnetic Flux leakage see Atherton et al. (1987) and references therein.

1.2.1 Results of Initial Work

In the initial work by Sanchez, the effect of a strong magnetic field on hydrogen absorption and hydrogen induced cracking in high-strength linepipe steels was experimentally evaluated. Presented below is a summary of the theoretical and experimental work performed by Sanchez. In closing, a list of conclusions, as stated by Sanchez, will be given.

1.2.2 Thermodynamic Model

In the work done by Sanchez, a thermodynamic model was developed to assess the effect of magnetization on hydrogen absorption. The thermodynamic model accounted for the external work due to magnetization and related magnetic flux density, B , caused by MFL tools, to the total amount of absorbed hydrogen in the steel. The terms in the thermodynamic model are based on the hydrogen dissociation reaction and the work experienced by the steel under the magnetic flux density induced by MFL tools.

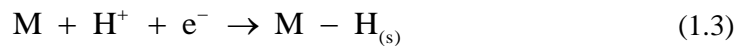
At constant pressure and temperature, the auxiliary function

$$dG = -\text{external work} \quad (1.1)$$

by modifying the Nernst equation with the addition of an internal work term ($-\Delta MB$) to the external electrochemical work term ($-n_e FE$), the differential Gibb's free energy is given buy:

$$dA = -\Delta MB - n_e FE \quad (1.2)$$

where ΔM represents the change in magnetization, B is the magnetic flux density, n_e is the number of electrons exchanged in the electrochemical reaction, F is Faraday's constant, and E is the electrochemical potential. Considering the electrochemical cathodic hydrogen reduction reaction, as given below



where $H_{(s)}$ is a hydrogen atom in solid solution in the metal matrix, M . The half-cell electrochemical potential, E , in Equation (1.2) is associated with the electrochemical reaction (1.3). The electrochemical potential energy is given by

$$E = E^0 - \frac{RT}{n_e F} \ln \left(\frac{[H]}{[M][H^+]} \right) \quad (1.4)$$

Substituting Equation (1.4) into Equation (1.2) gives Equation (1.5), which relates the free energy of the electrochemical reaction to magnetization and hydrogen content in the metal lattice.

$$dA = -\Delta MB - n_e F \left[E^0 - \frac{RT}{n_e F} \ln \left(\frac{[H]}{[M][H^+]} \right) \right] \quad (1.5)$$

For a given alloy composition, the activity of the metal, M, can be taken as unity. At equilibrium, $dA = 0$, and the hydrogen concentration as a function of the change in magnetization is given by

$$\ln[H] + 2.303 \text{ pH} - \frac{n_e F E^0}{RT} = \left(\frac{\Delta M}{RT} \right) B \quad (1.6)$$

rearranging Equation (1.6) gives the hydrogen content under a magnetic flux density as

$$[H]_{B=B} = [H]_{B=0} \exp \left(\frac{\Delta M}{RT} B \right) \quad (1.7)$$

where the equilibrium hydrogen content $[H]_{B=B}$ is determined under a magnetic flux density B, and the equilibrium hydrogen content when no magnetic field is applied is given by $[H]_{B=0}$ which is defined as

$$[H]_{B=0} = \exp \left(\frac{n_e F E^0}{RT} - 2.303 \text{ pH} \right) \quad (1.8)$$

Rearranging Equation (1.7) in terms of natural logarithms gives

$$\ln([H]_{B=B}) = \ln([H]_{B=0}) + \left(\frac{\Delta M}{RT} \right) B \quad (1.9)$$

A schematic plot of Equation (1.9) is given in Figure 1.1. The slope of the line is $(\Delta M/RT)$ and is a materials property.

1.2.3 Experimental Hydrogen Charging Results

The purpose of Sanchez's work was to assess the effect of a strong magnetic field on absorbed hydrogen content in API linepipe steels X80, X70, and X52. To that end, samples of linepipe steel grades X80, X70, and X52 were cathodically charged with and without a two Tesla magnetic field. The steel samples were cathodically charged at a potential of -0.550 volts for times ranging from one to twelve hours. The electrolyte used in the experimental work by Sanchez was 1N H₂SO₄.

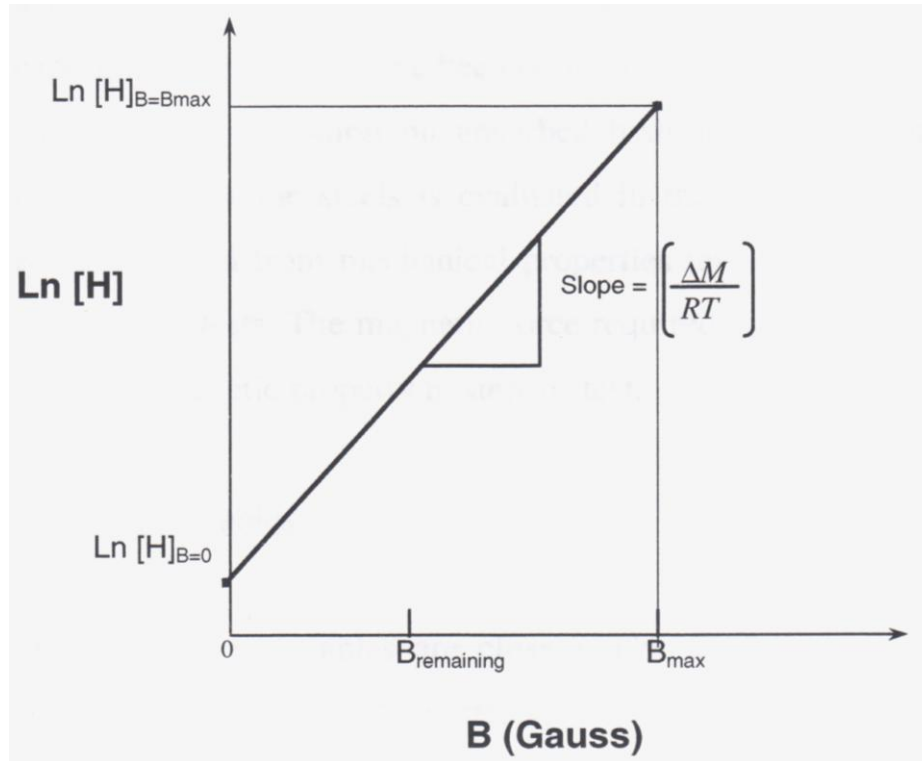


Figure 1.1: Schematic plot of Equation 2.8. The slope of the line is a material property; the y-intercept is the concentration of hydrogen in the steel without a magnetic field, Sanchez (2005).

To produce a constant two Tesla magnetic field, the same magnetic configuration was used for each experiment. The magnets were electrically isolated from the solution with the use of an epoxy resin; the purpose of the epoxy resin was to prevent current leaks during the experiments. The experimental results, shown in Figure 1.2, indicate that a magnetic field caused a marked effect on the absorbed hydrogen concentration in API X80, X70, and X52 linepipe steels.

At saturation, the absorbed hydrogen concentration in linepipe steel X52 under a two-Tesla magnetic induction was 6.1 times the concentration under cathodic charging conditions without an applied magnetic field. The results for the absorbed hydrogen concentration in the magnetized linepipe steels of grades X70 and X80 show that the saturation levels were 2.6 and 1.6 times the hydrogen content under non-magnetized conditions.

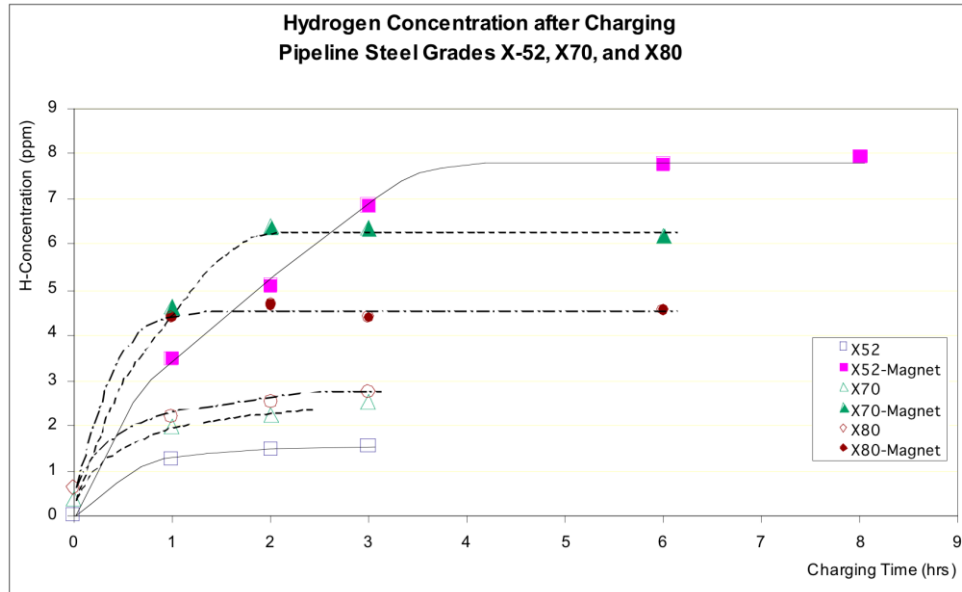


Figure 1.2: Comparison plot of steel grades X52, X70, and X80 with and without a magnetic field, Sanchez (2005).

1.2.4 Theoretical Explanation for Increased Hydrogen Absorption in a Magnetic Field

Sanchez gave two reasons for the increase in hydrogen content when a magnetic field is applied during the electrochemical charging experiments. One reason is due to the magnetic effect on the electronic spins, and the other is due to lattice distortion from interstitially dissolved hydrogen. The effects are explained in more detail below.

In the solid state, hydrogen occupies the interstitial sites between atoms in the metal lattice. The hydrogen atom dissociates into a proton and an electron in the steel, the proton occupies the interstitial site and the electrons are donated to the d-band of iron, Sanchez (2005). The positive charge of the proton has to be screened to preserve electrical neutrality. However, the screening process is not ideal, and repulsive forces occur between the proton and the positively charged metal nuclei. The existence of repulsive forces between the proton and the metal nuclei create local expansion and distortion of the metal lattice, Sanchez (2005).

The 3d band of iron is partially filled with five electrons with spin-up and only one electron with spin-down. As a consequence, there is spin polarization of the atom with a permanent moment. Therefore, an externally applied magnetic field during experimentation produced magnetic moments that were aligned parallel to the field direction, Sanchez (2005). The exchange energy or exchange force is repulsive for electrons with parallel spins. The repulsive

force due to parallel spins may distort the lattice in two possible ways: (a) producing a larger separation from one atom to another, or (b) producing a void because an electron jumps to a nearest neighbor creating an empty space and a double occupancy, Sanchez (2005).

The distortion of the steel lattice due to parallel aligned magnetic moments and repulsive electronic forces, as well as the preference of hydrogen to occupy interstitial sites, led to the following experimentally confirmed conclusion: “a strong magnetic field externally applied to the tested pipeline steels produces more available, suitable sites where hydrogen can preferentially diffuse and be trapped, increasing the absorbed hydrogen content”, Sanchez (2005).

1.2.5 Results for the Magnetization Effect on Hydrogen Concentration and Coldwork

To assess the effect of magnetization on hydrogen absorption in cold-worked steel samples, steel specimens were sectioned from cold-worked linepipe steel X70 and X80 and then cathodically charged for three hours in 1N H₂SO₄. Strain was introduced into the samples by bending the samples to different angles. Severely deformed materials develop a preferred orientation (known as fiber texture) which causes anisotropy in mechanical properties. During bending, the plastic strain is proportional to the distance from the neutral axis, which remains at the center fiber if the change in thickness is neglected. Fibers on the outer surface are stretched and fibers on the inner surface are compressed. The strain increases with decreasing radius of curvature, and for a given bending operation, the bending curvature cannot be larger than a critical value, or cracking of the material will occur, Sanchez (2005). The results were plotted in terms of hydrogen content as a function of bending angles (level of residual stress), Figures 1.3.

The experimental data presented in Figure 1.3 show that a strong magnetic field produces an enormous effect on the total hydrogen concentration in the tested pipeline steels under cold-work conditions. The cold-worked X70 linepipe steel samples can absorb up to 9.4 times more hydrogen than the as-received samples and the X80 linepipe steel can absorb up to 3.7 times the amount of hydrogen as the as-received samples in the same environment, Sanchez (2005).

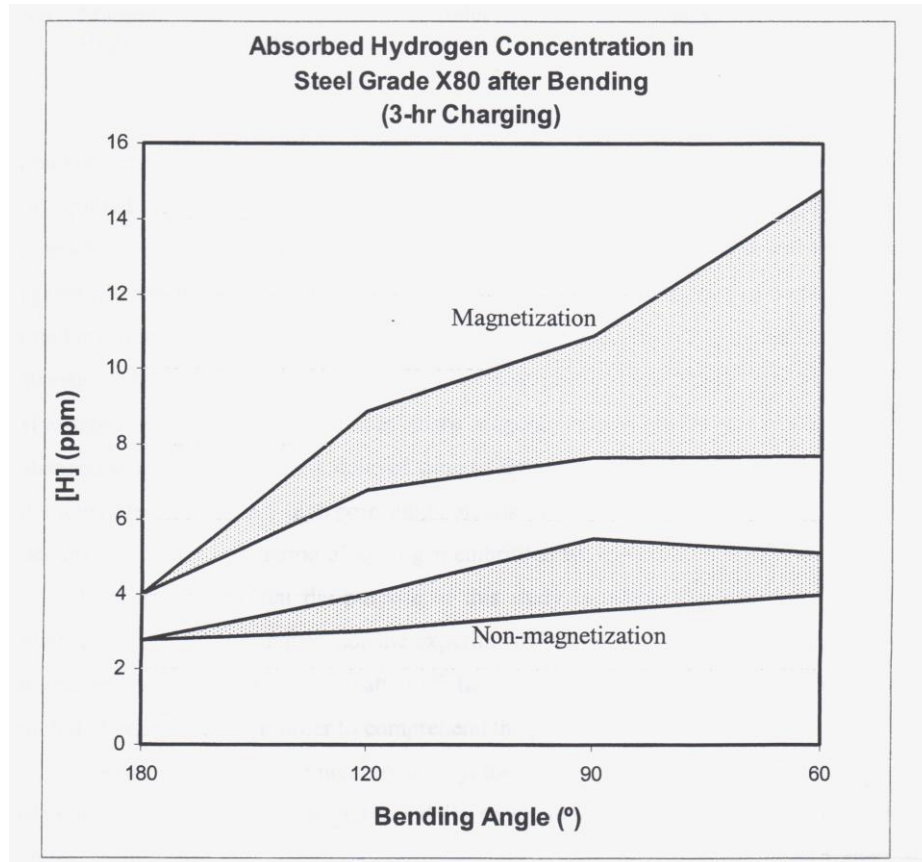


Figure 1.3: Plot of hydrogen concentration as a function of bending angle for X80 linepipe steel. The bottom region is a region of non-magnetization and the upper region in the plot is a region of magnetization, Sanchez (2005).

1.2.6 Results for the Magnetization Effect on Hydrogen Induced Cracking

Hydrogen damage or hydrogen embrittlement is a form of environmentally induced cracking that generally occurs as a result of the combined action of hydrogen and residual or applied stress. Hydrogen induced cracking, a type of hydrogen damage, is characterized by the brittle fracture of a typically ductile alloy under sustained loads in the existence of hydrogen, Sanchez (2005). A review of the types of hydrogen damage and hydrogen damage mechanisms is given in Beachem et al. (1977) and Interrante et al. (1982) and the references therein.

To simulate experimental conditions of standard hydrogen damage tests, a set of 60°-bending steel of grade X70 and X80 steel samples were used, Sanchez (2005). The tests were conducted using linepipe steel grades of X70 and X80 steel samples submerged in the charging

solution for 12, 24, and 36 hours with and without a magnetic field, Sanchez (2005). The results are summarized below in Table 1.1.

Table 1.1: Cracking results for X70 and X80 linepipe steel

Charging Time (hours)	Pipeline Steel Grade X70				Pipeline Steel Grade X80			
	Pitting		Cracks		Pitting		Cracks	
	Non-Magnet	Magnet.	Non-Magnet	Magnet	Non-Magnet.	Magnet	Non-Magnet	Magnet
12	Minor	Moderate	No	Yes	n/t	No	n/t	No
24	Minor	Heavy	No	Yes	No	Minor	No	Yes
36	n/t		n/t		Minor	Heavy	No	Yes

where n/t stands for not tested because it was considered non-relevant in terms of test purposes. This comparison evaluation points out the effect of magnetization on the nucleation and propagation of cracks in the tested pipeline steels under laboratory conditions, Sanchez (2005).

1.2.7 Conclusions Determined by Initial Hydrogen Absorbtion Research

The conclusions given below were paraphrased from the rearch work by Sanchez.

- A uniform magnetic induction produced by MFL pipeline pigging tools causes an increase in the total absorbed hydrogen concentration. The increase in hydrogen is thought to be due lattice distortion from parallel-aligned magnetic moments, repulsive electronic forces, and hydrogen segregation to lattice interstitial sites.
- At a remanent magnetic induction of 1 Tesla, the absorbed hydrogen concentration increases by nearly sixty percent. At magnetic saturation (pigging operation), the concentration could be as much as six times.
- A magnetic field of 2 Tesla produces a significant increase in the total hydrogen concentration in the cold-worked pipeline steels. X70 steel can absorb up to 9.4 times more hydrogen than as received steel and X80 steel can absorb up to 3.7 times the amount in the magnetized state.

- Magnetization accelerates the cracking mechanism because the saturation hydrogen content is reached quicker.
- Hydrogen damage or hydrogen induced cracking susceptibility of pipeline steels is negatively affected by magnetization at saturation levels. These results suggest that the remanent magnetization left by magnetic flux leakage inspection tools might also significantly affect the susceptibility to this cracking mechanism.

1.3 Review of Magnetic Field Effects on Magnetocorrosion

The initial work by Sanchez was performed to determine if there was a change in hydrogen absorption, and cracking behavior when a magnetic field was present during electrochemical hydrogen charging. Later, research was conducted to develop a better understanding of the thermodynamics and kinetics associated magnetism, hydrogen charging, and corrosion.

The review presented below focuses on a phenomena known as magnetocorrosion, Jackson (2008). Magnetocorrosion is the altered corrosion behavior in the presence of a magnetic field. The combination of magnetic and electric fields alters the magnetocorrosion behavior, including hydrogen content, pitting, and cracking of pipeline steels, Jackson (2008). The research performed on magnetocorrosion focused on the thermodynamics and kinetics of corrosion, and evaluated the correlation of magnetocorrosion to microstructure, mechanical properties, and magnetic properties, Jackson (2008).

1.3.1 Thermodynamics of Magnetocorrosion

The thermodynamic model developed by Jackson (2008) follows a similar derivation to that given by Sanchez (2005); however, the model developed by Jackson accounts for the work due to magnetostriction, and solute strain. The final form of the thermodynamic model is given as

$$[H] = [H]_{B=0} \exp\left(\frac{B\Delta M}{2RT}\right) \exp\left(\frac{Yd\delta M_s \mu_0 H}{3 \lambda_s RT}\right) \exp\left(-\frac{\frac{2}{3} \mu \frac{1}{\Omega} \left(\frac{d\Omega}{dc}\right) f(c)}{RT}\right) \exp\left(\frac{Y(\alpha dT)^2}{RT}\right) \quad (1.10)$$

where

$$[H]_{B=0} = \exp\left(-\frac{nF\phi}{RT}\right) \exp(2.3 \text{ pH}) \exp\left(-\frac{\Delta G^0}{RT}\right) \quad (1.11)$$

The first exponential term accounts for the hydrogen content that would be present in the steel without a magnetic field present during charging. The second exponential term is the work due to magnetostriction, the third exponential term accounts for solute-strain, and the last exponential accounts for temperature. Where Y is the bulk modulus, λ_s is the material saturation magnetization constant, M_s is the saturation magnetization, and μ_0 is the magnetic permeability in a vacuum. B and ΔM are the same as defined above in the model given by Sanchez. F is Faraday's constant and R and T have their usually meaning. μ is the shear modulus, Ω is the mean volume per atom of the alloy, and $f(c)$ is a linear function according to Vegard's law, Jackson (2008).

The thermodynamic models given by Sanchez (2005) and Jackson (2009) both predict an exponential increase in hydrogen from the effect of magnetization. In addition, given the thermodynamic basis of these models one could also expect a shift in the stability lines of the Pourbaix diagram. However, the change in ΔG due to magnetization is on the order of hundredths of volts, meaning that ΔG is approximately the same in the magnetized and unmagnetized state. Therefore, the Pourbaix diagram should remain unaltered when an external magnetic field is applied during experimentation. These calculations were based only on ΔMB and suggest that other work terms associated with magnetization need to be taken into account, Jackson (2008).

1.3.2 Kinetics of Magnetocorrosion

The kinetic model to describe the effect of magnetization on corrosion proposed by Jackson (2008) is based upon the Evans diagram, Helmholtz Double layer and Gouy-Chapman layer stirring, and the stirring of surface electrons in the metal. The Helmholtz double layer is analogous to a metal capacitor and can be thought of as a capacitor-like separation of positive and

negative charges. The Gouy-Chapman layer is a diffuse layer of charge directly adjacent to the Helmholtz double layer. In combination, these layers act to limit the diffusion of ionic species to the metal/electrolyte interface, Jackson (2008).

The application of cathodic protection currents in the presence of a remanent magnetic fields leads to the creation of Larmor loops. In a metal, surface electrons contribute to the conductivity according to

$$\sigma^n = \frac{N_{eff} \tau}{m_e} \quad (1.12)$$

where N_{eff} is the number of electrons in the skin layer, τ is the time of their interaction with the electromagnetic field, and m_e is the electron mass. Electromagnetic waves are sinusoidally periodic, and there exists two intervals of interest: when the electric field is dominant and when the magnetic field is dominant. Electromagnetic waves propagate approximately perpendicular to metal surfaces leading to higher surface fields. In the interval when the magnetic field is dominant, electrons move in “Larmor loops” due to the interaction of the electron charge and the magnetic field, creating a cross-product ($V \times B$) force that create looping orbits in the conduction band electrons in the metal, Jackson (2008). The behavior discussed above is shown schematically in Figure 1.4.

Magnetism will cause Lorentz forces to stir the moving ions in the electrolyte passing within a pipeline. Sufficiently high remanent magnetic fields may create a Lorentz force to stir the electrolyte and increase the limiting exchange current density, Jackson (2008). Cathodic protection increases the rate of hydrogen production while decreasing the corrosion current. Disturbance of the Helmholtz double layer will increase the exchange current and thus shift the polarization curve to greater currents, increasing the hydrogen content and decreasing the corrosion current, as shown in Figure 1.5, Jackson (2008).

The thermodynamic and kinetic models presented above suggest a theoretical explanation as to why a magnetic field increases the measured hydrogen content of high-strength linepipe steels when performing cathodic hydrogen charging experiments and serve as good starting points for further investigation.

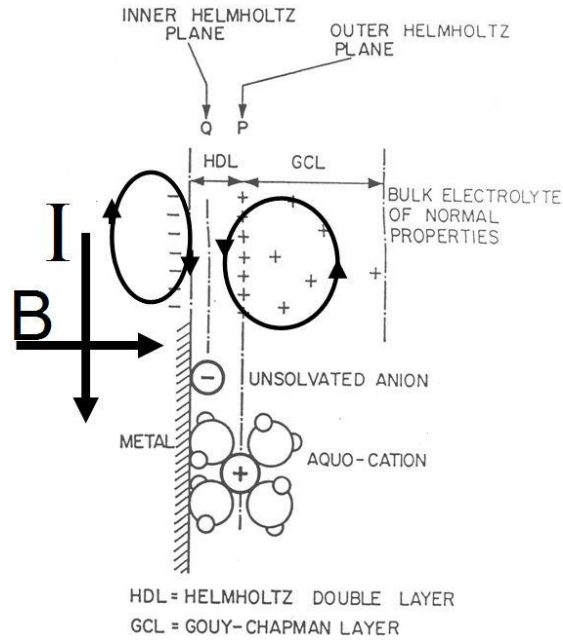


Figure 1.4: Schematic of Helmholtz double layer, Gouy-Chapman layer, and the Larmor loop effect from combined electrical and magnetic fields, Jackson (2008).

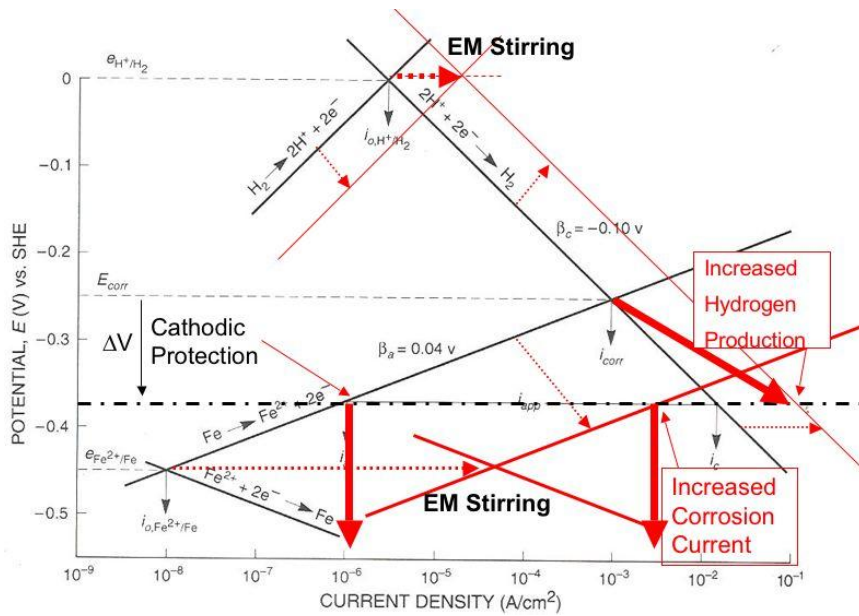


Figure 1.5: Schematic Evans diagram indicating increased hydrogen production and corrosion current due to cathodic protection and Helmholtz-Layer-controlled effects on hydrogen content, Jackson (2008).

1.4 Magnetochemistry

This Section of the literature review will focus on the salient aspects of magnetochemistry and elucidate the details associated magnetism and its effect on electrochemistry. The aspects of magnetochemistry to be presented are the following: (i) forces acting on the electrolyte when a magnetic field is present, (ii) the effect of magnetism on electrodeposition and mass transport. However, initially the topic of magnetohydrodynamics (MHD) must be discussed since MHD governs the transport of charged species and fluid flow of the electrically conducting media (electrolyte) in the electrochemical cell.

1.4.1 Magnetohydrodynamics (MHD)

MHD is concerned with the mutual interaction of fluid flow and magnetic fields. Therefore, the fluids must be electrically conducting and non-magnetic, limiting MHD flows to liquid metals, ionized gases, and strong electrolytes, Davidson (2001). MHD is a relatively young discipline in science and engineering beginning with the work of Hartmann (1937) in liquid metal duct flows and of Alfvén (1950) on cosmic gas dynamics, Müller et al. (2001). The mutual interaction of a magnetic field, \mathbf{B} , and a velocity field, \mathbf{u} , arises as a result of Faraday's law, Ampere's law and the Lorentz force experienced by a current-carrying body. These three processes can be split into three parts, Davidson (2001).

- i. The movement of a conducting fluid and a magnetic field causes an e.m.f. to develop according to Faraday's law of induction.
- ii. Induced currents give rise to a second, induced magnetic field. The induced magnetic field adds to the original magnetic field and the change is usually such that the fluid appears to 'drag' the magnetic field lines along with it.
- iii. The combined magnetic field interacts with the induced current density, \mathbf{J} , to give rise to the Lorentz force (per unit volume) $\mathbf{F}_L = \mathbf{J} \times \mathbf{B}$. The Lorentz force acts on the conductor and is directed to inhibit the movement of the magnetic field and the fluid.

Processes (ii) and (iii) have similar effects. In both cases the movement of the fluid and magnetic field tend to be reduced. Fluids can 'drag' magnetic field lines and magnetic fields can pull on

conducting fluids. These combined effects produce a ‘freezing together’ of the medium and the magnetic field, this feature is considered the defining characteristic of MHD flow.

1.4.1.1 Important Parameters of MHD

At this point it is important to introduce some of the parameters which characterize MHD flows. To begin, notation will be introduced, and then three important parameters in MHD will be presented, without derivation. Let μ be the permeability of free space, σ and ρ represent the electrical conductivity and density of the conducting medium, respectively, and l be a characteristic length scale. Three important parameters in MHD are given below in Table 1.2, Davidson (2001).

Table 1.2: Table of MHD parameters

R_m	$\mu \sigma u l$	Magnetic Reynolds Number
v_a	$\frac{B}{\sqrt{\rho \mu}}$	Alfven Velocity
τ	$[\sigma B^2 / \rho]^{-1}$	Magnetic Damping Time

The Magnetic Reynolds number is considered a dimensionless measure of conductivity, the second quantity has dimension of velocity and the third quantity has dimensions of time. The behavior of a magnetic field depends on the conductivity of the medium. When R_m is large, the magnetic field lines act like elastic bands frozen into the conducting medium. When R_m is small, \mathbf{u} has little influence on \mathbf{B} , with the induced field being negligibly small by comparison with the imposed field, Davidson (2001).

1.4.1.2 Governing Equations of MHD

The governing equations of MHD are developed by the incorporation of Lorentz force in the Navier-Stokes equations. The governing equations of MHD are presented below along with some of the key dimensionless groups associated with MHD flow. Beginning with Maxwell’s equations

$$\nabla \times \mathbf{B} = \mu \mathbf{J}, \quad \nabla \cdot \mathbf{J} = 0 \quad (1.13)$$

$$\nabla \times \mathbf{E} = -\frac{\partial \mathbf{B}}{\partial t}, \quad \nabla \cdot \mathbf{B} = 0 \quad (1.14)$$

and auxiliary expressions

$$\mathbf{J} = \sigma(\mathbf{E} + \mathbf{u} \times \mathbf{B}), \quad \mathbf{F} = \mathbf{J} \times \mathbf{B} \quad (1.15)$$

Combining these equations gives the magnetic induction equation

$$\frac{\partial \mathbf{B}}{\partial t} = \nabla \times (\mathbf{u} \times \mathbf{B}) + \lambda \nabla^2 \mathbf{B}, \quad \lambda = (\mu \sigma)^{-1} \quad (1.16)$$

where λ is the magnetic diffusivity and has units of m^2/s . Now, using Newton's second law, the equation for momentum transport is given as

$$\frac{D\mathbf{u}}{Dt} = -\nabla(p/\rho) + \nu \nabla^2 \mathbf{u} + (\mathbf{J} \times \mathbf{B})/\rho \quad (1.17)$$

where the term $D\mathbf{u}/Dt$ represents the material derivative. There are four dimensionless groups which frequently appear in MHD literature and are given below in Table 1.3.

Table 1.3: Dimensionless groups for MHD

Name	Symbol	Definition	Significance
Reynolds Number	Re	$u l / \nu$	Ratio of inertia to shear forces
Interaction Parameter	N	$\sigma B^2 l / \rho u$	Ratio of Lorentz forces to inertia
Hartmann Number	Ha	$Bl(\sigma / \rho \nu)^{1/2}$	Ratio of Lorentz forces to shear forces
Magnetic Reynolds Number	R_m	$u l / \lambda$	Ratio of advection to diffusion of B

1.4.2 Magnetochemical Forces

There are three forces acting on the electrolyte when a magnetic field is present in the electrochemical cell. The three forces are the Lorentz force, the concentration gradient force, and the magnetic field gradient force. The derivation and implications of these three forces will be presented and discussed below.

The density of magnetostatic energy of the electrolyte containing magnetic species is given by, Lioubashevski et al. (2007) and Landau et al. (1960):

$$E_m = - \frac{\mathbf{M} \mathbf{B}}{2 \mu_0} = - \frac{\chi_m \mathbf{C} \mathbf{B}^2}{2 \mu_0} \quad (1.18)$$

where $\mathbf{M} = \chi_m \mathbf{C} \mathbf{B}$ is the magnetization induced by \mathbf{B} , μ_0 magnetic permeability of free space, and χ_m is the molar magnetic susceptibility of the species involved. The force associated with the magnetostatic energy is obtained by taking the spatial derivative of Equation (1.18)

$$\mathbf{F}_{\text{mag}} = - \nabla E_{\text{mag}} = \frac{1}{2} \nabla (\chi_m \mathbf{C} \mathbf{B}^2) \quad (1.19)$$

giving

$$\mathbf{F}_{\text{mag}} = \frac{\chi_m \mathbf{B}^2 \nabla \mathbf{C}}{2 \mu_0} + \frac{\chi_m \mathbf{C} \mathbf{B} \nabla \mathbf{B}}{\mu_0} \quad (1.20)$$

where $\nabla \mathbf{B}$ is the magnetic field gradient and $\nabla \mathbf{C}$ is the concentration gradient. In one dimensional form the equation is given as

$$F_{\text{mag}} = \frac{\chi_m \mathbf{B}^2}{2 \mu_0} \frac{\partial \mathbf{C}}{\partial x} + \frac{\chi_m \mathbf{C} \mathbf{B}}{\mu_0} \frac{\partial \mathbf{B}}{\partial x} \quad (1.21)$$

the derivatives are kept as partial derivatives since the evolution of the concentration and magnetic fields could be functions of time. The force given in Equation (1.20) represents the summation of two separate forces, the concentration gradient force and the magnetic field gradient force. The concentration gradient force is given as

$$F_C = \frac{\chi_m \mathbf{B}^2 \nabla \mathbf{C}}{2 \mu_0} \quad (1.22)$$

and the magnetic field gradient force is

$$F_B = \frac{\chi_m \mathbf{C} \mathbf{B} \nabla \mathbf{B}}{\mu_0} \quad (1.23)$$

The concentration gradient force is directed towards areas with higher concentrations of paramagnetic species and the magnetic field gradient force is directed toward areas with higher values of magnetic field strength, Lioubashevski et al. (2007, 2004), Leventis et al. (2001, 1999, 2005), Devos et al. (2000), Bund et al. (2005), Ragsdale et al. (1998, 1996), and Grant et al. (2001). The third force which acts upon a unit volume fluid element is the Lorentz force

$$\mathbf{F}_L = \mathbf{I} \times \mathbf{B} \quad (1.24)$$

Overall, the three magnetic forces that act upon a fluid element are given by Equations (1.21)-(1.23). The Lorentz force acts when a fluid element carries current, the magnetic field gradient force acts when the volume element is located in a magnetic field gradient, and the concentration gradient forces acts when the concentration is nonuniform. Most importantly, the concentration gradient force is present even when the magnetic field is uniform, and acts upon the diffusion layer, Leventis et al. (2001). Therefore, as was mentioned above in the section on the governing equations of MHD, these forces can be incorporated into the Navier-Stokes equations to give the following transport equation

$$\rho \left(\frac{\partial \mathbf{u}}{\partial t} + \mathbf{u} \cdot \nabla \mathbf{u} \right) = -\nabla P + \nu \nabla^2 \mathbf{u} + \mathbf{I} \times \mathbf{B} + \mathbf{F}_B + \mathbf{F}_C \quad (1.25)$$

where ρ is the density and ν is the viscosity. More will be said about the magnetic forces in the chapter on MHD fluid flow modeling

1.4.3 The Effect of Magnetism on Mass Transport and Electrodeposition

In this section, the effect of a magnetic field on mass transport and electrodeposition will be discussed. In terms of mass transport, the review will focus mainly on the empirical relationships that have been developed and how these empirical relationships relate to the limiting current density. Secondly, the effect of a magnetic field on electrodeposition will be discussed. The primary affect of a magnetic field on electrodeposition is to alter the morphology of the deposited material.

1.4.3.1 The Effect of Magnetism on Mass Transport

As was mentioned above, magnetohydrodynamic phenomena arise from the interaction of velocity fields and electromagnetic fields. The effect of applying a magnetic field during electrolysis is strongest when mass transport is the controlling mode because of interactions with the convective diffusion layer at the electrode. The strength of the magnetic field effect is dependent upon the positions of the electrodes and the direction of the magnetic field, Tacken et al. (1995).

The orientation dependence of the magnetic field on mass transfer enhancement was studied by Mori et al. (2002). In their work, the electrolytic mass transfer rates under diffusion controlled conditions for cylindrical cathodes in various positions relative to the applied magnetic

field were analyzed. Specifically, three cathode-magnetic field orientations/geometries, Figure 1.6, were studied in an electrolytic solution of $K_3Fe(CN)_6 - K_4Fe(CN)_6$ in a magnetic field of up to 0.65 Tesla. For case one $\alpha < \pi/2$ and $\theta < \pi/2$, for case two $\alpha = \pi/2$ and θ at different angles relative to the north pole of the magnet, and for case three $\theta = 0$ and $\alpha = \pi/2$. For each case a regression equation was obtained that

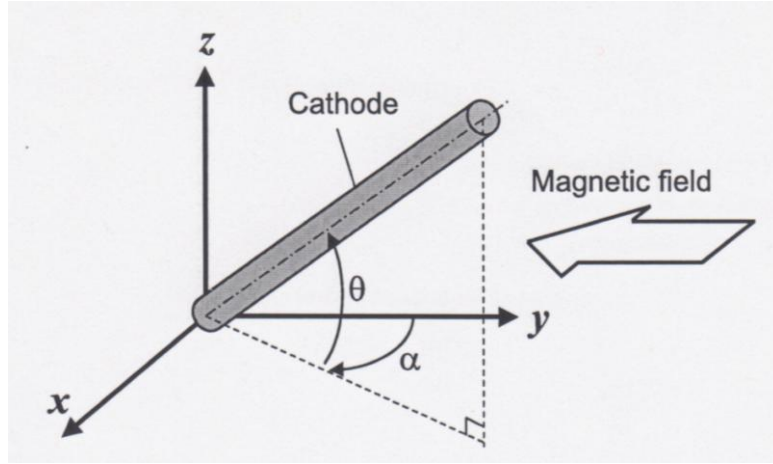


Figure 1.6: Cathode-magnetic field orientations studied by Mori et al. (2002). Their work showed that the mass transport effects caused by the magnetic field had strong orientation dependence.

related the magneto-diffusion factor to the Sherwood number. The magneto-diffusion factor was defined as

$$M_D = \frac{z F B \Delta C d_E^2}{\rho \nu} \quad (1.25)$$

Where z is the valence of the ion, F is Faraday's constant, B is the magnetic field, ΔC is the concentration gradient between the solution bulk and the interface, ρ is the density, ν is the viscosity, and d_E^2 is the characteristic length or equivalent diameter of the electrode. For the first case the equation is given by

$$Sh = 2.59 \left[M_D Ra^{1/2}/Sc \right]^{0.254} \quad (2.1)$$

for the second case the mass transfer enhancement equation is given by

$$Sh = 1.06 \left[(L/d)^{1.16} M_D Ra^{1/2}/Sc \right]^{0.286} \quad (2.2)$$

and for the third case the mass transfer enhancement equation is

$$\text{Sh} = 1.46 (L/d)^{0.253} \left[M_D \text{Ra}^{1/2} / \text{Sc} \right]^{0.271} \quad (2.3)$$

where $\text{Ra} = \text{Gr} \cdot \text{Sc}$ is the Rayleigh number and Gr is the Grashof number and Sc is the Schmidt number. $\text{Gr} = g \zeta \Delta C d_E^3 / \nu^3$ and $\text{Sc} = \nu / D$ where g is the acceleration due to gravity, ζ is the densification factor, D is the diffusion coefficient, and ν is the viscosity. Some of the results of their study are shown below in Figure 1.7.

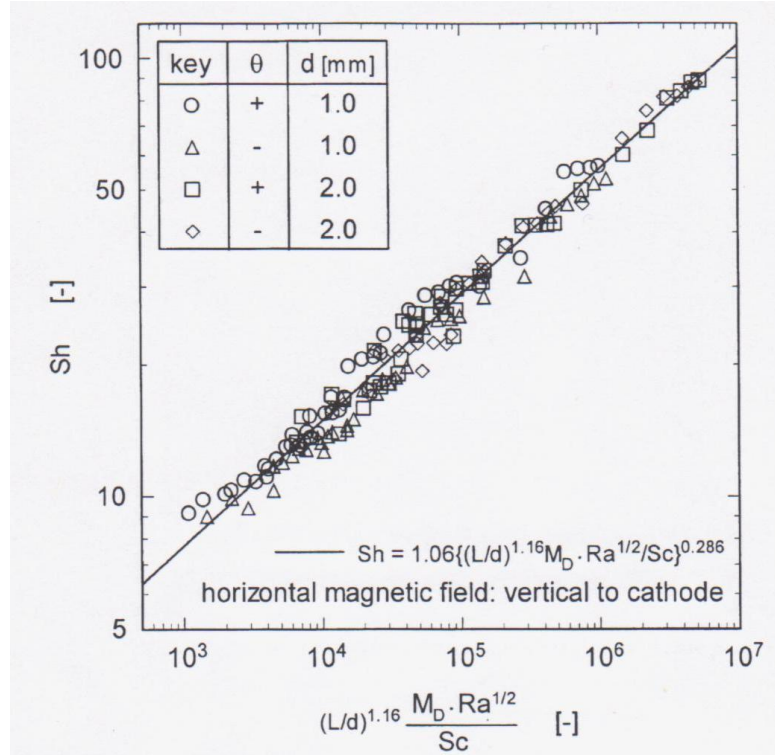


Figure 1.7: Plot of Sherwood number as a function of magnetic mass transfer enhancement factor.

The general effect of MHD in electrochemical applications is to produce convective movement of species at the electrode surface, and for electrochemical systems that are limited by mass transfer; the result of such convective movement is to increase the limiting current density.

In work by Fahidy (1972) he showed that during dc electrolysis, with the superposition of a magnetic field, that as the magnetic field strength was increased the limiting current density increased according to the following least-squares relationship

$$i_L = i_L^0 + a_1 B^{m_1} \quad (1.29)$$

where i_L is the limiting current density, i_L^0 is the limiting current density without a magnetic field, a_1 and m_1 are constants and B is the magnetic field strength. The data from his study, used to develop Equation (1.29), is shown below in Table 1.4. From the values given in Table 1.4, Fahidy determine the constants in Equation (1.29) to be $i_L^0 = 20.0$, $a_1 = 10.961$, and $m_1 = 1.6435$. Fahidy attributed the increase in limiting current density to a decreasing boundary layer thickness with increasing field strength.

In work by Legeai et al. (2004), the oxidation reactions of hexacyanoferrate(II) and hydroquinone at platinum disk electrodes in KCl media were studied using chronoamperometry under a 1.74 T

Table 1.4: Magnetic field strength and limiting current densities, Fahidy (1973)

Magnetic Field Strength B, T	Cathode Limiting Current density i_L , A/m ²
0.004	20.0
0.285	21.4
0.374	22.1
0.460	22.7
0.540	24.6
0.685	25.6

magnetic field. The limiting current density was fit to the following empirical equation

$$i_B = K C^a D^b d^c \nu^e \delta^f B^g n^h \quad (1.30)$$

where K is a proportionality constant, C is the concentration of electroactive species, D is the diffusion coefficient, d is the working electrode diameter, ν is the kinematic viscosity of the electrolyte, δ is the dielectric constant of the solution, B is the magnetic field strength, and n is the number of electrons involved in the redox process. From their work, it was found that the final form the empirical equation for limiting current density is

$$i_B = K C^{4/3} D d^{5/3} \nu^{-2/3} \delta^{-7/4} B^{1/3} n \quad (1.31)$$

The aim of the work by Legeai et al. was to determine the exponent of the dielectric constant and to validate the 1/3 power dependence on the magnetic field. As was mentioned before, the general effect of a magnetic field is to increase the limiting current density. For more information on

mass transport enhancement and empirical relationships on magnetic field strength and limiting current density see the following references: Bund et al. (2003), Boum et al. (1999), Chopart et al. (2002), Weier et al. (2005, 2007), Aaboubi et al. (2002), Mohanta et al. (1974, 1975, 1977), Wassef et al. (1975, 1975), Quraishi et al. (1981), Kim et al. (1997), and Fahidy et al. (1976, 1972, 1979, 1977, 1990, 1976, 1977, 1999).

1.4.3.2 The Effect of Magnetism on Electrodeposition

Magneto-electrolytic deposition (MED) can be defined as the formation of a substance layer on an appropriate substrate in an externally applied magnetic field, or in coupled electric and magnetic fields. The benefit of an externally applied magnetic fields on macroscopic properties, e.g., compactness and deposit uniformity, has been known for a century, and the effect on micro-scale behavior, e.g., growth orientation has been verified quantitatively in the last two decades, Fahidy (2001).

Krause et al. investigated the potentiostatic electrodeposition of cobalt, nickel, and copper in external homogeneous magnetic fields up to 1 Tesla. From their studies, it was concluded that the magnetic force

$$F_{\text{mag}} = \frac{\chi_m B^2}{2 \mu_0} \nabla C + \frac{\chi_m C B}{\mu_0} \nabla B \quad (1.32)$$

affects the deposition of copper, cobalt, and nickel independently of the direction of the superimposed magnetic field. They cite enhanced deposition rates of all metals and attribute the enhanced deposition rates to laminar fluid flow at the electrode surface brought about by the MHD effect. The MHD effect is known to decrease the diffusion layer thickness and increase the limiting current density.

In work by Ohno et al. (1975), in which the effect of magnetic field on the electrodeposition of an iron-nickel alloy was examined, they found that not only did the magnetic field enhance deposition rates but also altered the polarization. Ohno concluded that the effect of a magnetic field on the cathode potential was to increase polarization in the electrodeposition of nickel and iron-nickel alloys, which are magnetic materials. The polarization effect was greater when the magnetic field was perpendicular to the electrolytic current flux than when the two fluxes were in parallel, Ohno et al. (1975). In work done by Chouchane et al. (2007), it was found that during the electrodeposition of nickel and zinc, the magnetic field had an effect on

deposited alloy morphology and the presence of a magnetic field increased the solubility of nickel in zinc. Research by Koza et al. (2009) on the electrodeposition of Co-Fe alloys revealed that a magnetic field applied parallel to the electrode surface increased the limiting current density and increased deposition rates. For further review of the effect of magnetic fields on the electrodeposition process see the following papers: Motoyama et al. (2005), Koza et al. (2009), Barbier et al. (1998), and Ispas et al. (2007).

In closing, the effect of a magnetic field on electrodeposition processes is to increase the deposition rate and increase the limiting current density. The increase in limiting current density is true for any electrochemical process. These changes occur due the interaction of externally applied magnetic field and an electric current. The magnetic field and electric current interaction give rise to three forces: the Lorentz force, the concentration gradient force, and the magnetic field gradient force. The relative magnitude of these forces depends on the magnetic susceptibility of the species in the electrolyte, magnetic character of the electrode, and the orientation of the electrode relative to the magnetic poles.

CHAPTER 2

EXPERIMENTAL OBSERVATIONS AND STATEMENT OF PROBLEM TO BE SOLVED

2.1 Introduction

Throughout the course of this project many experimental observations have been made. As was pointed out in Chapter 1, the interaction of the magnetic field with the electric current generates magnetohydrodynamic forces which manifest in three forms; the Lorentz force, the concentration gradient force, and the magnetic field gradient force. These three forces act upon the species in the electrolyte which lead to complex fluid motion and electrochemical phenomena. The purpose of this chapter is to present the experimental observations, a consequence of the magnetic forces, and state the problem to be solved.

2.2 The Effect of a Magnetic Field on the Open Circuit Potential (OCP)

The experimental values obtained for OCP measurements with and without a magnetic, for API X80 linepipe steel, are shown below in Figure 2.1. The data presented in Figure 2.1 indicates that, upon application of a magnetic field, the OCP is shifted to more anodic potentials. A shift to more anodic potential values implies that the metal surface is experiencing corrosion of some type in the open circuit state. Steady state values are usually reached in the electrochemical cell after about five hours. The quantity ΔV_M represents the amount the potential is shifted when the magnetic field is present in the cell. Given the fact that Figure 2.1 shows OCP measurement taken for two hours, true values of ΔV_M could be several millivolts larger than what is reported below. The type of behavior shown in Figure 2.1 is not exclusive to X80 linepipe steel grade. The potential shift was observed for all steel grades, with the shift usually on the order of 10 – 15 mV. Therefore, the potential difference between the working electrode and the counter electrode can be defined in the following manner

$$E_m = E^0 + \Delta V_m \quad (2.1)$$

where E_m is the total potential difference between the working electrode and counter electrode, including the contribution from the magnetic field and E^0 is the standard potential of an electrode.

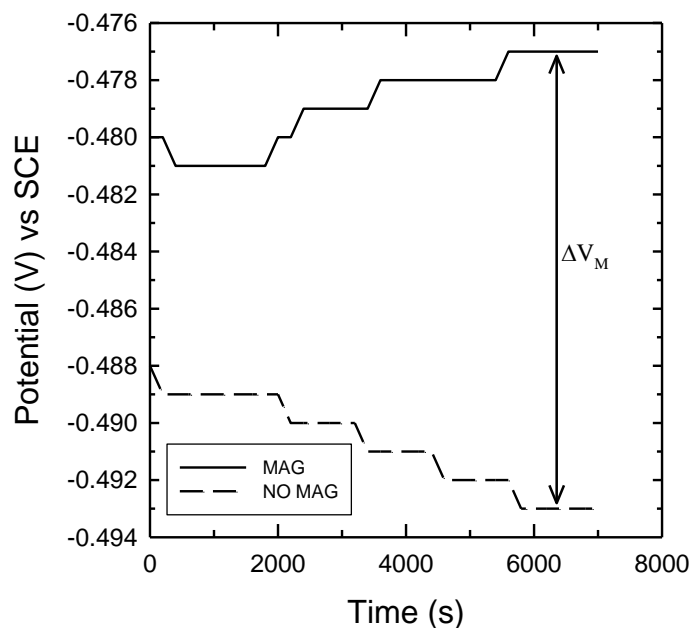


Figure 2.1: Open circuit potential measurements for X80 linepipe steel grade with and without a magnetic field. The quantity ΔV_M is the difference in open circuit potential after two hours of immersion in 1 N H_2SO_4 solution.

The shift in open circuit potential, due to an applied magnetic field, has been researched by many authors in the literature. In work by Rhen et al. (2007) the effect of a magnetic field and rotation speed of a rotating disk electrode on the corrosion current and open circuit potential of zinc and iron was studied using dichromate solutions acidified with nitric and sulfuric acid. They found open circuit potential shifts as large as 60 mV for zinc and 200 mV for iron. It was concluded that the open circuit potential is controlled by anodic current density and that the corrosion current density is controlled by cathodic reaction. Furthermore, Rhen and co-workers identified the Lorentz force as the main driving force responsible for the shift in open circuit potential. Research by Waskass et al. (1999) studied the effect of static magnetic fields on electrochemical processes taking place at ferromagnetic electrodes in paramagnetic solutions. In their work three systems were analyzed: ferric/ferrous, nickel/nickel-ion, and cobalt/cobalt-ion. Their results showed that a static magnetic field caused an anodic polarization for the ferric/ferrous system, and a cathodic polarization for the nickel/nickel-ion and the cobalt/cobalt-ion system. The shifts in open circuit potential were attributed to magnetoconvective effects, and gradients in the paramagnetic ion concentration next to the electrode surface. The gradient in

paramagnetic ion concentration was mentioned previously in Chapter 1 and was referred to as the concentration gradient force.

2.3 Erratic Hydrogen Charging Results with a Magnetic Field

In the initial experimental work by Sanchez (2005) it was shown that there was a significant increase in the amount of absorbed hydrogen when cathodic hydrogen charging was performed in the presence of a uniform magnetic field. Table 2.1, below, shows a sample of experimental data for the cathodically hydrogen charged linepipe steel grades X52, X70, and X80. The steel samples were electrochemically charged in 1 normal sulfuric acid (H_2SO_4) solution for twelve hours. All steel samples were prepared in the same manner. The steel samples were soaked in Trichloroethylene for twenty-four hours, rinsed with deionized water and then baked at two hundred degrees Celsius for four hours. The samples were baked to achieve a baseline level of hydrogen before electrochemically charging the steel specimen. After baking, each sample was polished to a 600-grit surface finish. Lastly, the sample would be soaked in Trichloroethylene to remove any residual oils. The steel samples charged with the magnetic field (0.7 Tesla) present in the electrochemical cell are indicated in the table.

When comparing the data presented in Table 2.1 to the data obtained by Sanchez, there exists a large discrepancy in the total hydrogen content. Referring to the data obtained by Sanchez, it can be observed that the hydrogen concentration, in all steel grades, reaches what appears to be saturation. However, considering Experiment No. 3, 9, and 15 in Table 2.1, it can be seen that the hydrogen concentration is more than three times greater than the saturation values for X70 and X80 steels reported by Sanchez.

Aside from the work by Sanchez, (2005), no work has been done on the effect of a magnetic field on cathodic hydrogen charging of API linepipe steels, or at least none can be found in the literature. However, a considerable amount of work has been done on the cathodic hydrogen charging of high-strength steels in general, see Interrante et al. (1982) as an example.

In more recent work by Dong et al. (2009) the hydrogen-induced cracking behavior of X100 pipeline steel was investigated using electrochemical hydrogen permeation measurements. Their experimental results showed that the amount of hydrogen-charging into X100 steel specimen increases with the charging time and charging current density. For example, they found that at steady state, the hydrogen concentration was approximately 9.5 ppm, 11.5 ppm, and 13 ppm after 1, 3 and 5 hours of charging respectively.

Table 2.1: Hydrogen charging results for X52, X70, and X80 steels with and without a magnetic field for twelve hours.

Experiment Number	Steel Grade	ppm[H]	Sample Mass (g)	Magnet	No Magnet	Time (hrs)
1	X52	3.97	0.775	X		12
2	X52	4.22	0.769		X	12
3	X70	22.6	0.875	X		12
4	X70	8.37	0.804		X	12
5	X80	3.12	0.807	X		12
6	X80	3.17	0.798		X	12
7	X52	3.97	0.775	X		12
8	X52	4.22	0.769		X	12
9	X70	22.3	0.857	X		12
10	X70	8.73	0.804		X	12
11	X80	9.01	0.776	X		12
12	X80	2.31	0.762		X	12
13	X70	3.76	0.819	X		12
14	X70	2.68	0.778		X	12
15	X80	23.9	0.796	X		12
16	X80	6.11	0.760		X	12
17	X80	6.99	0.770	X		12
18	X80	9.07	0.775		X	12

The electrolyte used for these experiments was 0.05 M H_2SO_4 + 250 mg/L As_2O_3 with a current density of 50 mA/cm². They also found that hydrogen charging will enhance the susceptibility of steel to HIC and cracks initiate primarily at inclusions in the steel. More work on the effects of hydrogen in high-strength steels can be found in Dong et al. (2009), Olden et al. (2008), Chaudhari et al. (1986) and the references therein.

2.4 The Effect of a Magnetic Field on Film Formation

It is believed that the formation of a corrosion product, during cathodic charging, is responsible for the variability in the hydrogen charging data. The experimental observation of an anodic shift in the open circuit potential lends support to this claim. In addition to the anodic potential shift, a black surface film was observed growing at the open circuit state before a charging experiment would begin (no current flowing). As was shown by Dey et al. (2006), there exists a thermodynamic desire for the steel specimen to develop a thin film of corrosion products, e.g. $\text{Fe}(\text{OH})_2$ and FeSO_4 , in freely corroding conditions (open circuit conditions). However, in the work by Dey, the experiments were done without a magnetic field present in the electrochemical cell.

Very little work has been done on cathodic film formation (passivation) of steel samples at the open circuit state with a magnetic field. The majority of work associated with passivation, film formation, and general corrosion behavior of iron electrodes in static magnetic fields has been performed by Lu et al. (2003, 2008, 2005). Lu's analysis of the corrosion behavior of iron electrodes in a static magnetic field was done by making potentiodynamic measurements (sweeping potential) and did not focus on the behavior of the electrode at the open circuit condition. More will be said about general corrosion behavior of the steel electrodes in Section 2.8 and the in the chapter on electrochemical corrosion behavior of steel electrodes in magnetic fields.

A conceptual model has been developed which gives an explanation as to why a magnetic field promotes film formation during cathodic experiments. The model is based on the thermodynamic associated with the Pourbaix diagram and kinetics based on the Evans diagram.

Cathodic hydrogen charging of steel in the presence of a magnetic field is difficult experimentally. The amount of hydrogen absorbed is dependent upon sample preparation technique, alignment of the sample in the magnetic field, alignment of the sample relative to the anode, and distance between the sample and the magnet surfaces. It is observed that the formation

of the corrosion products is accelerated by the application of an external magnetic field during cathodic hydrogen charging, Figure 2.2.

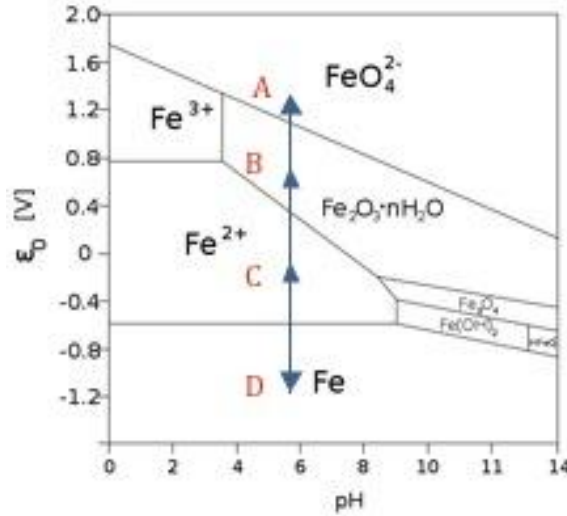


Figure 2.2: Schematic Pourbaix diagram for the iron-water system. The blue arrow indicates the direction in which the potential can shift when a magnetic field is applied to the system. A strong magnetic field could push the potential into region A (passive film formation), while a weak magnetic field could shift the potential into region C (active corrosion), and region D would be no magnetic field (immunity).

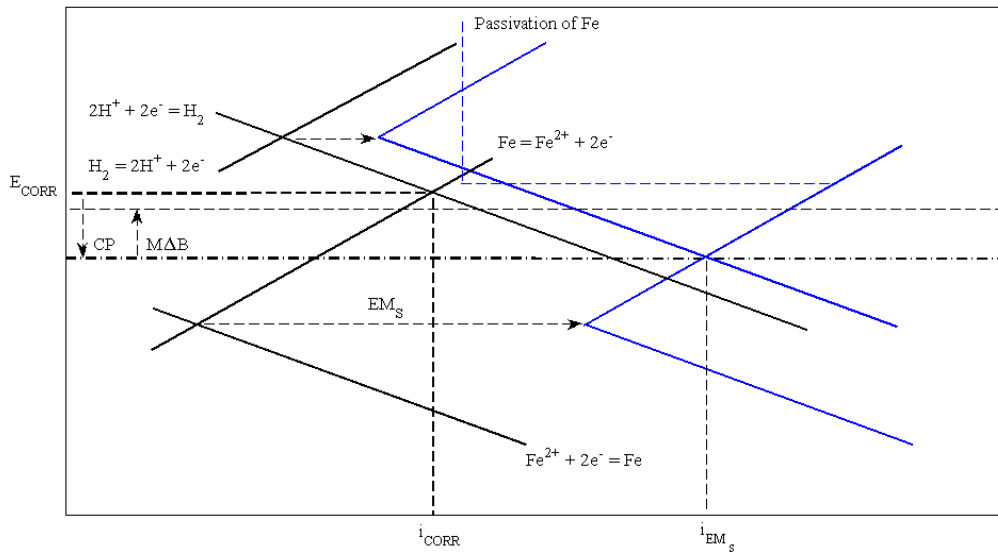


Figure 2.3: Schematic representation of an Evans diagram for the iron-water system. The black lines represent the original iron and hydrogen lines and the blue lines represent the iron and hydrogen lines shifted by the application of a magnetic field.

Referring to Figure 2.2, above, the blue arrows indicate the direction in which the potential is being shifted when a magnetic field is applied during the cathodic hydrogen charging experiments. The extent to which the potential is shifted depends upon the strength of the magnetic field ($M\Delta B$). Point A corresponds to a strong magnetic field, while point D corresponds to no magnetic field or a weak magnetic field. Intermediate ranges of magnetic field, point C and D, would cause a shift in potential into a region where iron would corrode. Figure 2.3 gives a kinetic model of what is occurring in the corrosion cell when a magnetic field is present during the hydrogen charging experiments. EM_s represents the shift in the half-cell reactions of iron and hydrogen when a magnetic field is applied. The magnetic field increases the corrosion current as shown by i_{EM_s} .

Two lines that are important to note in Figure 2.3 are CP (cathodic protection) line and the $M\Delta B$ (magnetic work) line. The CP line represents the potential shift when cathodic protection is applied to a steel pipeline. The result of cathodic protection is increased hydrogen production. The $M\Delta B$ line represents the positive potential shift from an applied magnetic field. As the magnetic field strength is increased, the amount that the potential is shifted in the positive direction also increases. Therefore, if $M\Delta B$ is small the potential may stay in the immunity region for iron, if $M\Delta B$ is increased further, the potential may be shifted into a region where iron corrodes, and if $M\Delta B$ is increased further still, the potential may be pushed into a region of passivity. The passive region is represented in Figure 2.3 by the blue dashed lines. Passivating behavior corresponds the formation of $\text{Fe}(\text{OH})_2$ and FeSO_4 .

Figures 2.4 and 2.5 show SEM images of X100 linepipe steel with corrosion product that formed during hydrogen charging experiments, Jackson (2008). It is believed that the formation of the corrosion products, $\text{Fe}(\text{OH})_2$ and FeSO_4 , gives rise to the variability in the hydrogen charging data. Figures 2.4 and 2.5 show the formation of a thin film of corrosion product on the surface of X100 line pipe steel. Figures 2.4 and 2.5 also show the cracking of the film. The cracks in the film are regions of increased current density and therefore increased hydrogen absorption. It is apparent that when cracks develop in the film, high levels of hydrogen absorption are observed and when cracks do not form in the film low levels of hydrogen are observed experimentally.

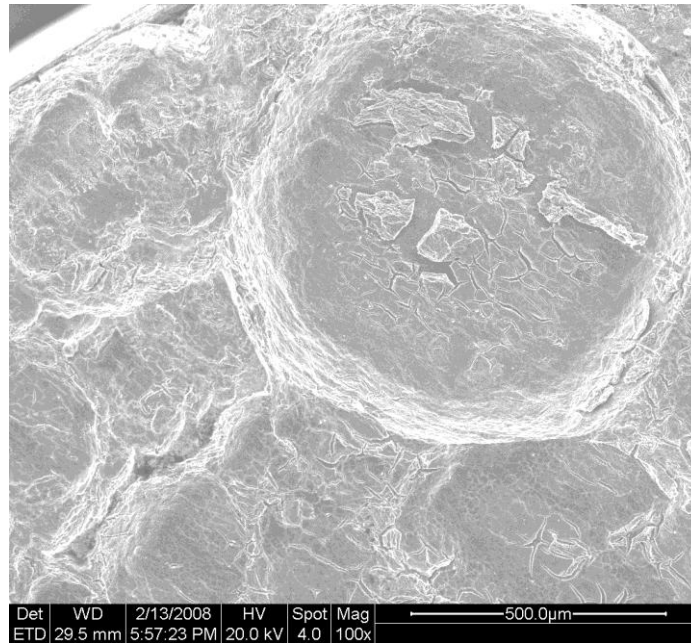


Figure 2.4: SEM image of X100 linepipe steel that was charged in a magnetic field. The image depicts cracking of the passivating film, Jackson (2008).

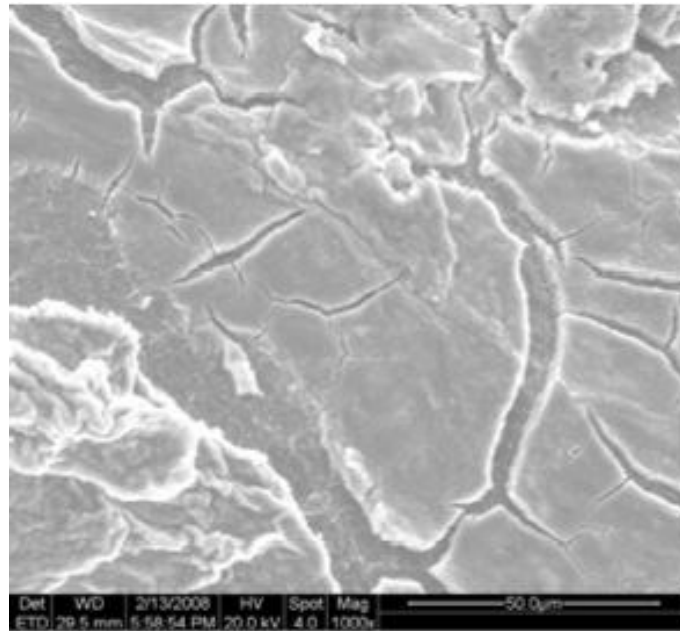


Figure 2.5: SEM image of X100 linepipe steel showing cracks in the passivating film. The crack in the film would give regions of increased current density and therefore increased hydrogen absorption, Jackson (2008).

2.5 Enhanced Pitting and Cracking Behavior with a Magnetic Field

It was experimentally demonstrated by Sanchez (2005) and Jackson (2009) that during electrochemical hydrogen charging experiments that the presence of a magnetic field promoted cracking and pitting behavior. This behavior is peculiar since, even though, the steel sample is polarized cathodically, the surface of the steel sample is exhibiting both cathodic and anodic behavior. Figure 2.6 shows this behavior on a sample of cathodically charged X70 linepipe steel. A similar behavior was reported by Kelly (1977) in experiments involving a titanium electrode in a 1 N H₂SO₄ solution. Kelly found that the imposition of a magnetic field during experimentation resulted in enhanced susceptibility to stress corrosion cracking, and localized corrosion. Kelly attributed these results to the Lorentz force acting on the species in the electrolyte.

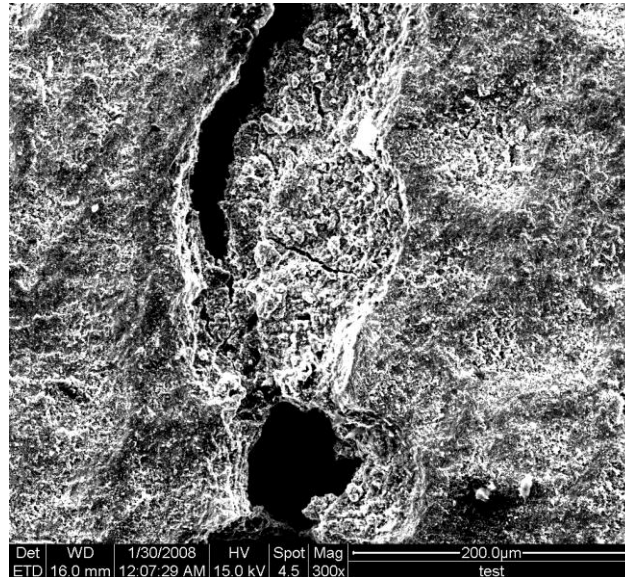


Figure 2.6: SEM image of X70 linepipe steel showing pitting and cracking behavior, Jackson (2008).

2.6 Electrolyte Stirring with a Magnetic Field

Observations made during experimentation revealed that bubbles typically nucleated at the bottom edge of the sample, would grow to a certain size, and migrate to the top of the sample. During the initial stages of an experiment the bubbles that nucleated were rather large and would cover a significant amount of sample surface area.

Bubble formation was dependent on the presence of a magnetic field. If there was no influence from the magnetic field the nucleation and growth of large bubbles on the sample

surface would proceed for approximately 1000 seconds. If the magnetic field was present, the nucleation and growth of large bubbles would proceed for approximately 500 seconds. After these times bubble formation would reach what could be considered steady state. Steady state is characterized by a significant decrease in bubble size and the formation of a thin, flowing bubble layer. In the unsteady condition, bubble size could reach diameters as large as 0.125 inches (3.175 mm).

Upon the establishment of steady state, two different flow paths were observed, which are dependent on the presence of a magnetic field. With no influence from a magnetic field, the bubbles would nucleate at the bottom of the sample and flow directly up the sample, Figure 2.7. However, once a magnetic field is introduced, the bubble flow path is altered and the flowing bubble layer is more diffuse. Under the influence of a magnetic field, the bubbles follow a helical flow pattern up and around the sample, Figure 2.8.

In the absence of a magnetic field, bubble formation occurs and bubbles flow directly up the sides of the cylindrical sample. In the presence of a magnetic field, bubble flow is noticeably decreased and flows helically outward towards to the magnets on either side of the specimen.

Aside from altering the bubble flow paths, the magnetic field will act to decrease the diffusion layer thickness as shown in Figure 2.9. By decreasing the diffusion layer thickness, the limiting current is increased. The increase in limiting current density, with application of a magnetic field, has been reported in the literature; for example, see Fahidy et al. (1976, 1972, 1979, 1977, 1990, 1976, 1977, 1999).

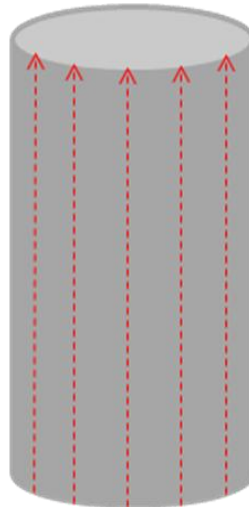


Figure 2.7: Bubble flow pattern without a magnetic field. The bubbles nucleated at the bottom of the steel sample and followed vertical flow path. There are no magnetic forces to alter the bubble trajectory.

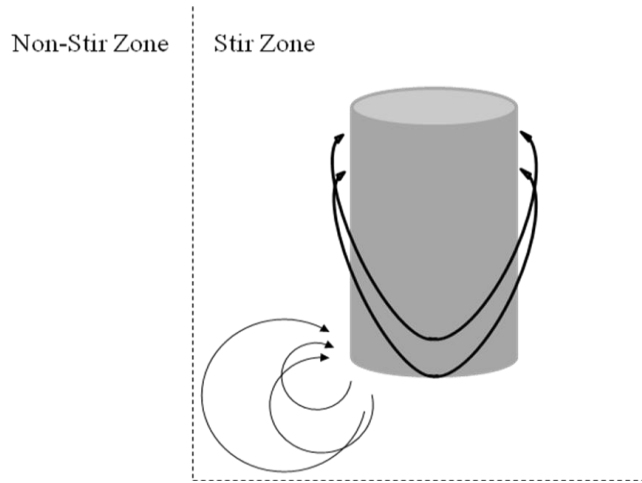


Figure 2.8: Schematic representation of the experimentally observed bubble flow with a magnetic field present in the electrochemical cell. When a magnetic field is present in the cell two distinct zones are present; a stir zone and non-stir zone.

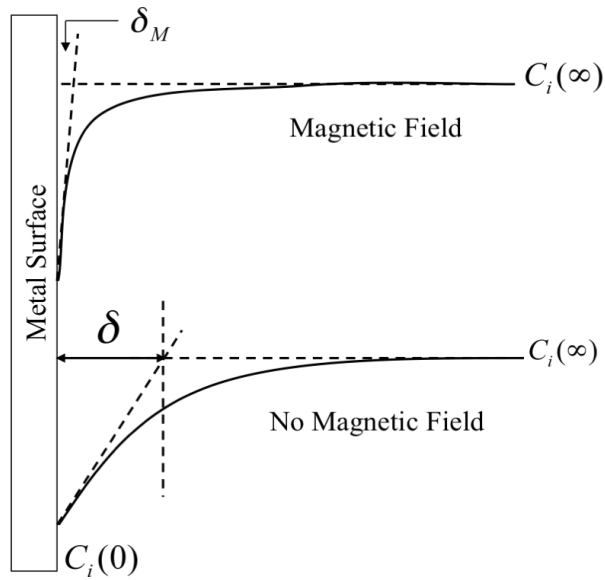


Figure 2.9: Schematic of a metal surface with different diffusion layer thicknesses. δ represents the diffusion layer thickness. The bottom curve in the schematic represents the diffusion layer thickness without a magnetic field. The top curve represents the diffusion layer thickness when the magnetic field is applied.

The magnetic forces responsible for the decrease in diffusion layer thickness are: the Lorentz force, the concentration gradient force, and the magnetic field gradient force. The Lorentz force is given as

$$\mathbf{F}_L = \mathbf{i} \times \mathbf{B} \quad (2.1)$$

the concentration gradient force is

$$F_C = \frac{\chi_m B^2}{2 \mu_0} \frac{dC}{dx} \quad (2.2)$$

and the magnetic field gradient force is

$$F_B = \frac{\chi_m C B}{\mu_0} \frac{dB}{dx} \quad (2.3)$$

where C is the concentration, B is the magnetic field strength, χ_m is the molar magnetic susceptibility, and μ_0 is the magnetic permeability of free space. Changes in the limiting current density can cause changes in the electrochemical kinetics of the system. The limiting current density is the measure of the maximum reaction rate that cannot be exceeded due to a limited diffusion rate of an ionic species in solution.

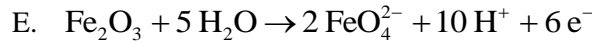
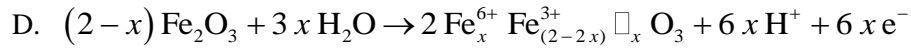
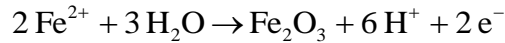
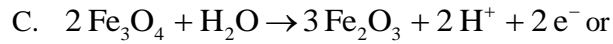
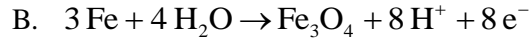
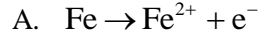
2.7 The Effect of a Magnetic Field on Passivation Behavior

The driving force for a corrosion reaction to occur is the potential difference between the anode and the cathode, and the rate of an electrochemical reaction is equal to the current that flows through the electrochemical cell. For a given potential difference between an anode and a cathode, the current (corrosion rate) will increase as the resistance throughout the cell decreases. The different types of polarization describe the various resistive elements in a corrosion cell Davis et al. (2000). Three types of polarization will be discussed below: activation polarization, concentration polarization, and ohmic polarization.

Activation polarization is when a step in the half-cell reaction controls the rate of electron flow, another way of stating this situation is that the reaction is under charge-transfer control, resulting in activation polarization. Concentration polarization results from mass transfer or diffusion-limited effects at metal surface, Davis et al. (2000). An example of this effect would be high cathodic reduction rates, where the solution directly adjacent to the metal surface becomes depleted of dissolved species being reduced. The last form of polarization, which will be discussed here, is ohmic polarization. Ohmic polarization is a result of pure resistance elements

along the current path in the electrochemical cell. Ohmic resistance is also referred to as iR effects, Davis et al. (2000).

Research on the polarization of iron has been interpreted to show that a series of electrochemical reactions occur as the polarization potential is increased, Stansbury et al. (2000). The reactions given below, denoted by the letters (A – E), are assumed to be the dominant reactions at the potential marked on the polarization curve in Figure 2.10.



where x , in chemical formula D, is the fraction of iron lattice sites occupied by Fe^{6+} in the Fe_2O_3 crystal structure, and \square represents the vacant iron lattice sites.

Passivation begins with reaction C. Reaction D begins as the potential is increased progressively above E_{pp} . Reaction D involves the formation of a defect oxide (an oxide containing vacant lattice sites). The point marked E_{pp} is known as the passivating potential, while point on the curve marked i_{crit} is the critical current density for passivation. i_p is the magnitude of the current density in the passive condition. The magnitude of the change from i_{crit} to i_p is important since this change in current density is indicative of the effectiveness of the passive film to reduce anodic dissolution (corrosion). The values of i_{crit} , E_{pp} , and i_p are important parameters which define the shape of the polarization curve and ultimately the corrosion behavior of the alloy. For example, low values of i_{crit} indicate that the alloy has the ability to passivate in many environments, Stansbury et al. (2000).

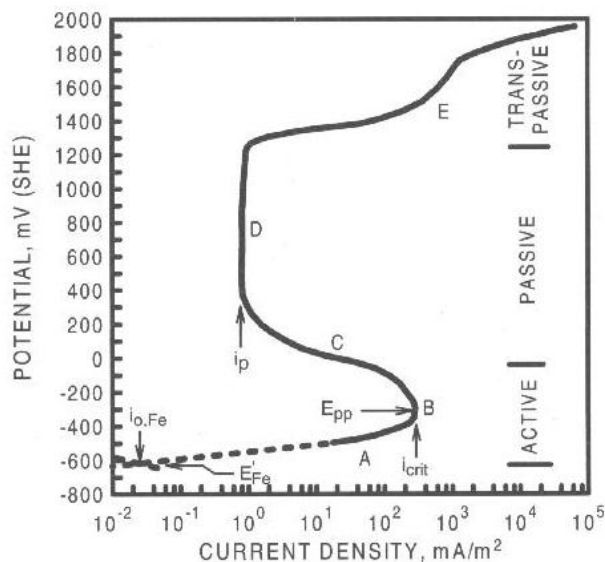


Figure 2.10: Schematic representation of a potentiodynamic polarization curve (anodic branch) for iron in a buffered solution of pH = 7. The letters (A – E) correspond to the electrochemical reactions given above, Stansbury et al. (2000).

2.7.1 Polarization Results for X52, X70, and X80

The polarization curves for X52, X70, and X80 linepipe steels were measured at a scan rate of 0.1667 V/s in 1N H₂SO₄ with and without a 0.7 T magnetic field in the electrochemical cell. The results of these experiments are given below in Figures 2.11 – 2.13. The important points to note from the figures presented below are the dramatic changes in the critical parameters that characterize the corrosion and passivation behavior of an alloy. Figures 2.11, 2.12, and 2.13 illustrate the large shifts in all parameters which characterize the corrosion behavior of X52, X70, and X80 linepipe steels in 1N H₂SO₄, namely i_p , i_{crit} , and E_{pp} with changes in magnetic field. These values are tabulated below in Table 2.2.

Table 2.2: Comparison of corrosion parameters for API X52, X70, and X80 linepipe steels. The letter M stands for magnet.

	i_p (A/cm ²)	$i_{p,M}$ (A/cm ²)	E_{pp} (V)	$E_{pp,M}$ (V)	i_{crit} (A/cm ²)	$i_{crit,M}$ (A/cm ²)
X52	0.00012	0.00036	0.56	0.98	0.0916	0.251
X70	2.42×10^{-5}	0.00059	0.285	0.881	0.039	0.33
X80	0.0891	0.0013	0.428	1.035	0.0891	0.251

From the results presented in Figures 2.11, 2.12, and 2.13, it may be stated that a magnetic field does not alter the general shape of the polarization curve, but has a significant effect on the specific currents and potentials which comprise the polarization curve. In all cases, a magnetic field increases the peak current, or i_{crit} , which is the current that must be exceeded to initiate the formation of a passive film. Therefore, by inspection of the figures below, a magnetic field makes it more difficult for any of the alloys to passivate (protect itself from corrosion). The magnetic field also increases E_{pp} , the passivating potential, and in all cases, decreases i_p . Lastly, the presence of a magnetic field in the electrochemical cell decreases the range of potential in which the metal is actually protected from corrosion. This behavior can be seen most readily in Figure 2.13, which is a comparison of polarization curves for X70 linepipe steel with and without a magnet. The passive region of X70 linepipe steel is essentially nonexistent with a magnetic field.

More will be said about the corrosion behavior of these steels in the chapter on electrochemical corrosion of API linepipe steel grades. However, the same type of behavior has been reported in the literature by Lu et al. (2005, 2008, 2003). In their work, they analyzed the effects of an applied magnetic field on the electrode processes of iron in sulphuric acid solutions with dichromate. Experimental measurements of the open circuit potentials, cathodic and anodic polarization curves, and polarization resistance were made in the presence and absence of a 0.4 Tesla magnetic field. Their results are consistent with those reported in this Chapter. They found a positive shift in the open circuit potential (E_{corr}) and a shift in the passivation potential in the anodic branch of the potentiodynamic polarization curve.

There are two distinct regions on a polarization curve: the cathodic branch and the anodic branch. The cathodic branch is the portion of the curve represented by negative potentials and the anodic branch of the curve is represented by positive potentials. Where the two curves meet gives the value of the corrosion potential. It is interesting to note that, even though the open circuit potential, also known as the corrosion potential (E_{corr}), is altered by the presence of a magnetic field, as shown in Figure 2.1, there is no noticeable change in the corrosion potential given by the potentiodynamic dynamic measurements in Figures 2.11, 2.12, and 2.13. One would expect, given the data from Figure 2.1 and the data given in the literature, that there would be a noticeable shift in the intersection point of the anodic and cathodic branches of the potentiodynamic curves when a magnetic field is applied. However, the potential shift is only noticeable at the passivation potential. This phenomenon will be investigated in a later chapter.

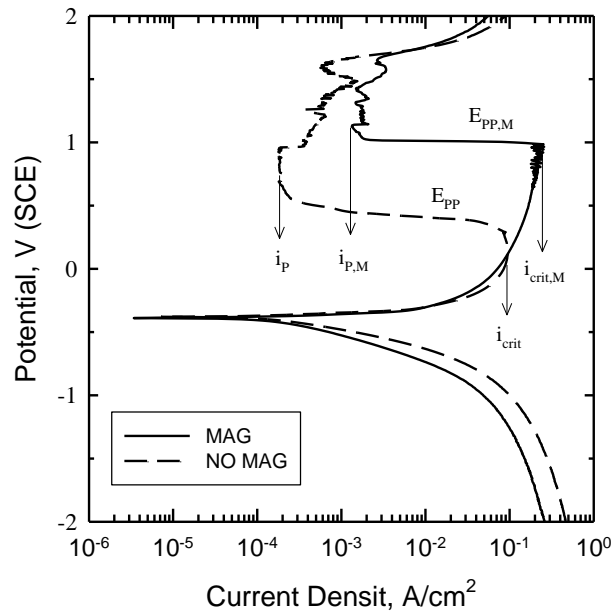


Figure 2.11: Potentiodynamic polarization curve for X80 linepipe steel with and without a magnetic field in 1 N H₂SO₄.

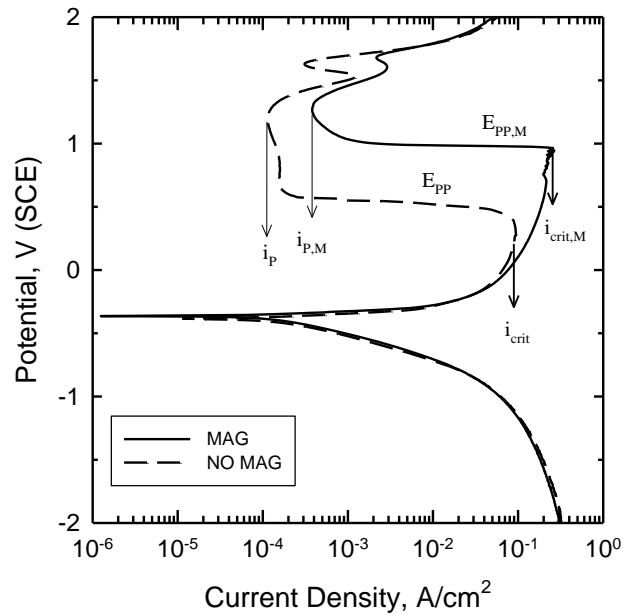


Figure 2.12: Potentiodynamic polarization curve for X52 linepipe steel with and without a magnetic field in 1 N H₂SO₄.

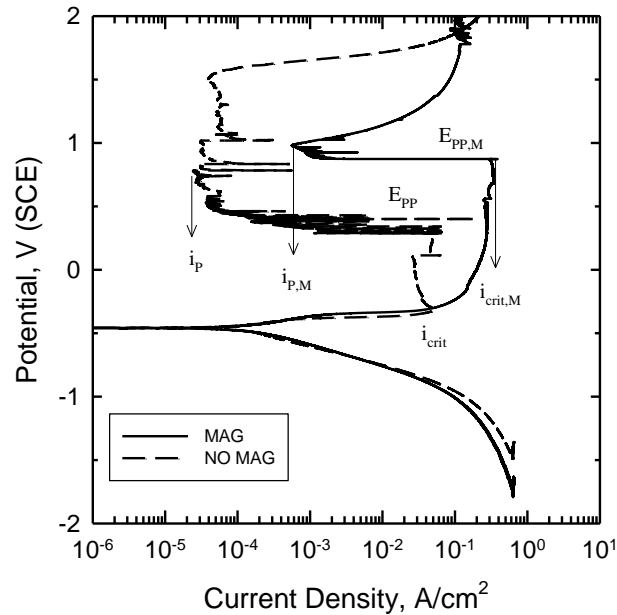


Figure 2.13: Potentiodynamic polarization curve for X70 linepipe steel with and without a magnetic field in 1 N H₂SO₄.

2.8 Research Problem to Be Solved

The purpose of this chapter was to present some of the experimental observations that have been made during the course of this research project and also provide a review of the literature which corroborates some of these experimental findings. It has been shown that a magnetic field can have many adverse effects on the hydrogen absorption behavior, pitting and cracking behavior, and overall corrosion behavior of a API linepipe steel. Many experimental techniques have been used to analyze this problem such as potentiostatic hydrogen charging, electrochemical impedance spectroscopy, and potentiodynamic polarization methods. The questions that need to be answered are the following:

1. Why does there exist a discrepancy in the hydrogen charging data obtained by Sanchez and that obtained by the author when the experimental conditions were identical?
2. What effect would changing the magnetic field strength have on the hydrogen absorption behavior of high-strength linepipe steel?
3. What is the effect of temperature on hydrogen absorption?

4. What is the effect of stress on hydrogen absorption?
5. Does a magnetic field alter the electron transfers kinetics associated with the electrochemical processes occurring on the sample surface?
6. Why is there no observable potential shift in the potentiodynamic polarization curves at the corrosion potential (OCP) but the OCP is known to shift when a magnetic field is present in the electrochemical cell?
7. Why does the passivation potential of the steel sample change when a magnetic field is present in the electrochemical cell?
8. What is the nature of the passivating film that forms during cathodic hydrogen charging experiments?
9. What is the fluid flow and mass transport behavior of the electrolyte next to the sample surface and what does this mean in terms of hydrogen absorption?

The driving force for this work is to understand the corrosion, and hydrogen absorption behavior of API linepipe steel grades that have been subjected to a pigging operation. The main objective of this research is to investigate and answer these questions and relate these findings to the conditions present in a high strength steel pipeline in the field.

CHAPTER 3
EXPERIMENTAL METHODS AND MATERIALS

3.1 Introduction

In this chapter the experimental materials that were used for this investigation will be presented and the various experimental techniques employed for this research work will be introduced. Experimental techniques include potentiostatic methods (cathodic hydrogen charging), electrochemical impedance spectroscopy (EIS), and potentiodynamic polarization methods. Lastly, an analytical mathematical modeling technique known as Adomian Decomposition Method (ADM) will be presented and discussed.

3.2 Experimental Materials

Three API linepipe steel grades were used for this research: X52, X70, and X80. The chemical compositions for these three steels are given below in Table 3.1.

Table 3.1: Chemical compositions of X52, X70 and X80 linepipe steels, all compositions in weight percent.

Steel	C	Mn	P	S	Ti
X52	0.0606	1.31	0.005	0.0073	-
X70	0.0718	1.42	0.012	0.0031	-
X80	0.07342	1.36	0.004	0.003	0.008

Figures 3.1-3.3 show the microstructures of these three linepipe steels, X52, X70, and X80 respectively. The microstructures are primarily ferrite, with the X52 microstructure having islands of pearlite at the ferrite grain boundaries.

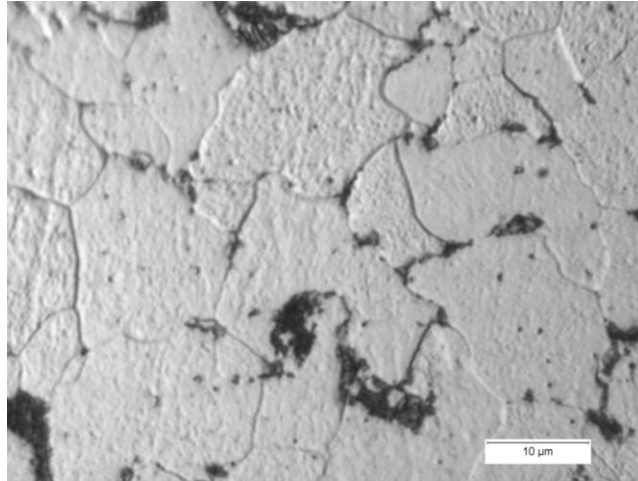


Figure 3.1: API X52 linepipe steel micrograph showing ferritic microstructure with small islands of pearlite at the grain boundaries.

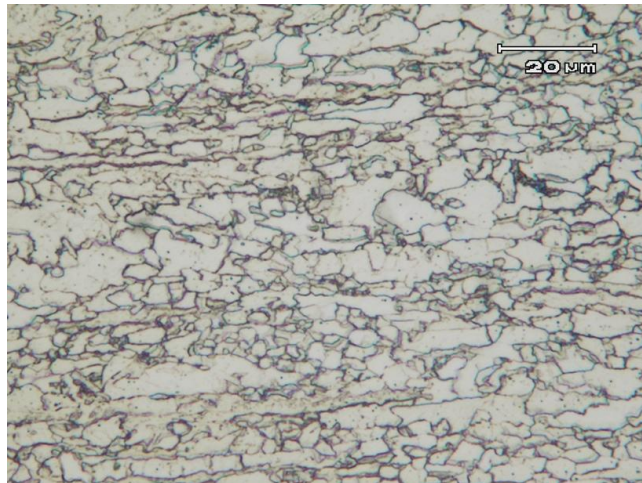


Figure 3.2: API X70 linepipe steel micrograph showing a fine-grained microstructure.

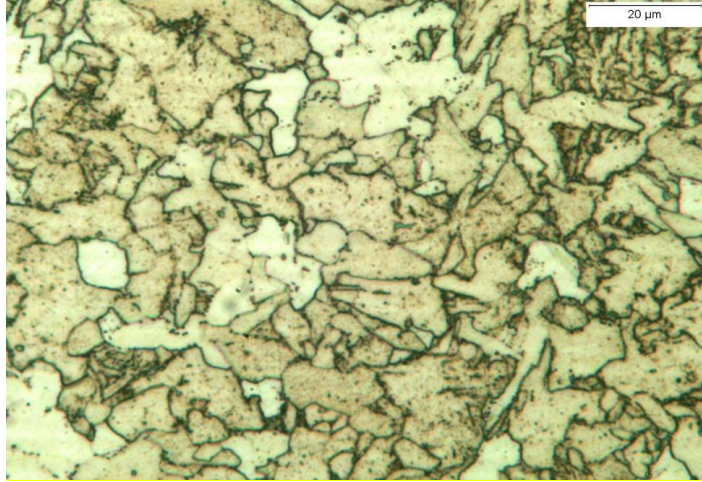


Figure 3.3: API X80 linepipe steel micrograph showing an irregular fine-grained ferritic microstructure.

3.3 Hydrogen Charging Environment

Cathodic charging of the steel samples was performed in a 1 N H_2SO_4 sulfuric acid solution. Acids, such as sulfuric acid, that contain more than one dissociable proton are called polyprotic acids. Polyprotic acids dissociate in a stepwise manner, and each dissociation step is characterized by its own acid-dissociation constant, K_{a1} , K_{a2} , and so on. Taking sulfuric acid as an example, the following dissociation reactions can be formed:



leading to the first acid dissociation constant:

$$K_{a1} = \frac{[\text{HSO}_4^-][\text{H}_3\text{O}^+]}{[\text{H}_2\text{SO}_4]} \quad (3.2)$$

K_{a1} is a very large number and therefore makes sulfuric acid a strong acid. Equation (3.1) describes the dissociation of sulfuric acid to bisulfate HSO_4^- . The second dissociation reaction is the bisulfate ion, HSO_4^- , going to sulfate SO_4^{2-} :



Equation (3.3) provides the second and last acid-dissociation constant for sulfuric acid:

$$K_{a2} = \frac{[\text{SO}_4^{2-}][\text{H}_3\text{O}^+]}{[\text{HSO}_4^-]} = 1.2 \times 10^{-2} \quad (3.4)$$

the values of stepwise dissociation constants of polyprotic acids typically decrease, usually by a factor of 10^4 to 10^6 for each dissociation step. This behavior arises due to

electrostatic forces that make it far more difficult to remove a positive proton from a negative ion such as HSO_4^- than from a molecule that is uncharged such as H_2SO_4 , McMurry et al. (2001).

3.3.1 Solution Concentration Calculation

The sulfuric acid solution is made in five gallon batches. Making large batches of the solution ensures a homogeneous solution between experiments. The details of making a 1 N H_2SO_4 solution are given below. The five-gallon batches of 1 N H_2SO_4 solution are mixed according to the determined concentration, as follows:

$$1 \text{ M} = \text{mass/ L/ GFW} \quad (3.5)$$

$$1 \text{ N} = 1 \text{ M} \times Z \quad (3.6)$$

where Z is the number of liberated hydroxide ions, M is the molarity, and N is normality of the solution:

$$1 \text{ M} = \text{mass/ L/ 98} \quad (3.7)$$

$$1 \text{ N} = 1 \text{ M} \times Z (\text{H}_2\text{SO}_4=2) = \text{mass/ L/ 49} \quad (3.8)$$

The liquid density of the reagent grade sulfuric acid is 1.84 g/cm^3 . This density value gives a final concentration of:

$$1 \text{ N H}_2\text{SO}_4 = \frac{49}{1.84} = 26.6 \frac{\text{cm}^3}{\text{L}} \quad (3.9)$$

given the above information, the amount of sulfuric acid that must be utilized to make a five-gallon batch of 1 normal sulfuric acid solution can be calculated.

$$1 \text{ cm}^3 = 1 \text{ mL} \quad (3.10)$$

$$5 \text{ gallon} \times \frac{4 \text{ qt}}{1 \text{ gallon}} \times \frac{1 \text{ L}}{1.075 \text{ qt}} = 18.92 \text{ L} \quad (3.11)$$

$$26.6 \frac{\text{cm}^3}{\text{L}} \times 18.92 \text{ L} = 503.2 \text{ cm}^3 \quad (3.12)$$

$$503.2 \text{ cm}^3 \times \frac{1 \text{ mL}}{1 \text{ cm}^3} = 503.2 \text{ mL} \approx 0.5 \text{ L} \quad (3.13)$$

Therefore, for a 1 N H_2SO_4 solution, 0.5 L of concentrated sulfuric acid needs to be utilized in five gallons of water.

3.4 Electrochemical Cell

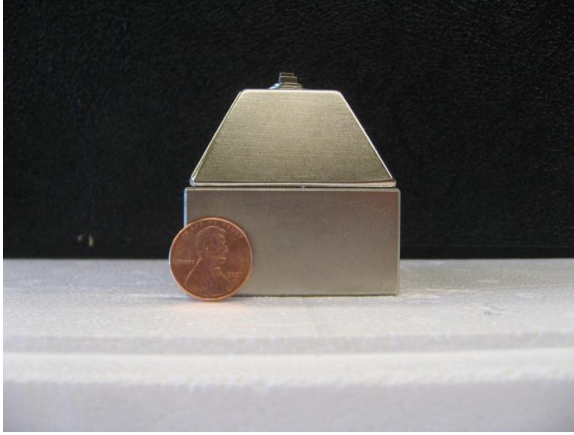
The electrochemical cell contains the steel sample acting as the cathode, two magnet towers, a graphite anode rod, and the Standard Calomel Electrode (SCE) reference electrode. Each magnet tower produces a continuous magnetic field as large as 1.0 Tesla (T). The hydrogen charging system consists of the electrolytic cell and the Princeton Applied Research Potentiostat/Galvanostat Model 273A. The electrochemical impedance spectroscopy arrangement combines the cathodic charging arrangement with the use of the Schlumberger Research Instruments (now Solartron Analytical) 1255 HF Frequency Response Analyzer to perform impedance analysis.

3.4.1 Magnet Towers

The magnet towers, shown below in Figure 3.4, consisted of four parts: (1) the base, (2) the pyramid, (3) magnet stack, and (4) the PVC separator. The base is a 2 in. x 2 in. x 1 in. (50.8 mm x 50.8 mm x 25.4 mm) rectangle of neodymium, the pyramid has a 2in. x 2in. (50.8mm x 50.8 mm) base and tapers to a 1 in. x 1 in. (25.4mm x 25.4 mm) square and is 1 inch (25.4 mm) thick, the magnet stack consists of a series of magnets with successively smaller surface areas with the smallest magnet having square dimensions of 4 mm x 4 mm. All of the neodymium magnets have a thin nickel plating to prevent the oxidation of neodymium. This magnet-stacking configuration was utilized to create an approximate static magnetic field of 1 Tesla at the center of the field.

3.4.2 Reference Electrode

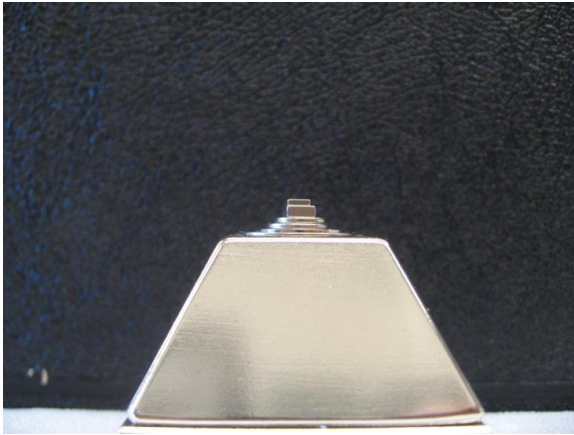
The absolute potential of a single electrode cannot be measured and all potential measurements are performed with respect to a reference electrode. Ideally, a reference electrode should be reproducible and reversible (Bard et al. 2001). Mercury, being a noble liquid metal, is easy to purify and has a surface that is completely reproducible. For this reason, mercury is considered to be one of the best electrode metals. Many mercurous salts have very low solubility in water and are suitable for the preparation of an electrode (Newman 1991). The disadvantage of the mercury-mercurous salt reference electrode is that mercury has two valence states. The calomel electrode is the most common of all mercury-mercurous salt electrodes. The calomel electrode is best used in acid solutions. For the experiments performed in this research, the saturated calomel electrode (SCE) was used.



(a)



(b)



(c)



(d)

Figure 3.4: Magnet tower assembly, each magnet tower produces a magnetic field strength of 1.0 T. (a) the overall height of an individual magnet tower is two inches. Each tower consists of a 2 inch \times 2 inch \times 1 inch (50.8 mm \times 50.8 mm \times 25.4 mm) base and a 2 inch \times 2 inch \times 1 inch (50.8 mm \times 50.8 mm \times 25.4 mm) pyramid. (b) Top view of the magnet towers. (c) View of the magnet stack used to bring the magnetic field strength to 1.0T. (d) The two magnet towers separated by a piece of PVC. The PVC was used to achieve the desired field strength of 0.7 T. Changing the length of the PVC separator will change the strength of the magnetic field. The magnets were isolated from the solution by coating them in a silicone calking and then in acrylic paint. The poles of the magnet towers, separated by the PVC, were covered in a two-part epoxy resin.

3.4.3 Counter Electrode (Anode)

The counter electrode or anode used in the hydrogen charging experiments was a graphite rod. At the beginning of every charging experiment, the graphite rod was polished with 600 grit sand paper to expose fresh anode surface and then rinsed with de-ionized water. The graphite rod is 12 inches (304.8 mm) in length and 0.25 inches (6.35 mm) in diameter. Graphite was chosen as the anode material due to the fact that it is cheap and was readily available.

3.4.4 Working Electrode (Cathode)

The working electrode or cathode, for the hydrogen charging experiments was made of either X52, X70, or X80 API linepipe steel. All steel samples were machined to the same specifications and dimensions. The dimensions of the charging specimens were: 0.3125 inches (w) \times 0.125 inches (d) \times 0.5 inches (h) (7.9 mm \times 3.175 mm \times 12.7 mm). All have samples have approximately the same mass ($m = 0.8$ g). The sample geometry is shown in Figure 3.5.

3.5 Cathodic Hydrogen Charging Experiments

Hydrogen charging experiments were performed on three different API linepipe steel grades: X52, X70, and X80. The samples were machined from sections of linepipe steel in the longitudinal direction. The dimensions of the charging specimens were: 0.3125 inches (w) \times 0.125 inches (d) \times 0.5 inches (h) (7.9 mm \times 3.175 mm \times 12.7 mm). Charging experiments were carried out for times ranging from two to twelve hours.

When performing hydrogen charging experiments, the voltage can be set at a constant value or the current can be set at a constant value. When the voltage is set at a constant value the working electrode is said to be under potentiostatic control and when the current is set at a constant value the working electrode is said to be under galvanostatic control.

The experiments were run under potentiostatic control (constant potential) at a value of $E = -0.55$ V. The potential must be a negative value since the desired outcome is to have the hydrogen ions migrate to the cathode and be absorbed into the metal. Under potentiostatic control the current is measured as a function of time. A typical plot for a hydrogen charging experiment is shown below in Figure 3.6. The plot in Figure 3.6 gives the current density as a function of time. The Princeton Applied Research Potentiostat/Galvanostat 273A records the

output in this format. All of the hydrogen charging experiments were performed on the Princeton Applied Research Potentiostat/Galvanostat 273A. The hydrogen content was assessed by using the LECO Hydrogen Determinator.

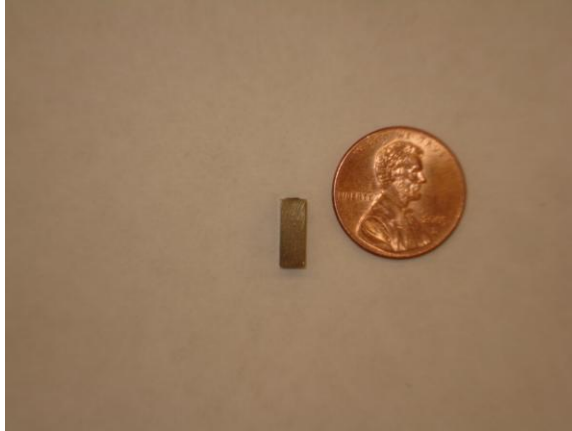


Figure 3.5: This figure shows the geometry and dimensions of the hydrogen charging samples. The size of the hydrogen charging sample was dictated by the LECO Hydrogen Determinator. Hydrogen charged samples tested in the LECO cannot have a mass greater than one gram.

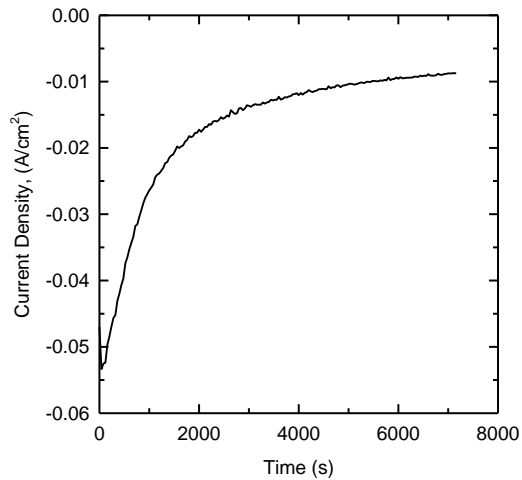


Figure 3.6: Typical plot for a hydrogen charging experiment. This data shows the current transient for a two hour hydrogen charging experiment on X80 linepipe steel. The magnets were in the electrochemical cell for this experiment.

3.5.1 Hydrogen Charging: Variation in Magnetic Field Strength

To determine the effect of varying magnetic field strength on hydrogen absorption, API X80 linepipe samples were cathodically charged at magnetic field strengths of 0.0, 0.3, 0.5, and 0.7 Tesla for two hours. The strength of the magnetic field is controlled by changing the length of the PVC separator between the poles of the magnet towers, Figure 3.7. The magnetic field strength was measured using a Gauss meter. A magnetic field strength of 0.7 T was the highest magnetic field strength that could be attained and still have the sample fit between the magnet poles.



Figure 3.7: The strength of the magnetic field is controlled by changing the length of PVC between the poles of the magnets.

3.5.2 Hydrogen Charging: The Effect of Stress on Hydrogen Absorption

The effect of stress on hydrogen absorption was assessed by machining tensile samples (ASTM E8) from a section of X80 linepipe steel. The tensile samples were machined from the longitudinal direction of the linepipe section. To achieve different levels of stress in the API X80 linepipe steel tensile samples, the samples were stressed to three different stress levels: 90 ksi (621 MPa) before UTS (Ultimate Tensile Strength), UTS, and 90 ksi (621 MPa) after UTS. The samples were then removed from the tensile machine, and sectioned above the neck. The hydrogen charging samples were taken from the sectioned tensile sample, in the form of a cylinder, and had dimensions of 0.25 inch (h) \times 0.25 inch (d) (6.35 mm \times 6.35 mm). The circular cylinders were then drilled and tapped with a #3-48 drill bit to a 0.125 inch (3.175 mm) depth. The sample geometry is shown below in Figure 3.8. The stressed hydrogen charging

samples were charged at a magnetic field strength of 0.7 T for a time of two hours. The open circuit potential was measured for one hour prior to the hydrogen charging experiment

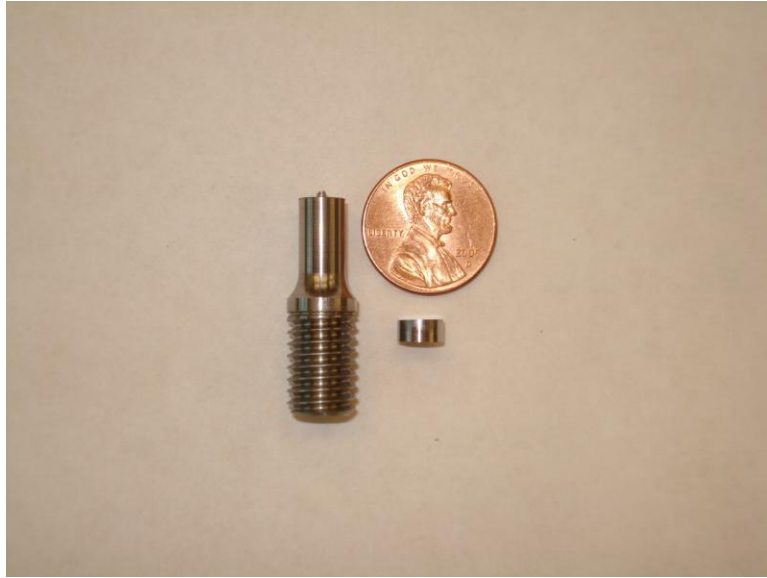


Figure 3.8 E8 tensile sample that has been sectioned is on the left of the figure. Below the penny, is the hydrogen charging sample. All hydrogen charging samples, for the stress experiments were taken from the neck of the tensile sample.

3.6 Potentiodynamic Polarization Experiments

Potentiodynamic polarization experiments were performed on API X80 linepipe steel at four different magnetic field strengths: 0.0, 0.3, 0.5, and 0.7 Tesla. The polarization experiments were performed according to ASTM G5 – 94. The potential was swept from -2 V to +2 V at a sweep rate of 0.1667 mV/s. For the potentiodynamic polarization experiments, the X80 linepipe steel samples had dimensions of 5 mm × 5 mm × 10 mm. and were drilled and tapped with #3-48 to a depth of 2.5 mm. Prior to experiment, the samples were rinsed in deionized water and then cleaned with acetone. After cleaning, the samples were cast in a two-part epoxy resin and allowed to cure for nine hours. Casting the sample in epoxy resin served two purposes: (1) it electrically isolated the sample, and (2) maintained a constant surface area from one experiment to another. Once the epoxy resin was fully cured, one of the sample faces was exposed using a belt sander, and finally polished to a 600 grit finish. The exposed surface area used for the potentiodynamic experiments was 0.5 cm².

The potentiodynamic experiments consisted of two parts: (1) open circuit potential measurement, and (2) potentiodynamic experiment. Prior to the start of a potentiodynamic polarization experiment the open circuit potential was measured for three hours. After three hours of open circuit potential measurement, the potential would reach the steady state potential or the corrosion potential. After the three hour open circuit potential measurement, the potentiodynamic polarization experiment would begin. A potentiodynamic polarization experiment, swept from -2 V to +2 V at a sweep rate of 0.1667 mV/s would take approximately 6.5 hours. Therefore, a full experiment, including open circuit potential measurement, would take approximately 9.5 hours.

3.7 Electrochemical Impedance Spectroscopy Experiments

Electrochemical Impedance Spectroscopy (EIS) experiments were performed on API X80 linepipe steel at different magnetic field strengths. The magnetic field strengths were: 0.0, 0.3, 0.5, and 0.7 Tesla. The experiments were conducted according to ASTM G106 – 89. All EIS experiments were potentiostatically controlled at a voltage of -0.55 V. The open circuit potential was measured for one hour before the EIS experiment began. The frequency was swept from 10^5 Hz – 0.1 Hz for the EIS experiments

The X80 linepipe steel samples, used for the EIS experiments, had dimensions of 5 mm × 5 mm × 10 mm. and were drilled and tapped with #3-48 to a depth of 2.5 mm. Prior to experiment, the samples were rinsed in deionized water and then cleaned with acetone. After cleaning, the samples were cast in a two-part epoxy resin and allowed to cure for nine hours. Casting the sample in epoxy resin served two purposes: (1) it electrically isolated the sample, and (2) maintained a constant surface area from one experiment to another. Once the epoxy resin was fully cured, one of the sample faces was exposed using a belt sander, and finally polished to a 600 grit finish. The exposed surface area used for the EIS experiments was 50 mm².

The purpose of the EIS experiments was to obtain kinetic information about the system and determine if the magnetic field induced any change in the electron transfer process occurring at the surface of the electrode.

3.8 Adomian Decomposition Method

The Adomian decomposition method was introduced by George Adomian in 1984, Adomian (1984). The Adomian decomposition method can be used to solve a wide class of linear or nonlinear, ordinary or partial differential equations, and integral equations, Wazwaz (2002).

The method can be used in a very direct fashion without the aid of linearization, or perturbation that may alter the physical behavior of the model under investigation, Wazwaz (2002).

The Adomian decomposition method consists of decomposing the unknown function $u(x, y)$ of any equation into a sum of an infinite number of components given by the following series

$$u(x, y) = \sum_{n=0}^{\infty} u_n(x, y) \quad (3.14)$$

the decomposition method is concerned with finding the individual components u_0, u_2, u_3, \dots of the series given by Equation (3.14). These components can be determined through a recursive relationship that involves simple integrals.

As a means of explaining the basic concepts of the Adomian decomposition method, consider the following linear differential equation

$$\mathbf{L} u + \mathbf{R} u = g \quad (3.15)$$

where \mathbf{L} is a linear differential operator which is assumed to be invertible, and \mathbf{R} is linear differential operator of order less than \mathbf{L} and g is a source term. Applying the inverse of the linear operator \mathbf{L}^{-1} to both sides of Equation (4.15) and solving for u

$$u = f - \mathbf{L}^{-1}(\mathbf{R} u) \quad (3.16)$$

where f represents the terms arising from integrating the source term and the boundary or initial conditions. As was stated above, the solution u is given by an infinite series of components

$$u = \sum_{n=0}^{\infty} u_n \quad (3.17)$$

with the individual components being determined by the following recursive relationship

$$\sum_{n=0}^{\infty} u_n = f - \mathbf{L}^{-1} \left(\mathbf{R} \left(\sum_{n=0}^{\infty} u_n \right) \right) \quad (3.18)$$

To determine the individual components of the recursive relation given by Equation (3.18), the zeroth component, u_0 , is usually defined by the function f , which arises from boundary and initial conditions and integrating the source terms. Therefore, the recursive relation is formally defined by, Wazwaz (2002).

$$u_0 = f \quad (3.19)$$

$$u_{n+1} = -\mathbf{L}^{-1}(\mathbf{R} u_n), \quad n \geq 0 \quad (3.20)$$

For further information on the Adomian decomposition method see Adomian (1984, 1985, 1986, 1987, 1987, 1988, 1990, 1991, 1992, 1993, 1996, 1997).

In the Chapter on Magnetohydrodynamic fluid flow modeling, the Adomian decomposition method is applied to a coupled system of nonlinear ordinary differential equations derived from the boundary layer equations for magnetohydrodynamic fluid flow and mass transport at a vertical electrode. Therefore, the purpose of introducing the Adomian decomposition method is to model the fluid flow and mass transport next to a vertical electrode with the end result being equations that predict the effect of a magnetic field on the limiting current density and mass transport processes.

CHAPTER 4

RESULTS AND DISCUSSION: HYDROGEN CHARGING

4.1 Introduction

In this Chapter the results for the hydrogen charging experiments will be presented and discussed. Cathodic hydrogen charging experiments were performed on API X80, X70, and X52 linepipe steel with and without a magnetic field present in the electrochemical cell. Time, magnetic field strength, and stress were varied to determine their effect on hydrogen absorption. The first series of hydrogen charging experiments were performed on API linepipe steel grades X80, X70, and X52 at a magnetic field strength of 0.7 Tesla and the time was varied from two to twelve hours. API X80 linepipe steel was the only steel grade examined for the variation in magnetic field strength experiments and the stress experiments. For the variation in magnetic field strength experiments, the magnetic field was varied from 0.0 to 0.7 Tesla. Each API X80 linepipe steel specimen was charged for two hours at their respective field strength. For the stress effect experiments, API X80 linepipe steel E8 tensile samples were stressed to three different levels and then cathodically charged for times ranging from two to twelve hours. The three stress levels were 90 ksi pre-UTS, ultimate tensile strength (UTS), and 90 ksi post-UTS. The total hydrogen content was measured with the LECO Hydrogen Determinator

4.2 Hydrogen Charging Results for API X80, X70, and X52 Linepipe Steel Grades

In this Section the results from the timed hydrogen charging experiments for API X80, X70, and X52 linepipe steels will be summarized. For these experiments, the time was varied from two to twelve hours. When the magnetic field was present in the electrochemical cell, it was maintained at a constant value of 0.7 Tesla. The samples were polished to 600 grit prior to experiment. The final surface area was 1.64 cm^2 and the charging solution was 1N H_2SO_4 .

Figure 4.1 shows the results for the hydrogen charging experiments performed on API X80 linepipe steel as a function of time. As can be seen from Figure 4.1 there is no correlation between magnetic field strength and hydrogen absorption. Figure 4.2 shows the results for the hydrogen charging experiments for API X70 linepipe steel. There also appears to be no

correlation between hydrogen absorption behavior and magnetic field strength for X70 linepipe steel. Figure 4.3 gives the results of the hydrogen charging experiments for API X52 linepipe steel. As can be seen from the results presented, there exists no correlation between magnetic field and hydrogen absorption.

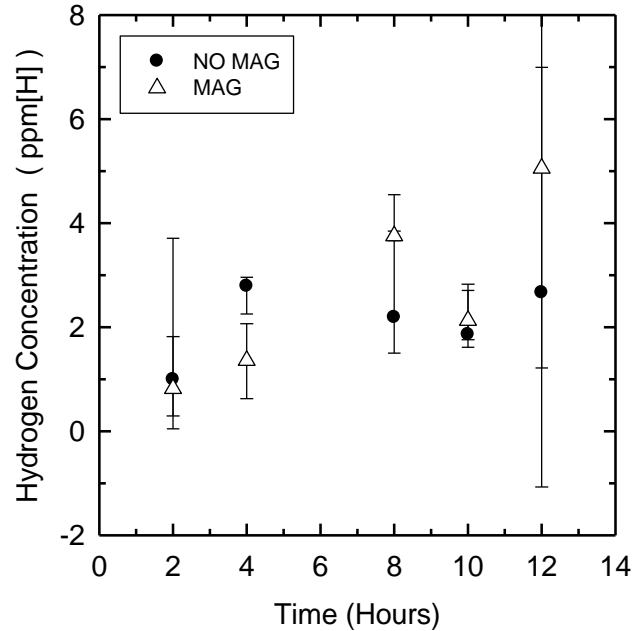


Figure 4.1: Hydrogen charging results for API X80 linepipe steel. This plot shows total hydrogen concentration as a function of time. The triangles represent experiments done in the presence of a magnetic field and the black circles are experiments done without a magnetic field.

4.3 Hydrogen Charging Experiments: Stress Effects

In this section the results from the experiments for the effect of stress and magnetic field strength on hydrogen absorption will be presented. The steel used for these experiments was API X80 linepipe steel. API X70 and X52 linepipe steel grades were not used due to lack of material. The samples of API X80 linepipe steel were taken from a piece of X80 linepipe and machined into sub-sized E8 tensile samples. The tensile samples were taken in the longitudinal direction. The magnetic field strength used for these experiments was 0.7 Tesla.

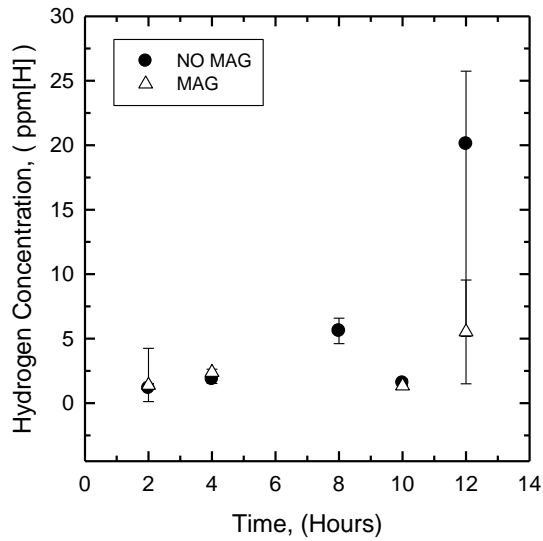


Figure 4.2: Hydrogen charging results for API X70 linepipe steel. This plot shows total hydrogen concentration as a function of time. The triangles represent experiments done in the presence of a magnetic field and the black circles are experiments done without a magnetic field.

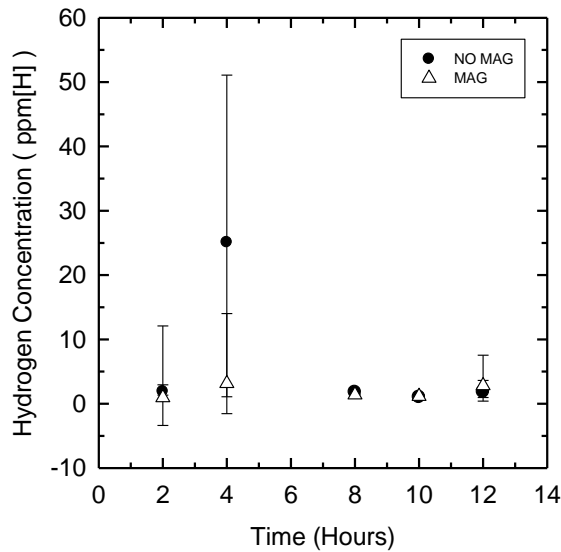


Figure 4.3: Hydrogen charging results for API X52 linepipe steel. This plot shows total hydrogen concentration as a function of time. The triangles represent experiments done in the presence of a magnetic field and the black circles are experiments done without a magnetic field.

To assess the effect of stress on hydrogen absorption, the API X80 linepipe tensile samples were stressed to three different stress levels and charged in a 0.7 T magnetic field for times ranging from two to twelve hours. The three stress levels were 90 ksi pre-UTS, UTS, and 90 ksi post-UTS. Figure 4.4 summarizes the results for the hydrogen charging experiments performed on API X80 linepipe steel at all stress levels. As can be seen in Figure 4.4, there exists no real trend between magnetic field strength, stress, and time. However, the type of trend that is expected is shown at the twelve hour time point. The most hydrogen is expected to be absorbed at the highest stress level (90 ksi post-UTS) and the least amount at the 90 ksi pre-UTS stress level. At the two hour time point there is only one data point, the lack of data shown at this time point is due to problems with the LECO Hydrogen Determinator.

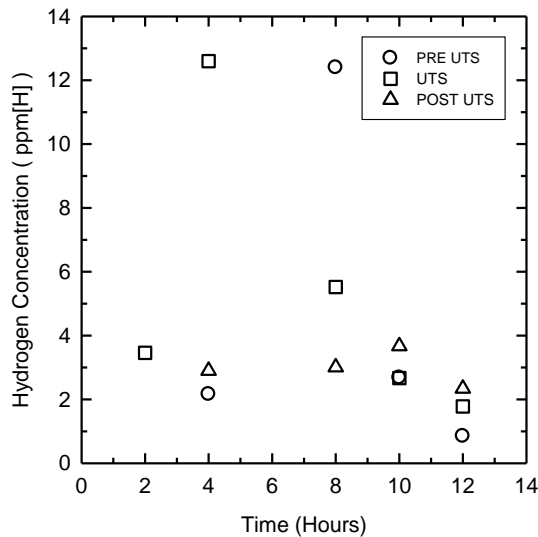


Figure 4.4: Comparison plot of all Hydrogen charging results for API X80 linepipe steel. This plot shows total hydrogen concentration as a function of time. All of the stress levels are represented on this plot. The open-circles represent the pre-UTS experiments, the open-squares represent the UTS experiments, and the open-triangles represent the post-UTS experiments.

4.4 Hydrogen Charging Experiments: Magnetic Field Effects

The results from the magnetic field strength effect experiments are presented in this section. For these experiments, the magnetic field strength was varied from 0.0 to 0.7 Tesla. Each API X80 linepipe steel sample was cathodically charged for two hours at their respective magnetic field strength. The open circuit potential was measured for one hour prior to the

beginning of the cathodic hydrogen charging experiment. All samples were polished to a 600 grit finish and cleaned with acetone prior to experiment. The final surface area was 1.64 cm^2 .

Figure 4.5 gives the results for the magnetic field strength effect experiments. As can be seen from the results, there is a correlation between magnetic field strength and hydrogen absorption. The most hydrogen is absorbed by the steel when the magnetic field strength is 0.7 Tesla. For a charging time of two hours, the total hydrogen content is approximately doubled.

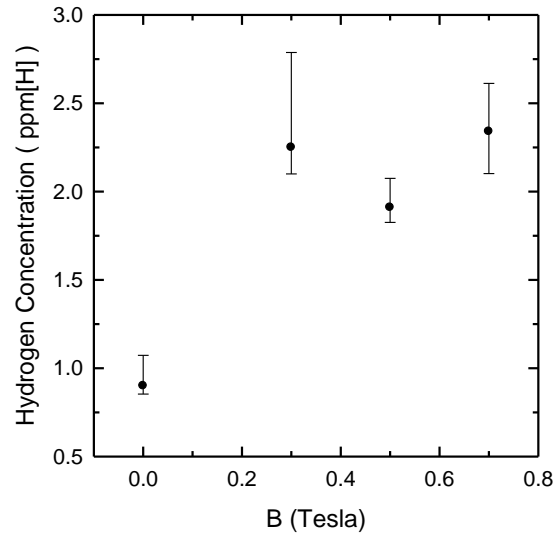


Figure 4.5: Hydrogen charging results for API X80 linepipe steel. This plot shows total hydrogen concentration as a function of magnetic field strength. The magnetic field strengths used for this series of experiments were 0, 0.3, 0.5, and 0.7 T. A magnetic field strength of 0.7 T appears to have the largest effect on hydrogen absorption.

4.5 Discussion: Hydrogen Charging Results

In this Section the results from the cathodic hydrogen charging experiments performed on API X52, X70, and X80 linepipe steel grades will be discussed. From the results given in Figures 4.1 – 4.4, it can be seen that there is no real correlation between magnetism, stress, and hydrogen absorption; reasons will be given as to why this is the observed behavior. However, as can be seen in Figure 4.5, there is a direct correlation between magnetic field strength and hydrogen absorption.

This Section will begin with a discussion of the hydrogen absorption mechanism, or more directly, what are the electrochemical reactions that lead to a hydrogen atom being absorbed into

the metal lattice. Next, the magnetic forces that are present at the electrode/electrolyte interface will be summarized. It will be demonstrated that these magnetic forces act to increase the flux of ions to the surface of the electrode. The observance of the formation of a passivating cathodic film will be discussed. It is believed that cathodic film formation leads to decreased hydrogen absorption by the API X80, X70, and X52 linepipe steel grades.

4.5.1 Hydrogen Absorption Mechanism

The potential of an electrode strongly affects the kinetics of reactions occurring on the electrode surface, Bard et al. (2002). The kinetics of electron transfer reactions are governed by the Butler-Volmer equation

$$i = i_0 [\exp(-\alpha f \eta) - \exp((1-\alpha)f \eta)] \quad (4.1)$$

where α is the transfer coefficient, η is the potential, $f = F/R T$ with F being Faraday's constant, T is temperature and R is the gas constant, and i_0 is the exchange current density. In terms of cathodic hydrogen charging, the charge transfer reaction of interest is the hydrogen ion reduction reaction



Reactions, chemical or electrochemical in nature, can be explained and visualized in terms of progress along a reaction coordinate (activated complex theory). However, when considering electrochemical reactions, the shape of the energy surface is dependent on the electrode potential as shown schematically below in Figure 4.6. In terms of this research, the interest lies in the reduction reaction, panel (c), of Figure 4.6. Since the reaction given by Equation (4.2) is being driven at a fairly negative potential, only the cathodic portion of the Butler-Volmer equation is important

$$i = i_0 \exp(-\alpha f \eta) \quad (4.3)$$

this is equivalent to saying the reaction given by Equation (4.2) is effectively irreversible.

The absorption of hydrogen is believed to occur in a series of steps and it is generally accepted that in the first step of the absorption process H^+ is discharged to form an adsorbed atom on the electrode surface, Pound et al. 1993. In acidic solutions, for example, the hydrogen absorption mechanism is given by the following sequence of reactions



where Equation (4.4) produces an adsorbed hydrogen atom. Equation (4.4) is known as the Volmer reaction. The second step leads to formation of molecular hydrogen by either the electrochemical reaction of an adsorbed hydrogen atom with a proton, known as the Heyrovsky reaction, or by the chemical reaction between two adsorbed hydrogen atoms, which is known as the Tafel reaction. These reactions are shown below



alternatively, the adsorbed hydrogen atoms can diffuse directly into the metal, as shown below, Landolt (2007).



the reaction sequence given by Equations (4.4) – (4.7) is shown schematically in Figure 4.7.

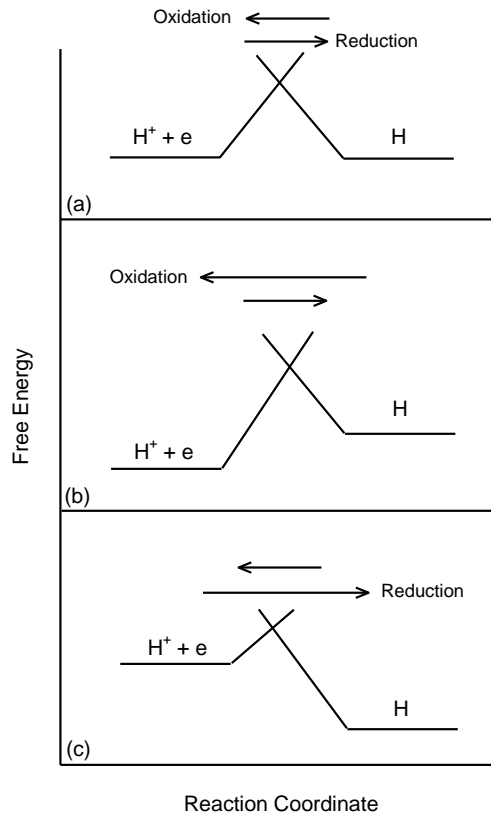


Figure 4.6: Schematic diagram of the free energy curves associated with an electrochemical reaction; (a) schematic corresponding to equilibrium, (b) schematic corresponding to a more positive potential promoting oxidation, and (c) schematic corresponding to a more negative potential promoting reduction.

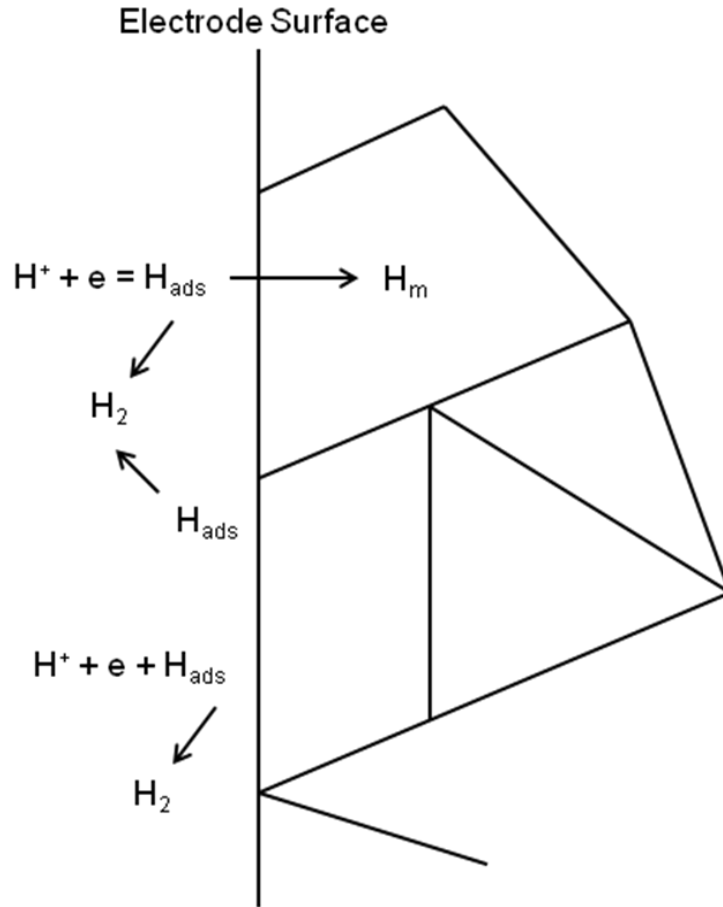


Figure 4.7: Schematic diagram showing the possible reaction paths for hydrogen absorption into a metal electrode. H_m represents a hydrogen atom that has been absorbed directly into the metal and is free to diffuse into the bulk of the lattice.

4.5.2 Magnetic Forces Present in the Electrolyte

In this Section, the magnetic forces present in the electrolyte will be discussed. It is believed that these magnetic forces are, in part, responsible for the increased hydrogen absorption observed in API linepipe steel grades X52, X70, and X80. These forces act to enhance transport or delivery of hydrogen ions to the electrode surface.

There are two principal magnetic forces present in the electrolyte: the Lorentz force and the Magnetic force. The Lorentz force is given as the cross-product of the current and the magnetic field

$$F_L = i \times B \quad (4.8)$$

and the Magnetic force is given as

$$F_{\text{mag}} = \frac{\chi_m B^2 \nabla C}{2 \mu_0} + \frac{\chi_m C B \nabla B}{\mu_0} \quad (4.9)$$

where the first term on the right hand side of Equation (4.9) is the concentration gradient force and the second term on the right hand side of Equation (4.9) is the magnetic field gradient force.

Using the Nernst-Planck equation it can be shown that the two forces given in Equation (4.9) enhance the transport of hydrogen ions to the metal/electrolyte interface. To begin, write

$$J_j = C_j M_j F \quad (4.10)$$

where J_j represents the flux of species j , C_j is the concentration of species j , M_j is the mobility of species j , and F is the driving force. Equation (4.10) can be rewritten as

$$J_j = -\frac{C_j D_j}{R T} \frac{d \mu_j}{d x} + C_j v(x) \quad (4.11)$$

where D_j is the diffusivity of species j , R is the gas constant and T is the temperature, μ_j is the chemical potential of species j . The last term in Equation (4.11) takes into account the convective motion of the electrolyte. Taking into account all potentials that contribute to the flux of ions in solution, a modified Nernst-Planck equation is obtained

$$J_j(x) = -\left(\frac{C_j D_j}{R T}\right) \left[\frac{d}{d x} (R T \ln C_j) + \frac{d}{d x} (z_j F \phi) - \frac{d}{d x} \left(\frac{\chi_m C_j B^2}{2 \mu_0} \right) \right] + C_j v(x) \quad (4.12)$$

taking the derivatives and simplifying gives the Nernst-Planck equation that takes into account the effect of a magnetic field

$$J_j(x) = -D_j \frac{d C_j(x)}{d x} - \frac{z_j F}{R T} D_j C_j \frac{d \phi(x)}{d x} + \frac{C_j D_j \chi_m B^2}{2 R T \mu_0} \frac{d C_j(x)}{d x} + \frac{C_j D_j \chi_m C_j B}{2 R T \mu_0} \frac{d B(x)}{d x} + C_j v_{\text{mag}}(x) \quad (4.13)$$

where the first term represents diffusion, the second term represents migration, the third and fourth terms represent migration due to magnetic forces, and the last term represents convection. χ_m is the molar magnetic susceptibility, B is the magnetic field strength, ϕ is the potential, μ_0 is the permeability of free space, and $v_{\text{mag}}(x)$ is the velocity induced by the magnetic field. The Lorentz force was not included in this derivation but is considered in detail in the chapter on magnetohydrodynamic fluid flow modeling.

Equation (4.13) shows how a magnetic field increases the transport/flux of ions to the metal/electrolyte interface. Equation (4.13) is a nonlinear equation in concentration and magnetic field strength and is coupled to the electrical potential. The electrical potential distribution could be obtained by solving Poisson's equation.

4.5.3 Cathodic Film formation

When a piece of iron is placed in sulfuric acid, the iron will begin to corrode, with result of such a corrosion process being the formation of a passive film. Previous research on the topic of cathodic film formation has shown that the film is composed primarily of $\text{Fe}(\text{OH})_2$ and FeSO_4 , Dey et al. (2006). X-Ray diffraction was used to identify the corrosion products. In their work, they found that the film reached a thickness of six micrometers after an exposure time of fifty hours in H_2SO_4 .

It is believed that the formation of corrosion product on the sample surface during cathodic hydrogen charging leads to erratic charging results. It also believed that a magnetic field promotes the formation of corrosion product. As can be seen in Figure 4.8, when a magnetic field is present in the electrochemical cell, the potential is shifted to more positive potentials, which supports this claim. The shift in open circuit potential is also known to be greater, the stronger the magnetic field.

The correlation between a positive shift in open circuit potential and magnetic field strength can be explained with the use of the Pourbaix diagram for the iron-water system, Figure 4.9. The vertical blue line in Figure 4.9 indicates the direction the potential can shift when a magnetic field is applied. For example, when the magnetic field strength is high, the potential may shift into regions marked A or B (passive regions). If the magnetic field strength is not very strong, the potential may shift into region C (active corrosion) and when the magnetic field is relatively weak, the potential may stay in region D (immunity). Lastly, there is experimental evidence obtained from the SEM analysis, Figures 2.4 and 2.5 in Chapter 2, that a passive film is present on the sample after a hydrogen charging experiment.

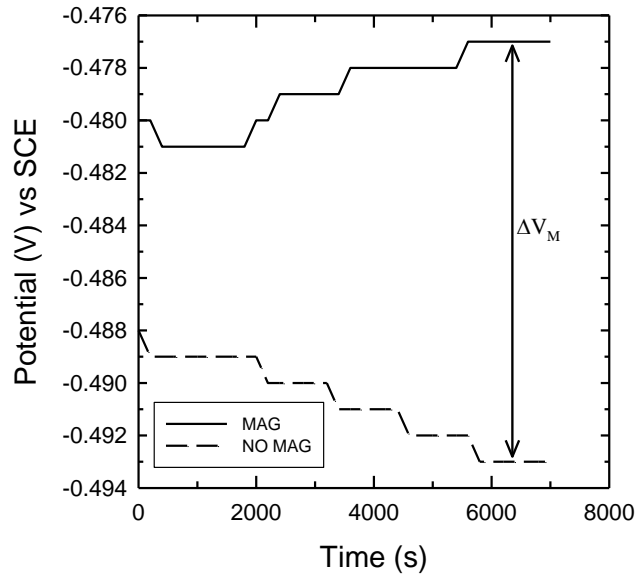


Figure 4.8: Shift in the open circuit potential when a magnetic field is applied during cathodic hydrogen charging experiments on X80 linepipe steel.

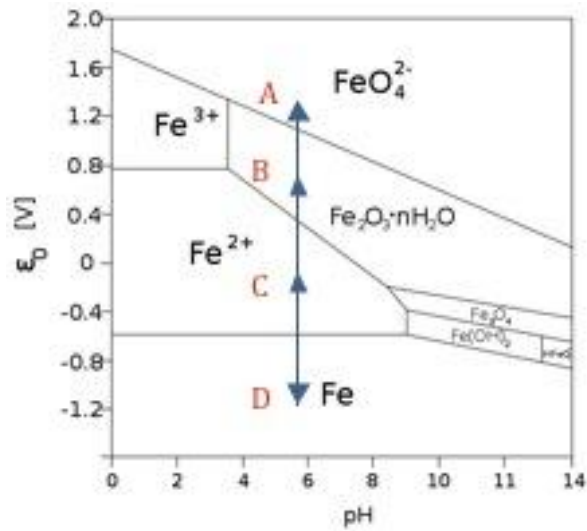


Figure 4.9: Schematic Pourbaix diagram for the iron-water system. The blue arrow indicates the direction in which the potential can shift when a magnetic field is applied to the system. A strong magnetic field could push the potential into region A (passive film formation), while a weak magnetic field could shift the potential into region C (active corrosion), and region D would be no magnetic field (immunity).

CHAPTER 5

RESULTS AND DISCUSSION: ELECTROCHEMICAL CORROSION STUDIES FOR X80

5.1 Introduction

In this Chapter the experimental results for the corrosion experiments performed in the presence of a magnetic field will be presented and discussed. Two main experimental techniques were used to assess the corrosion behavior of API X80 linepipe steel in the presence of a magnetic field: (1) Potentiodynamic polarization and (2) Electrochemical Impedance Spectroscopy (EIS).

5.2 Corrosion Studies: Potentiodynamic Polarization Experiments

In this Section the results from the potentiodynamic polarization experiments will be presented. For these experiments, only API X80 linepipe steel grade was analyzed. The experiments were performed at four different magnetic field strengths: 0.0, 0.3, 0.5, and 0.7 Tesla. The voltage was swept from negative two volts to positive two volts at a sweep rate of 0.1667 mV/s. The electrolyte was 1N H₂SO₄.

Figures 5.1 – 5.3 give the potentiodynamic polarization results for API X80 linepipe steel grade. Figure 5.1 compares the results from a potentiodynamic polarization experiment performed at a magnetic field strength of 0.0 Tesla and 0.3 Tesla. Figure 5.2 compares the results from a potentiodynamic polarization experiment performed at a magnetic field strength of 0.0 Tesla and 0.5 Tesla. Figure 5.3 compares the results from a potentiodynamic polarization experiment performed at a magnetic field strength of 0.0 Tesla and 0.7 Tesla. Figure 5.4 compares all potentiodynamic polarization experiments together. The important features to notice in this plot are the shifts in passivation potential and decrease in limiting current density with applied magnetic field. Figure 5.5 gives the intersection of the cathodic and anodic branch of the potentiodynamic polarization plots, which shows the effect of magnetic field on open circuit potential and corrosion current. Figure 5.6 compares the cathodic branches of the potentiodynamic polarization curves at the different magnetic field strengths. These curves show

approximately the same slope, irrespective of magnetic field strength, and a decrease in limiting current density with increasing magnetic field strength.

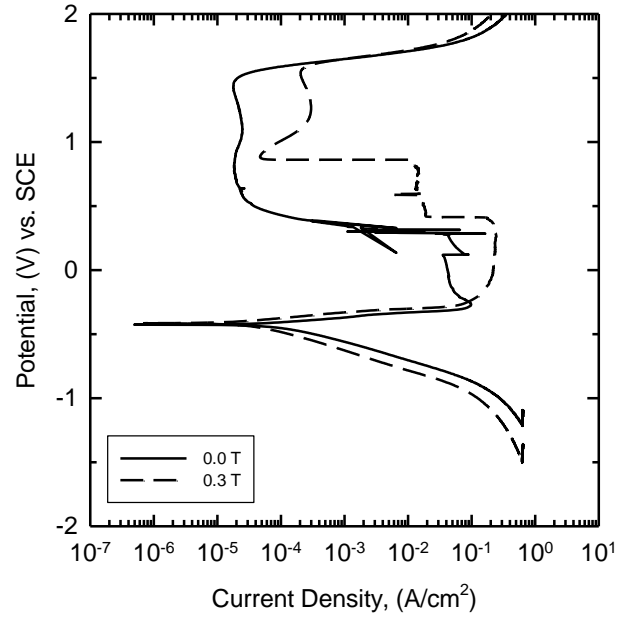


Figure 5.1: Potentiodynamic polarization experimental results for API X80 linepipe steel. The solid line represents a polarization experiment performed at a magnetic field strength of 0.0 Tesla and the dashed line represents a polarization experiment performed at a magnetic field strength of 0.3 Tesla.

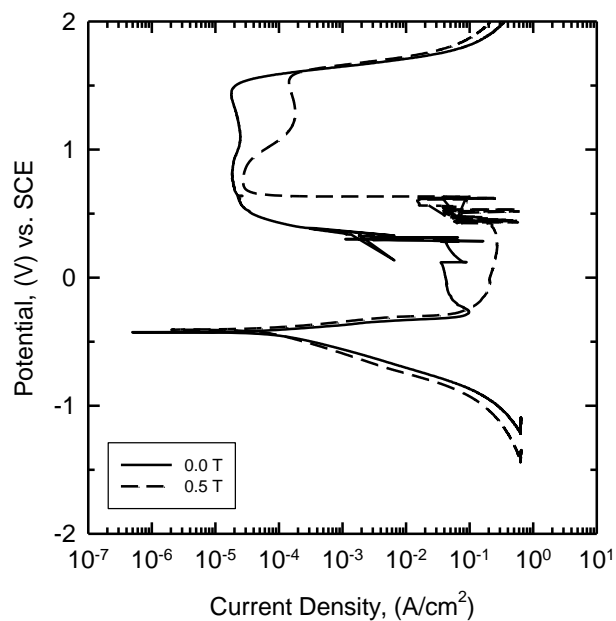


Figure 5.2: Potentiodynamic polarization experimental results for API X80 linepipe steel. The solid line represents a polarization experiment performed at a magnetic field strength of 0.0 Tesla and the dashed line represents a polarization experiment performed at a magnetic field strength of 0.5 Tesla.

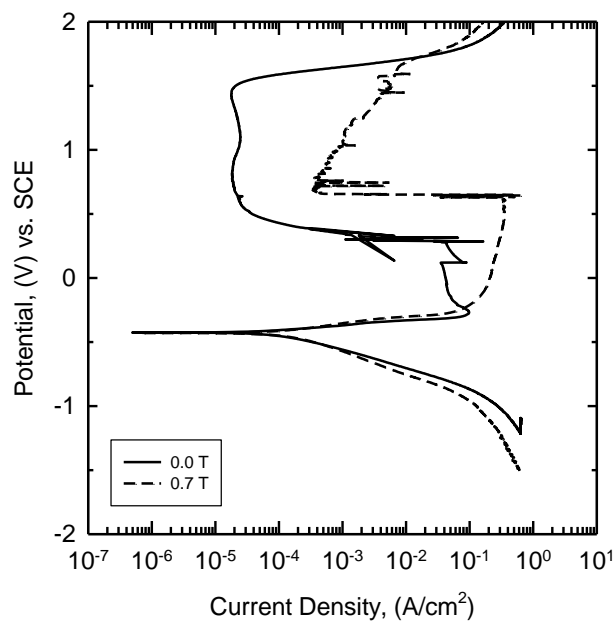


Figure 5.3: Potentiodynamic polarization experimental results for API X80 linepipe steel. The solid line represents a polarization experiment performed at a magnetic field strength of 0.0 Tesla and the dashed line represents a polarization experiment performed at a magnetic field strength of 0.7 Tesla.

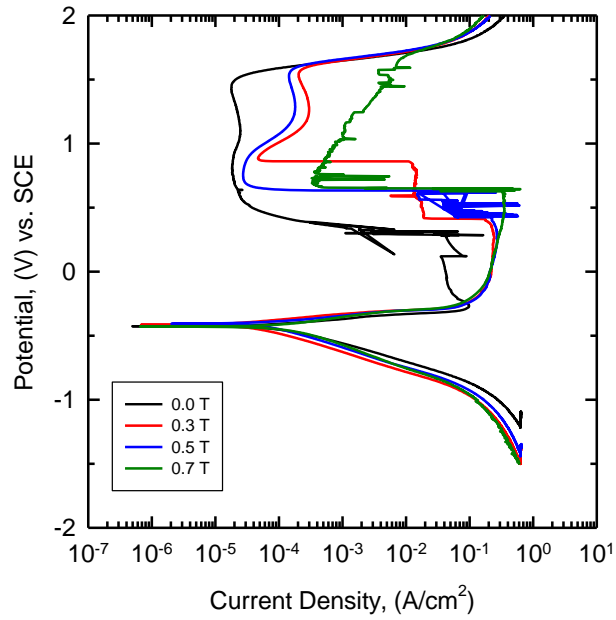


Figure 5.4: Potentiodynamic polarization experimental results for API X80 linepipe steel. This plot gives a comparison of the polarization experiments at all magnetic field strengths. The important elements to notice from this plot are the shifts in passivation potential and decrease in limiting current density with applied magnetic field.

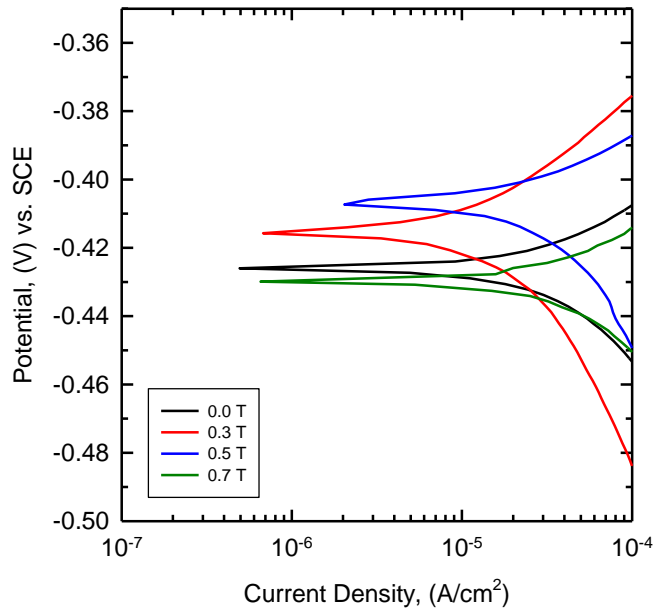


Figure 5.5: This plot shows the variation in open circuit potential and corrosion current with applied magnetic field for X80 linepipe steel.

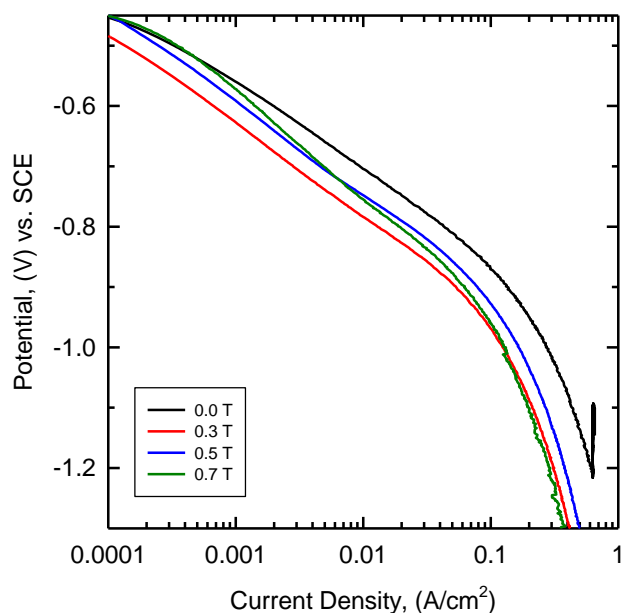


Figure 5.6: This plot shows the cathodic branch of the potentiodynamic polarization curve. Note the decrease in limiting current density with increasing strength of magnetic field. The largest decrease in limiting current density occurs at a magnetic field strength of 0.7 Tesla.

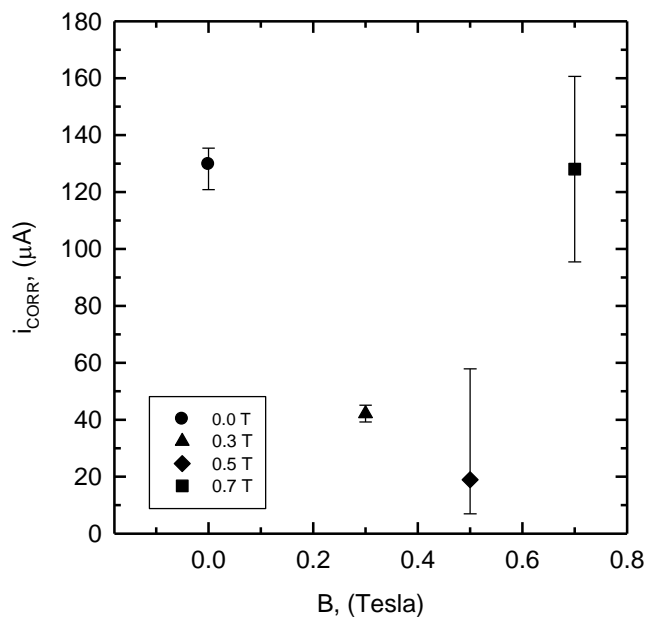


Figure 5.7: Variation in corrosion current with magnetic field. These results are for API X80 linepipe steel in 1N H_2SO_4 .

5.3 Corrosion Studies: Electrochemical Impedance Spectroscopy (EIS)

In this Section the results from the EIS experiments will be presented. For these experiments only API X80 linepipe steel was analyzed. The perturbing signal was 10 mV AC and the DC potential was -0.55 Volts. Figure 5.8(a) compares the Nyquist plot at two different magnetic field conditions: 0.0 and 0.3 Tesla. Figure 5.8(b) shows the Bode diagram at the same magnetic field strength. Figure 5.9(a) shows the Nyquist plot at two different magnetic field strengths: 0.0 and 0.5 Tesla. Figure 5.9(b) gives the Bode diagram at the same magnetic field strengths that are reported in Figure 5.9(a). Figure 5.10(a) shows the Nyquist plot at two different magnetic field strengths: 0.0 and 0.7 Tesla. Figure 5.10(b) gives the Bode diagram at the same magnetic field strengths that are reported in Figure 5.10(a). Figure 5.11 gives a summary of the Nyquist plots at the four different magnetic field strengths: 0.0, 0.3, 0.5, and 0.7 Tesla.

The impedance data presented in Figures 5.8 – 5.11 are indicative of two electrochemical phenomena: electron charge transfer, and film formation. The charge transfer reaction is associated with hydrogen reduction. It can be seen from the impedance data that a magnetic field increases charge transfer resistance and decreased the double layer capacitance. This will be discussed in more detail in Section 5.5.

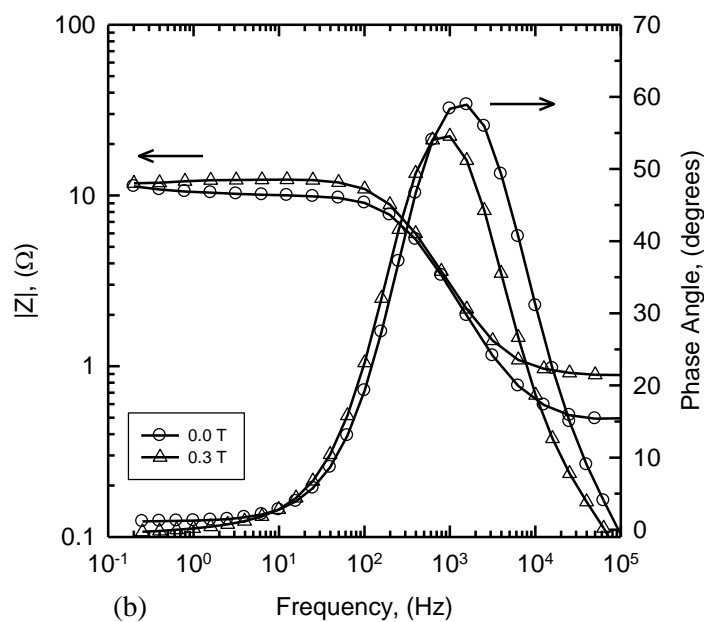
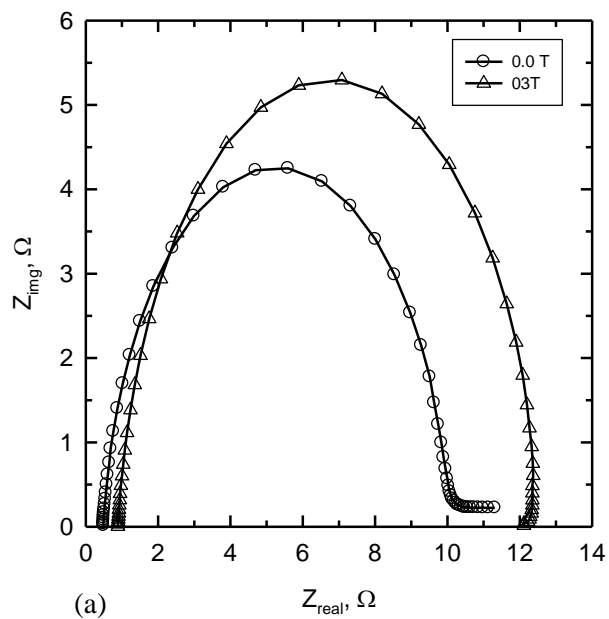


Figure 5.8: Results from the electrochemical impedance spectroscopy experiments on X80 linepipe steel; (a) Nyquist plots, (b) Phase angle and Impedance magnitude. (a) Comparison of the Nyquist plots at 0.0 and 0.3 Tesla, the single capacitive loop is indicative of a charge transfer process occurring on the surface of the electrode.

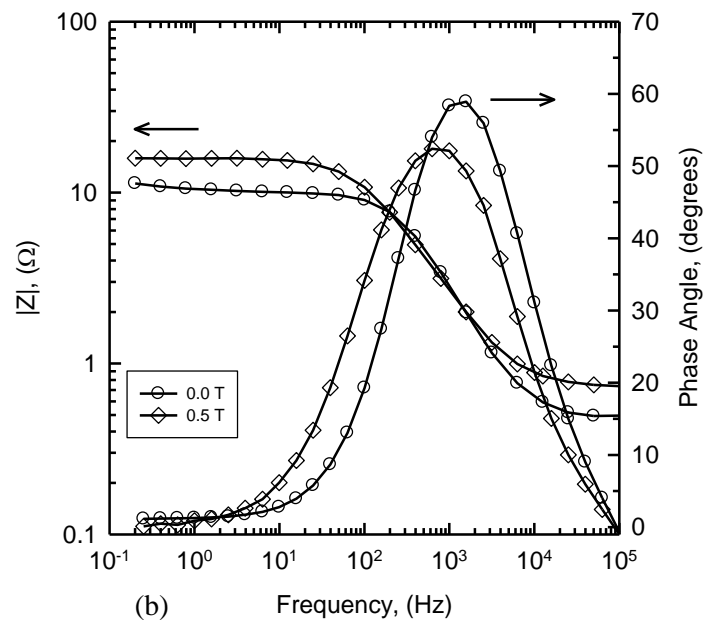
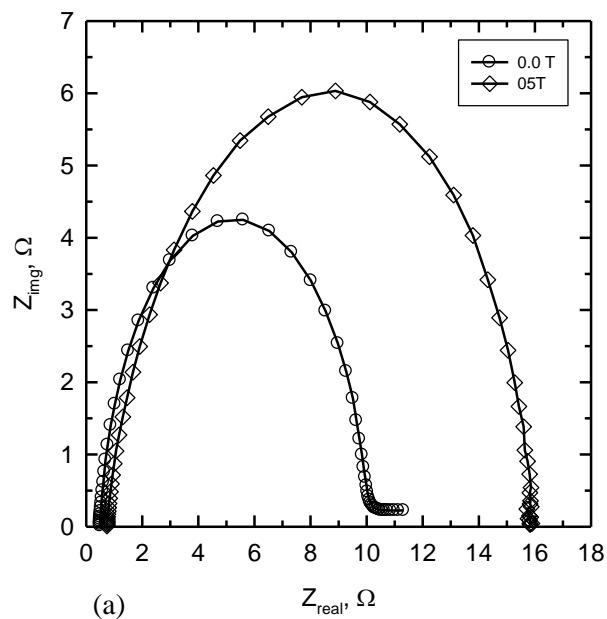


Figure 5.9: Results from the electrochemical impedance spectroscopy experiments on X80 linepipe steel; (a) Nyquist plots, (b) Phase angle and Impedance magnitude. (a) Comparison of the Nyquist plots at 0.0 and 0.5 Tesla, the single capacitive loop is indicative of a charge transfer process occurring on the surface of the electrode.

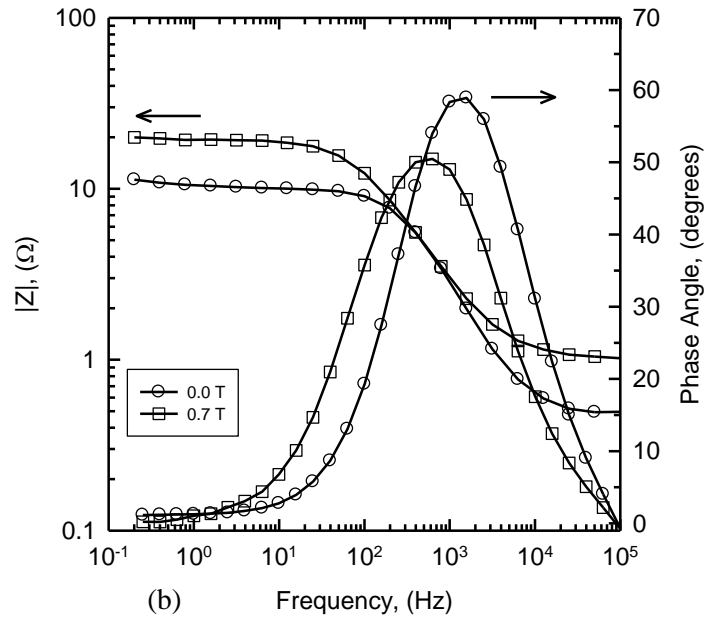
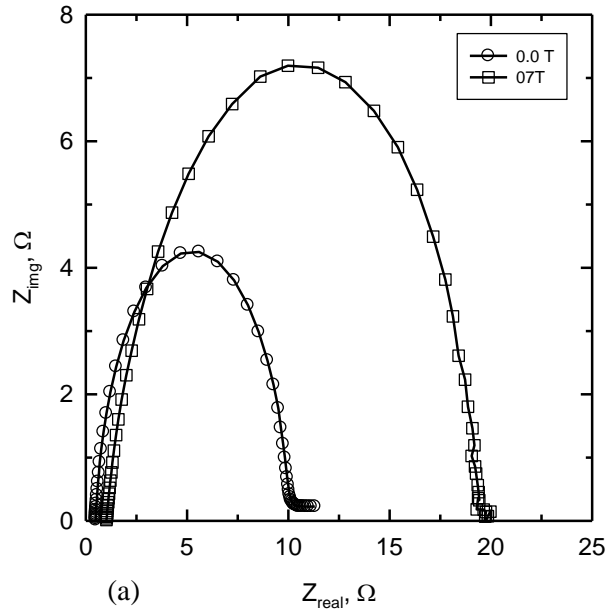


Figure 5.10: Results from the electrochemical impedance spectroscopy experiments on X80 linepipe steel; (a) Nyquist plots, (b) Phase angle and Impedance magnitude. (a) Comparison of the Nyquist plots at 0.0 and 0.7 Tesla, the single capacitive loop is indicative of a charge transfer process occurring on the surface of the electrode.

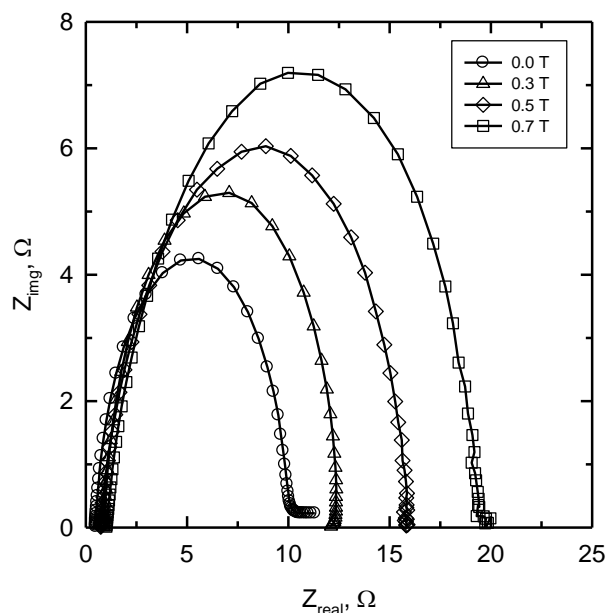


Figure 5.11: Comparison of the Nyquist plots at all of the different field strengths. The data given by the Nyquist plots is indicative of a single charge transfer process occurring on the surface of the electrode. From this data it can be seen that a magnetic field increases the charge transfer resistance.

5.4 Discussion: Potentiodynamic Polarization Experiments

In this Section the experimental results from the potentiodynamic polarization experiments will be discussed. A model for the observed shift in passivation potential will be given. This model attributes the shift in passivation potential to magneto-convective effects and the Lorentz force.

From the results presented in Figure 5.4 it may be stated that a magnetic field does not alter the general shape of the polarization curve, but has a significant effect on the specific currents and potentials which comprise the polarization curve. Figure 5.4 summarizes some of the results from the potentiodynamic polarization experiments. The important features that should be noted from these results are the following: shift in passivation potential, shift in the open circuit potential, and decrease in the limiting current density. The passivation potential is the group of horizontal lines in Figure 5.4 in the Potential range of approximately 0.5 to 1 Volt. The open circuit potential is the region of the plot where the cathodic branch (negative potential values) and the anodic branch (positive potential values) meet. For the results shown in Figure 5.4, the open circuit potential is approximately -0.4 Volts. The limiting current density on the cathodic branch

of the polarization curves at a value of approximately 1 A/cm^2 . In the sections that follow, each one these phenomena will be discussed; to begin, the effect of a magnetic field on the open circuit potential will be analyzed.

5.4.1 Magnetic Field Effects on the Open Circuit Potential (OCP)

At the open circuit potential no current is flowing in the electrochemical cell. Therefore, the observance of an open circuit potential shift is purely a thermodynamic phenomenon. The shift in open circuit potential is shown below in Figure 5.12 and in Figure 5.13. Figure 5.13 shows a plot of open circuit potential as a function of time for API X80 linepipe steel in $1\text{N H}_2\text{SO}_4$ after two hours of immersion at a magnetic field strength of 0.7 Tesla.

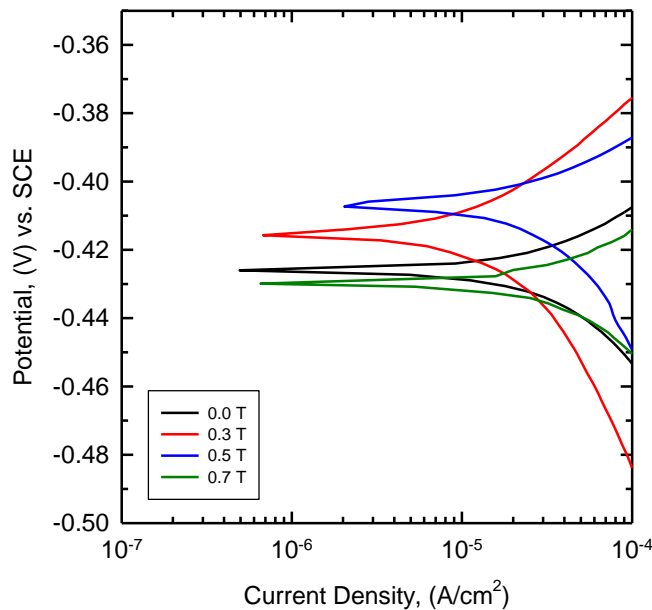


Figure 5.12: Plot depicting the shift in open circuit potential (OCP) with an applied magnetic field. The shift in OCP with an applied magnetic field is a thermodynamic phenomenon.

To show that the shift in OCP is a thermodynamic phenomenon a magnetic work term, ΔMB , is used in the formulation of the Nernst equation. ΔM is the change in magnetization and B represents the magnetic flux density. For this derivation, the total work being done on the system must be considered (internal and external work); therefore, instead of using Gibb's free

energy, Helmholtz free energy must be used. However, start with the First law of thermodynamics to show

$$dE = T dS - P dV - \delta \omega_{\text{ext}} \quad (5.1)$$

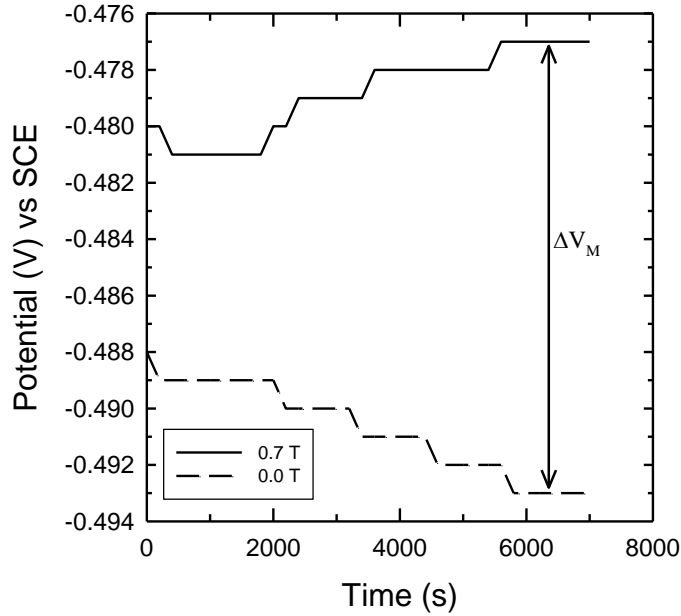


Figure 5.13: Open circuit potential measurements for X80 linepipe steel grade with and without a magnetic field. The solid line is the OCP measurement with the magnetic field. The dashed line is the OCP measurement without the magnetic field. The quantity ΔV_M is the difference in open circuit potential after two hours of immersion in 1 N H_2SO_4 solution. The magnetic field strength is 0.7 Tesla.

At constant temperature and pressure Gibbs free energy is given as

$$dG = -\delta \omega_{\text{ext}} + \sum \mu_i n_i \quad (5.2)$$

where the first term represents the external work being done on the system and the second term is the chemical potential. The external work for an electrochemical system is defined as

$$\omega_{\text{ext}} = -nFE \quad (5.3)$$

therefore, dG can be written as

$$dG = -nFE + \sum \mu_i n_i + RT \ln \frac{[H]}{[H^+]} \quad (5.4)$$

Equation (5.4) is an expression for the external work being done on the system. As was mentioned above, an expression for the total work being done on the system is needed. The

auxiliary function that describes both internal and external work is dA , or Helmholtz free energy. Helmholtz free energy is defined as

$$dA = -d\omega_{\text{int}} - d\omega_{\text{ext}} \quad (5.5)$$

since dG incorporates all of the external work being done on the system, Equation (5.4) can be substituted into Equation (5.5) to give

$$dA = dG - d\omega_{\text{int}} \quad (5.6)$$

the first term on the right hand side of the equals sign is the external work, as defined in Equation (5.4), and the second term is the internal work being done on the system. In this case, the internal work is being done by the magnetic field and is defined as

$$d\omega_{\text{int}} = \Delta M B \quad (5.7)$$

where ΔM represents the change in magnetization and B represents the magnetic flux density. Combining all equations gives the final thermodynamic relationship for the total work being done on the system

$$dA = -nFE + \Delta G^0 + RT \ln \frac{[H]}{[H^+]} - \Delta M B \quad (5.8)$$

assuming unit activity for H and that the system is at equilibrium ($dA = 0$) gives the following

$$nFE = \Delta G^0 - RT \ln[H^+] - \Delta M B \quad (5.9)$$

dividing through by nF gives the modified version of the Nernst equation which accounts for the shift in potential due to a magnetic field

$$E = E^0 - \frac{RT}{nF} \ln[H^+] - \frac{\Delta M B}{nF} \quad (5.10)$$

5.4.2 Magnetic Field Effects on the Limiting Current Density

The cathodic branch of the polarization curve is shown below in Figure 5.14, and the limiting current density is indicated by the nearly vertical part of the curve intersecting the x-axis at approximately 1 A/cm^2 .

Typically, the concentration of reactants and products in the bulk electrolyte is different than the concentration of reactants and products at the electrode surface. This situation leads to a concentration overpotential which varies with the rate of transport of reactants and products to and from the electrode surface, Landolt (2007). For example, at high reaction rates,

cathodic reduction reactions deplete the solution adjacent to the electrode surface of dissolved species leading to a situation shown schematically in the bottom part of Figure 5.15. Figure 5.15 shows a thickening of the diffusion layer (δ) due to a depletion of dissolved species as a result of high rates of cathodic reduction reactions.

The limiting current density is important because it is a measure of maximum reaction rate that cannot be exceeded due to limited rate of diffusion, Jones (1996). δ is referred to as the diffusion layer because the transport of ions next to the electrode surface is dominated by diffusion as opposed to convection. δ is commonly referred to as the Nernst diffusion layer, see Stansbury et al. (2002) and Bard et al. (2001).

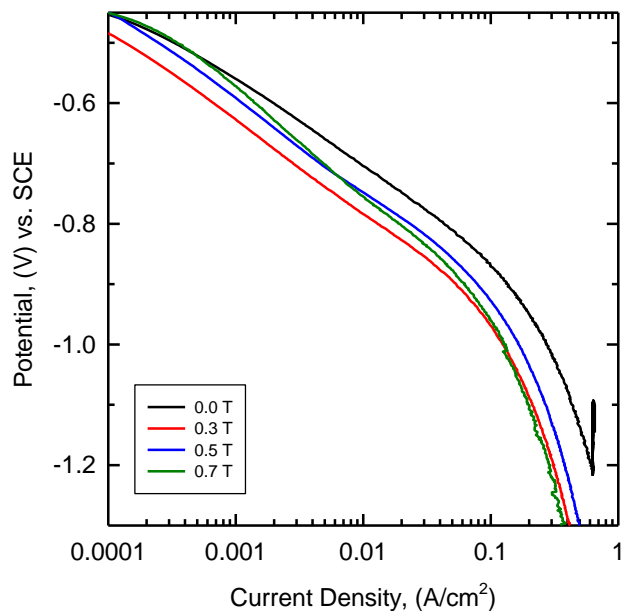


Figure 5.14: Plot of the cathodic branch of the potentiodynamic polarization curve. The limiting current density is shown as decreasing with increasing magnetic field strength. The limiting current density is where the polarization curves intersect the x-axis (current density).

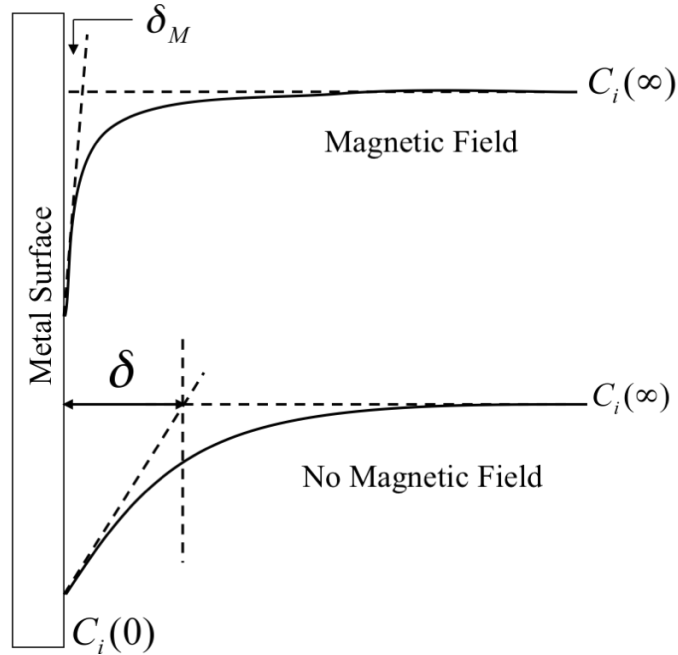


Figure 5.15: Schematic showing how an applied magnetic field can decrease the thickness of the concentration gradient in front of the electrode. The top schematic shows the thickness of the concentration gradient with a magnetic field and the bottom schematic shows the thickness of the concentration gradient without a magnetic field.

The general equation that describes limiting current density is given as

$$i_L = \frac{D n F C}{\delta} \quad (5.11)$$

where D is the diffusion coefficient, n is the number of electrons exchanged, F is Faraday's constant, C is the bulk concentration, and δ is the diffusion layer thickness. The limiting current density can be increased in a number of ways. For example, higher solution concentration, C ; higher temperature, which increases D ; and higher solution agitation, which decreases δ .

At the limiting current density, the concentration of the species being reduced, hydrogen in this case, goes to zero: $C_{H^+}(x=0) = 0$, see the bottom schematic of Figure 5.15. When the magnetic field is applied to the electrochemical system, see the top schematic of Figure 5.15, the thickness of the diffusion layer (δ) decreases. A decrease in the diffusion layer thickness means an increase in the supply of hydrogen ions to the surface of the electrode.

Therefore, in terms of this research, it is believed that the limiting current density would be increased due to magnetoconvective effects (stirring) caused by the Lorentz force. The stirring

created by the Lorentz force would act to decrease the thickness of the diffusion layer, see Figure 5.15, thereby increasing the limiting current density. However, as can be seen from the experimental data provided in Figure 5.14, the limiting current density is seen to decrease with applied magnetic field.

The reason for the discrepancy between theory and experiment could be a result of orientation. There exists a strong orientation dependence on mass transport in a magnetic field, see Tacken et al. (1995) and Mori et al. (2002). The cross product between the current and the magnetic field gives the Lorentz force. Therefore, if the magnetic lines are parallel to the current, the Lorentz force is zero. If the magnetic field lines are perpendicular to the current, the Lorentz force is at its maximum. When the Lorentz is zero, the only forces that contribute to convection are the concentration gradient force and the magnetic field gradient force. The effect of a magnetic field on mass transport, diffusion layer thickness, and limiting current density is analyzed in more detail in Chapter 6.

5.4.3 Magnetic Field Effect on the Passivation Potential

Polarization curves for API X80 linepipe steel were measured at a scan rate of 0.1667 V/s in 1N H₂SO₄ at magnetic field strengths ranging from 0.0 – 0.7 Tesla. The results of these experiments are given above in Figures 5.1 – 5.4. Figure 5.16 below, shows a comparison of polarization experiments performed on API X80 linepipe steel at a magnetic field strength of 0.0 and 0.7 Tesla.

Table 5.1: Current densities and potentials from a polarization experiment performed on API X80 linepipe steel with and without a 0.7 Tesla magnetic field. M stands for magnet.

	i_p (A/cm ²)	$i_{p,M}$ (A/cm ²)	E_{PP} (V)	$E_{PP,M}$ (V)	i_{crit} (A/cm ²)	$i_{crit,M}$ (A/cm ²)
X80	0.0891	0.0013	0.428	1.035	0.0891	0.251

The important points to note from Figure 5.16 are the shifts in the critical parameters that characterize the corrosion and passivation behavior of an alloy. The parameters that characterize the corrosion behavior are i_p , i_{crit} , and E_{PP} . i_{crit} is the critical current density that must be exceeded to initiate the formation of a passive film. E_{PP} is the passivation potential, and i_p is the

passivation current. Table 5.1 gives the value of each parameter with and without a magnetic field.

In all cases, a magnetic field increases the peak current: i_{crit} , increases the passivation potential; E_{pp} , and decreases i_p . The magnitude of the change in current density between i_{crit} and i_p is of great importance since the magnitude of this change indicates the effectiveness of the passive film in reducing the corrosion rate of the anode, Stansbury et al. (2002). Lastly, the presence of a magnetic field in the electrochemical cell decreases the range of potential in which the metal is actually protected from corrosion.

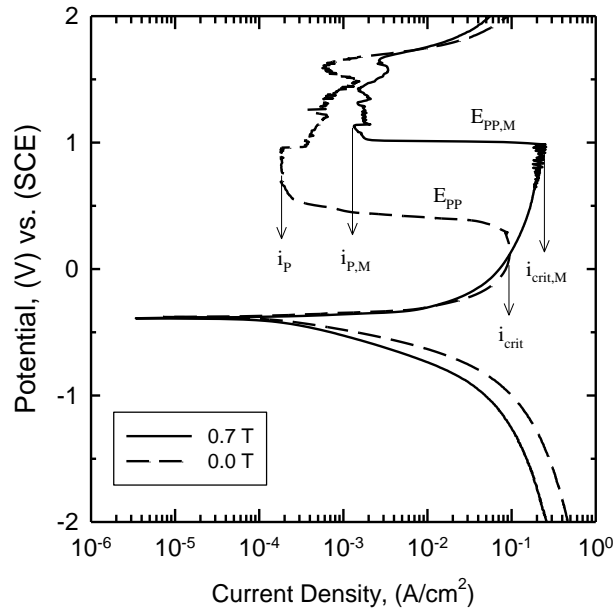


Figure 5.16: Potentiodynamic polarization curves for API X80 linepipe steel with and without a magnetic field. The plot has characteristic potentials and currents labeled, illustrating the difference in corrosion behavior with and without a magnetic field.

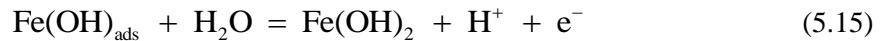
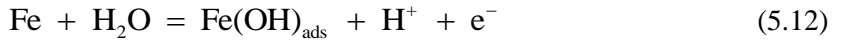
5.4.3.1 Model for Passivation Potential Shift

In this Section, a model or mechanistic explanation is given for the observed increase in passivation potential when a magnetic field is present in the electrochemical cell during a potentiodynamic polarization experiment. The model is based upon convective motion created by the Lorentz force, the concentration gradient force, and the magnetic field gradient force. However, before the model is presented, some words need to be said about the passivation of metals in general.

Metals in the passive state have a thin oxide layer on their surface which separates the metal from the electrolyte, Landolt (2007). The formation of solid corrosion products on the surface of an electrode is a dominant factor in controlling corrosion. These solid corrosion products form when the metal ions going into solution reach a saturation concentration, and precipitate onto the metal surface. If the precipitates do not adsorb to the surface, the corrosion rate will increase due to continual removal of ions from solution. The driving force to compensate for lack of ions in solution is continued transfer of metal ions from the electrode surface into the solution, Stansbury et al. (2002).

Alternatively, precipitates that adsorb to the electrodes surface and form continuous, nonporous films reduce the corrosion rate due to the fact that the controlling mechanism is now solid-state diffusion of ions through the film. Additionally, if the film is a poor conductor of electrons, then the corrosion reaction is further inhibited, Landolt (2007), Stansbury et al. (2002), and Jones (1996).

The generally accepted mechanism for the anodic dissolution of iron in acidic solution is given below

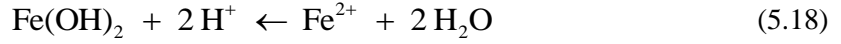


as proposed by Bockris et al. (1970), Lorbeer et al. (1978), and Lu et al. (2003). The reaction steps show the metal passivating with the formation of Fe(OH)_2 . Equations (5.12) – (5.17) and Figure 5.17 will be used to explain the observed shift in the passivation potential with applied magnetic field.

Consider the schematic of the metal/ electrolyte interface given in Figure 5.17. Figure 5.17 shows a schematic diagram of an electrode surface undergoing anodic dissolution in an acidic electrolyte. δ in Figure 5.17 represents the thickness of the diffusion layer, and the series of lines next to the electrode surface represent the passivating film that has grown.

Figure 5.17(a) gives the situation that occurs next to the electrode surface during a potentiodynamic polarization experiment when $B = 0$. There exists a high concentration of iron

ions in solution next to the electrode, and the electrode is in a passive state – covered by Fe(OH)_2 . From a thermodynamic perspective, considering Equation (5.16), the reaction is being driven towards the formation Fe(OH)_2



due to the high concentration of iron ions. Therefore, the relatively high concentration of iron ions and the relatively low concentration of hydrogen ions, and the absence of any convective motion, results in the normal potentiodynamic polarization curve given by the dashed line in Figure 5.16.

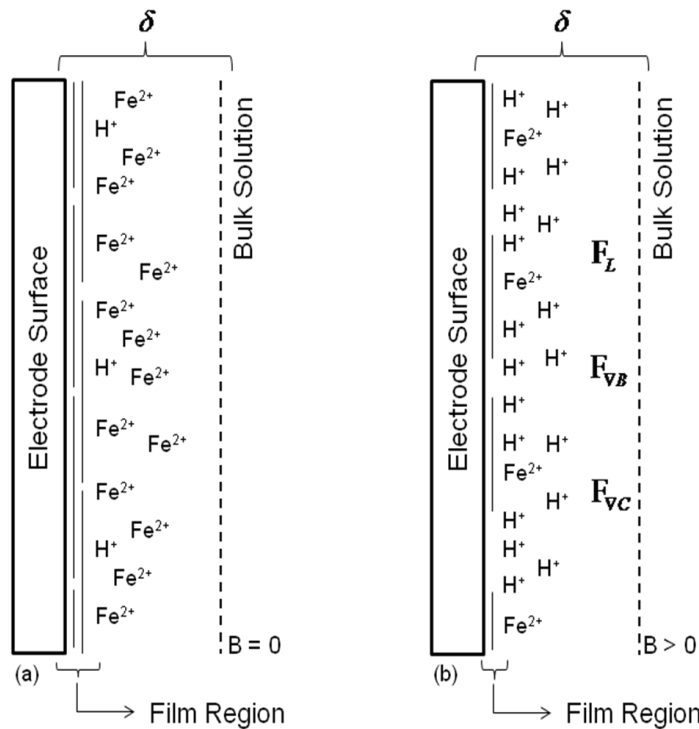
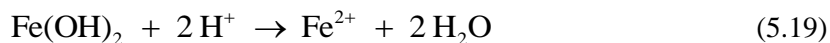


Figure 5.17: Schematic showing the anodic dissolution of iron; (a) without an applied magnetic field, and (b) with an applied magnetic field.

Figure 5.17(b) gives the situation that occurs next to the electrode surface during a potentiodynamic polarization experiment when $B > 0$. There exists a high concentration of hydrogen ions next to the electrode surface, locally making the solution more acidic, and delaying the onset of passivation. From a thermodynamic perspective, considering Equation (5.16), the reaction is being driven towards the dissolution of Fe and subsequently Fe(OH)_2



due to the high concentration of hydrogen ions. The reason for the change in passivation behavior of API X80 linepipe steel is the presence of magneto-convective motion in the electrolyte.

The magneto-convective motion is created by the forces shown in the diffusion layer next to the electrode, Figure 5.17(b). The three forces are: Lorentz force, concentration gradient force, and magnetic field gradient force. The concentration gradient force is directed towards areas with higher concentrations of paramagnetic species and the magnetic field gradient force is directed toward areas with higher values of magnetic field strength, Lioubashevski et al. (2007, 2004), Leventis et al. (2001, 1999, 2005), Devos et al. (2000), Bund et al. (2005), Ragsdale et al. (1998, 1996), and Grant et al. (2001). Given that the Lorentz force is the cross-product between the magnetic field strength and the current, the regions where the Lorentz force serves as the dominant mode of magneto-convection can be tracked, Figure 5.18.

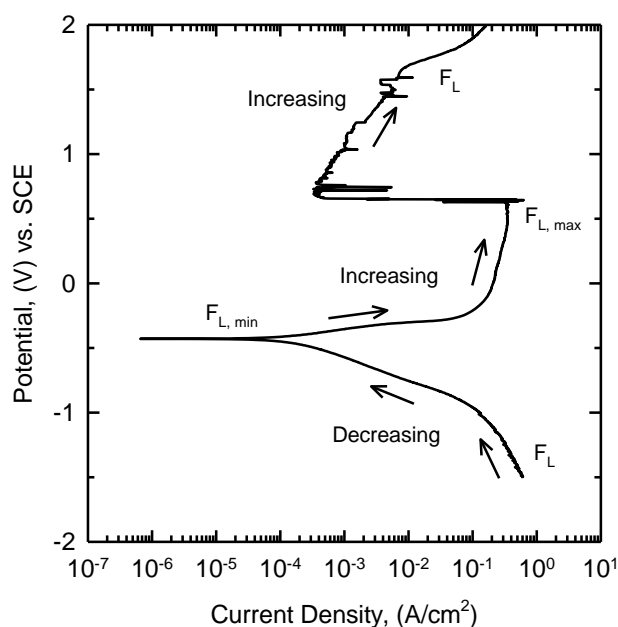


Figure 5.18: Potentiodynamic polarization curve for API X80 at a magnetic field strength of 0.7 Tesla. F_L represents the Lorentz force and this schematic shows regions on the polarization curve where the Lorentz force is dominant. On the anodic branch, the Lorentz force is greatest at the passivation potential.

Considering the anodic branch of the polarization curve shown in Figure 5.18, it can be seen that the Lorentz force reaches its maximum value at the onset of passivation. The passivation potential is shifted to more positive values because the magnetic forces enhance mass transport

and eliminate concentration gradients. It can be seen in Figure 5.19 that the passivation potential increases with increasing magnetic field strength. Mass transport enhancement due to the Lorentz force will be analyzed in more detail in Chapter 6.

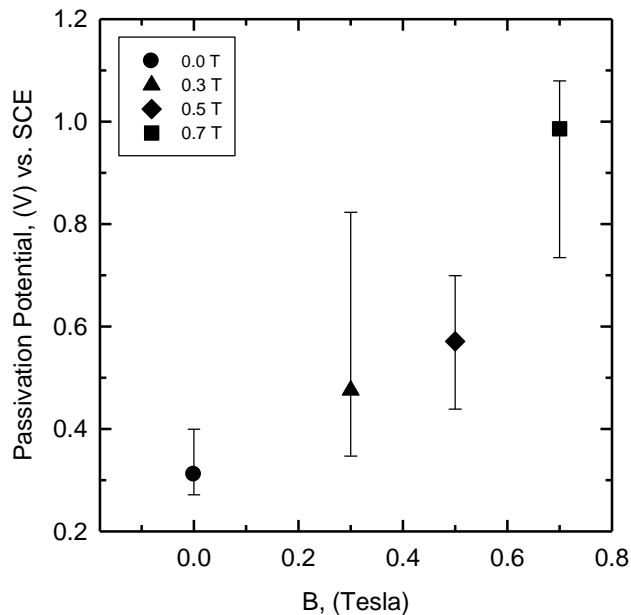


Figure 5.19: Variation in passivation potential as a function of magnetic field strength for API X80 linepipe steel in 1 N H_2SO_4 .

5.5 Discussion: Electrochemical Impedance Spectroscopy Experiments

In this Section the results from the electrochemical impedance spectroscopy experiments will be discussed. The equivalent circuit model that was used to model the impedance spectra will be presented and discussed. The equivalent circuit used in this modeling work is similar to the classical Randles type circuit; however, instead of using a capacitor to represent the double layer capacitance a constant phase element (CPE) is used. The use of a CPE results in an effective double layer capacitance and is used to account for time constant dispersion or frequency dispersion.

5.5.1 Review of Electrochemical Impedance Spectroscopy

In this Section a brief review of electrochemical impedance spectroscopy will be given. Specifically, details pertaining to equivalent circuit modeling and the use of a constant phase elements in the modeling of corroding interfaces will be presented.

There are two approaches to modeling and characterization of electrochemical interfaces: equivalent circuit approach, and the continuum approach. The equivalent circuit approach is the least detailed level of modeling, but the best understood in terms of linear systems and transfer function analysis. The continuum approach is the more detailed level of modeling. Transport of species to the electrode/electrolyte interface is governed by differential equations. Charge transfer processes occurring across the electrode/electrolyte interface is governed by rate laws which serve as boundary conditions to the differential equations, Taylor et al. (2005). The equivalent circuit approach was used in this research.

System linearity is of critical importance when modeling electrochemical interfaces using equivalent circuits. If the system under investigation is not linear, transfer function analysis cannot be used to analyze the system. A transfer function is the transfer gain from $U(s)$ to $Y(s)$ – input to output – of the system, Franklin et al. (2009). It is the ratio of the Laplace transform of the output to the Laplace transform of the input

$$\frac{Y(s)}{U(s)} = H(s) \quad (5.20)$$

where $s = j\omega$. Using a block diagram, the system given by Equation (5.20) is shown below in Figure 5.20.

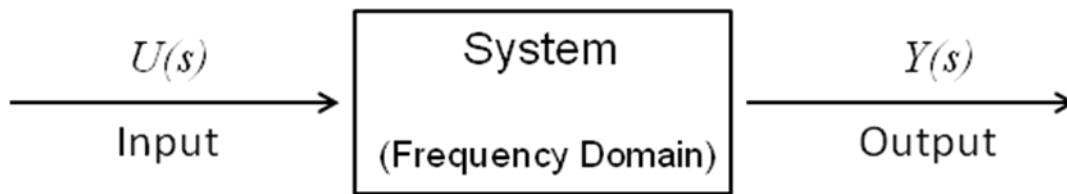


Figure 5.20: Block diagram for a hypothetical linear system. The ratio of the Laplace transform of the output to the Laplace transform of the input is the transfer function of the system.

Therefore, for the special case where the output signal is the system voltage (in the frequency domain) and the measured input signal is the current (in the frequency domain), and

the system is linear, the transfer function is the impedance, Taylor et al. (2005), as shown by the equations below

$$H(j \omega) = \frac{\text{output}}{\text{input}} \quad (5.21)$$

$$H(j \omega) = \frac{V(j \omega)}{I(j \omega)} \quad (5.22)$$

$$H(j \omega) = Z(j \omega) = \text{Impedance} \quad (5.23)$$

Electrochemical systems are rarely linear and the linearity of an electrochemical system is controlled by the potential, Orazem et al. (2008) and Barsoukov et al (2005).

For an EIS experiment a small perturbation potential is applied to the system, and the current response is recorded. The optimal perturbation potential depends on the polarization curve for the system under investigation. The use of a small amplitude perturbation permits application of a linear model for interpretation of the impedance spectra. The appropriate amplitude represents a compromise between the need to minimize nonlinear response (small perturbing amplitude) and the need to minimize noise in the impedance response (large perturbing amplitude). For electrochemical systems with a linear current-voltage curve, large perturbing amplitudes can be used. For electrochemical systems with a nonlinear current-voltage curve, smaller perturbing amplitudes should be employed, Orazem et al. (2008).

Shown below in Figure 5.21 is the circuit used to model the impedance spectra of the electrochemical system analyzed in this research. R_{Ω} is the solution resistance, R_{ct} is the charge transfer resistance, and a CPE. The letters CPE stand for Constant-Phase-Element and represent a circuit element that has a phase angle which is independent of frequency, Barsoukov (2005).

The impedance response of an electrode surface rarely shows ideal behavior. The impedance response usually exhibits a distribution of reactivity that is typically represented as a constant phase element. Time constant dispersion can be due to variations in reactivity, current, or potential along the electrode surface. The presence of time-constant dispersion is usually modeled by the use of a constant phase element, Orazem et al. (2008). The impedance expression of a CPE is given by

$$Z_{\text{CPE}}(\omega) = \frac{1}{Y_0 (i\omega)^\alpha} \quad (5.24)$$

where Y_0 is a factor which is directly proportional to the double layer capacitance C_{dl} of an ideally polarized interface, and the constant α varies between 0 and 1 and is related to the

dispersive nature of the interface. The details of how to obtain α will be discussed in the section on equivalent circuit modeling.

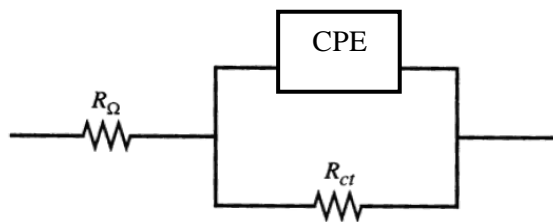


Figure 5.21: Circuit used to model the impedance behavior of the electrode/electrolyte interface. The letters CPE represent a constant phase element.

5.5.2 Interpretation of Impedance Spectra

Since the set of impedance data given in Figures 5.8 – 5.10 exhibit the same behavior only Figure 5.22 will be used to discuss the information that can be obtained from an impedance spectrum. Figure 5.22 is the same as Figure 5.10; the figure is reproduced here for reference. It should be noted that all of the EIS experiments performed for this research exhibit the same behavior and the data presented in Figures 5.8 – 5.11 is a representative sample of the impedance spectra recorded.

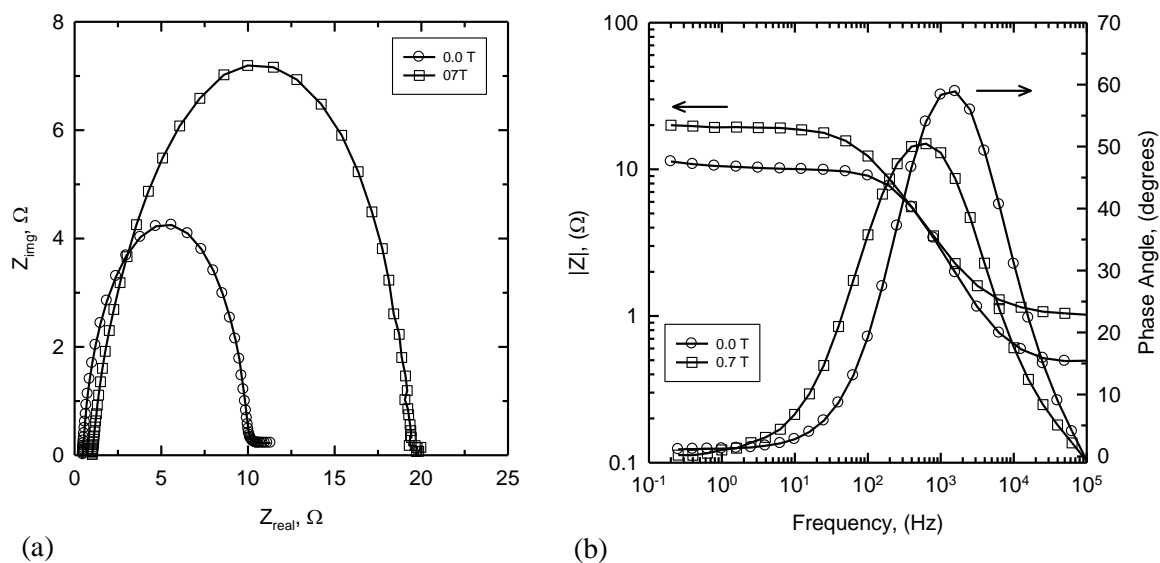


Figure 5.22: Results from the electrochemical impedance spectroscopy experiments; (a) Nyquist plots, (b) Phase angle and Impedance magnitude. (a) Comparison of the Nyquist plots at 0.0 and 0.7 Tesla, the single capacitive loop is indicative of a charge transfer process occurring on the surface of the electrode.

The following comments are about electrochemical impedance spectra in general. Figure 5.22 will be used as a visual aid and reference to describe the important features of EIS spectra. Figure 5.22 will be referred to again later as a means of explaining the experimentally observed behavior of the electrochemical system under study.

Figure 5.22(a) is known as the Nyquist plot. This plot gives the imaginary impedance, Z_{img} , as a function of the real impedance, Z_{real} – impedance is an imaginary quantity. There is no explicit representation of frequency on a Nyquist plot; however, the symbols on the impedance loops given in Figure 20(a) denote discrete points of frequency. For an EIS experiment, the frequency is swept from 1×10^5 to 1×10^{-1} Hz. Larger frequency ranges can be used, but for this research the frequency was swept from 1×10^5 to 1×10^{-1} Hz.

High frequency points are located near the origin and the frequency decreases along the Z_{real} axis. At the high frequency end of the impedance loop, where the loop intersects the x-axis near the origin, the value of the solution resistance is given. At the low frequency end of the impedance loop, where the loop intersects the x-axis at higher values of real impedance, the sum of solution resistance and charge transfer resistance is given. Lastly, for an ideal system (no time constant dispersion), the double layer capacitance can be obtained by the following relationship

$$C_{dl} = \frac{1}{\omega_{max} R_{ct}} \quad (2.25)$$

where C_{dl} represents the double layer capacitance, ω_{max} is the frequency at the apex of the impedance loop, and R_{ct} is the charge transfer resistance.

Figure 5.22(b) is known as the Bode diagram. There are two different data sets presented in Figure 5.22(b): the left axis is the impedance magnitude, and the right axis is the phase angle. The Bode diagrams show the functionality with respect to frequency much more clearly. The frequency is usually presented on a logarithmic scale to reveal important low frequency behavior, Orazem et al. (2008). Considering the plot of magnitude of impedance as a function of frequency; it can be used extract the same information that was obtained from the Nyquist plot. At high frequencies, the value of the solution resistance is given. At low frequencies, the summation of the solution resistance and the charge transfer resistance is given.

The phase angle as a function of frequency plot gives the phase angle between the voltage and current. The phase angle, θ , between voltage and current can be written as

$$\theta = \arctan\left(\frac{Z_{img}}{Z_{real}}\right) \quad (5.26)$$

this relationship is derived from the fact that voltage and current are phasor quantities, Taylor et al. (2005). The phase angle plots are sensitive to system parameters and provide a good means of comparing model to experiment. The impedance magnitude is less sensitive to system parameters but provides values for the solution resistance (high frequency) and charge transfer resistance (low frequency), Orazem et al. (2008).

5.5.3 Equivalent Circuit Modeling of the Experimental EIS Spectra

In this Section the experimental and modeling results for the electrochemical impedance experiments will be discussed. As was stated above, the interface was modeled using the circuit given in Figure 5.21. The method for determining the unknown parameters in Equation (5.24) will be presented and discussed as well.

Figure 5.22 shows the Nyquist plot and the bode plot for API X80 linepipe steel at a magnetic field strength of 0.7 Tesla (square symbols) and 0.0 Tesla (open circles). The Nyquist plots, Figure 5.22(a), show a single capacitive loop. A single capacitive loop is indicative of

charge transfer process occurring on the surface of the electrode. The charge transfer process that is taking place on the electrode surface is the hydrogen reduction reaction



charge transfer resistance is associated with the separation of charge at the electrode interface, Stansbury et al. (2004). The charge transfer resistance increases with increasing magnetic field strength as can be seen in Figure 5.22(a) and also in Figure 5.23. Figure 5.23 shows the behavior of charge transfer resistance with increasing magnetic field strength.

Figure 5.22(b) gives the Bode plot of API X80 linepipe steel at a magnetic field strength of 0.7 Tesla (square symbols) and 0.0 Tesla (open circles). It was mentioned above that the magnitude of impedance plot can be used to obtain the same information that is given in the Nyquist plot. Comparing Figure 5.11 and Figure 5.25 it can readily be seen that solution resistance (high frequency) and charge transfer resistance (low frequency) increases with increasing magnetic field strength.

Due to the sensitivity in the phase angle measurements, a great deal of qualitative information can be extracted from this data. Figure 5.24 compares the phase angle plots for the four different magnetic field strengths. Shifts in the phase angle data can be attributed to changes in the system parameters: solution resistance, charge transfer resistance, and double layer capacitance. Increasing the value of solution resistance acts to depress the overall height of the phase angle peak; this effect can be seen as the magnetic field strength is increased from 0.0 to 0.7 Tesla.

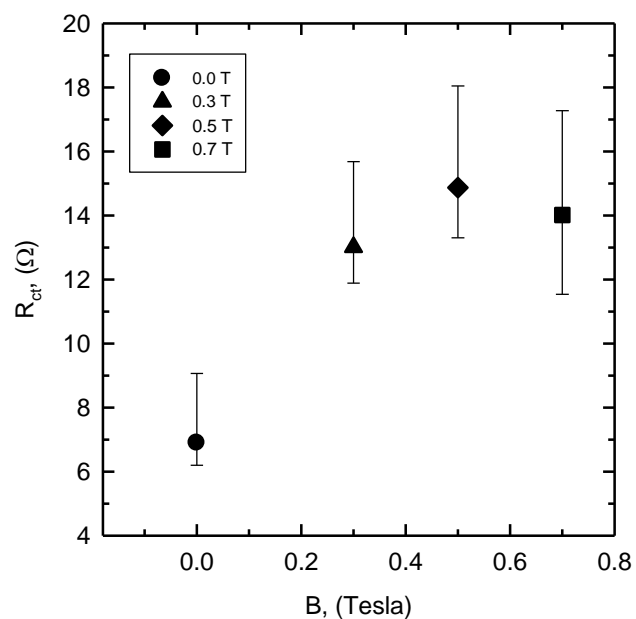


Figure 5.23: Variation in charge transfer resistance as a function of magnetic field strength for API X80 linepipe steel in 1 N H₂SO₄.

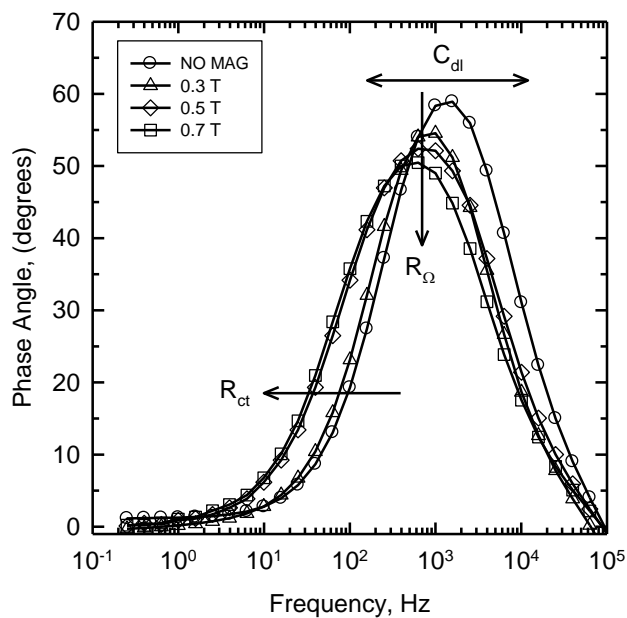


Figure 5.24: Comparison of the phase angle plots at the four different magnetic field strengths for API X80 linepipe steel in 1 N H₂SO₄. The arrows show the effect of changing the system parameters: R_{ct} , R_{Ω} , C_{dl} .

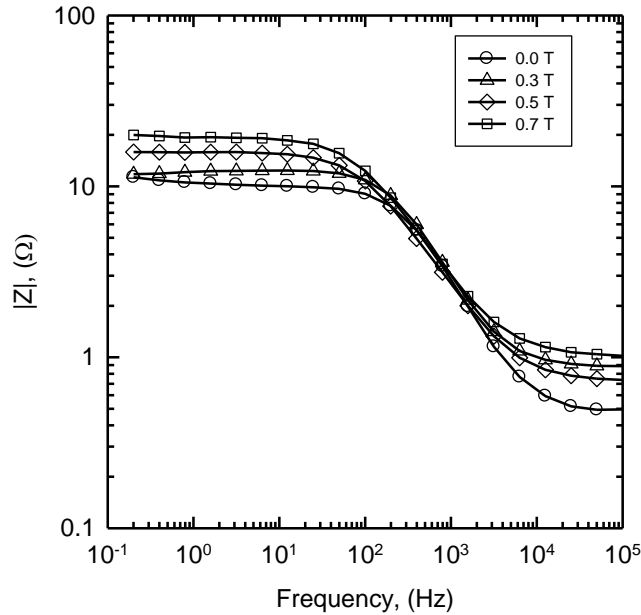


Figure 5.25: Comparison of the impedance magnitude plots at the four different magnetic field strengths for API X80 linepipe steel in 1 N H₂SO₄.

Changes in charge transfer resistance can be seen most readily at the low frequencies; just as in the Nyquist plot. Changes in the double layer capacitance will shift the phase angle plot back and forth along the frequency axis. The shifts shown in the phase angle data of Figure 5.24 can be attributed to changes in charge transfer resistance and double layer capacitance since the changes in solution resistance are minor; see Figure 5.11 (high frequency).

The EIS results were modeled using the equivalent circuit given in Figure 5.21. The impedance of a constant phase element is given by Equation (5.24). The double layer capacitance can be calculated from the following relationship

$$C_{dl} = Y_0(\omega_{max})^{(\alpha-1)} \quad (5.28)$$

The objective of modeling the impedance spectra of the system is to determine two main parameters: charge transfer resistance, and double layer capacitance. The charge transfer resistance can be related to the exchange current density, i_0 , by the following equation

$$R_{ct} = \frac{R T}{F i_0} \quad (5.29)$$

where R is the gas constant, T is the temperature, and F is Faraday's constant.

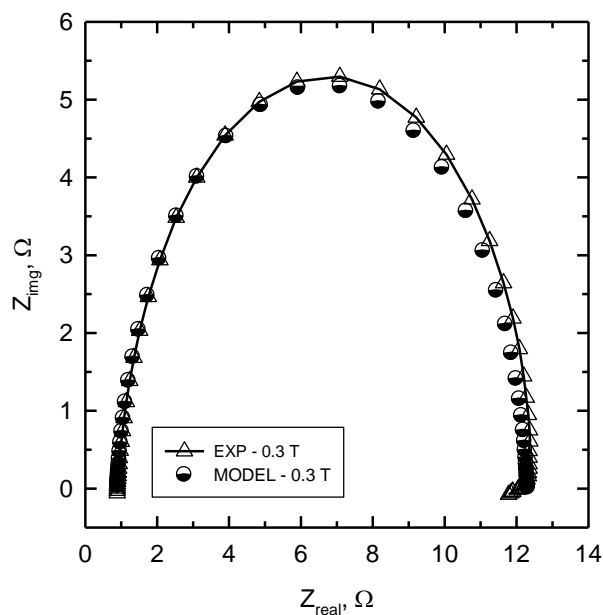


Figure 5.26: Nyquist plot comparing experimental data (triangles) and model data (black/white circles) using the equivalent circuit given in Figure 5.21. This data is for API X80 linepipe steel in 1 N H_2SO_4 .

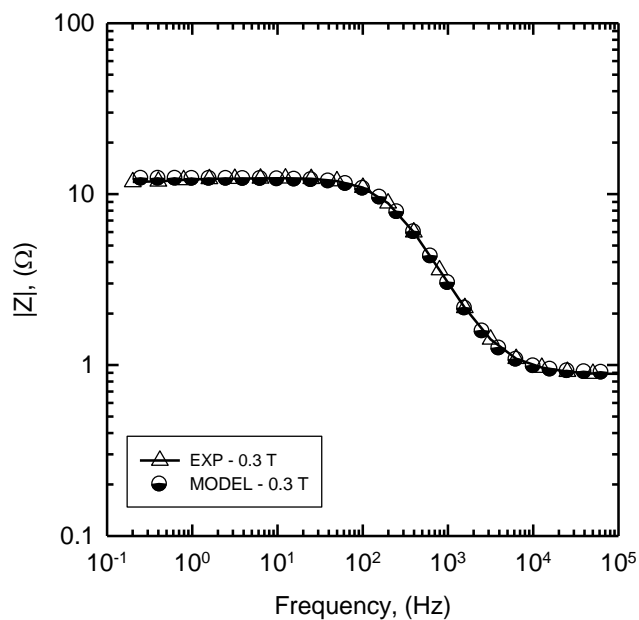


Figure 5.27: Impedance magnitude plot comparing experimental data (triangles) and model data (black/white circles) using the equivalent circuit given in Figure 5.21. This data is for API X80 linepipe steel in 1 N H_2SO_4 .

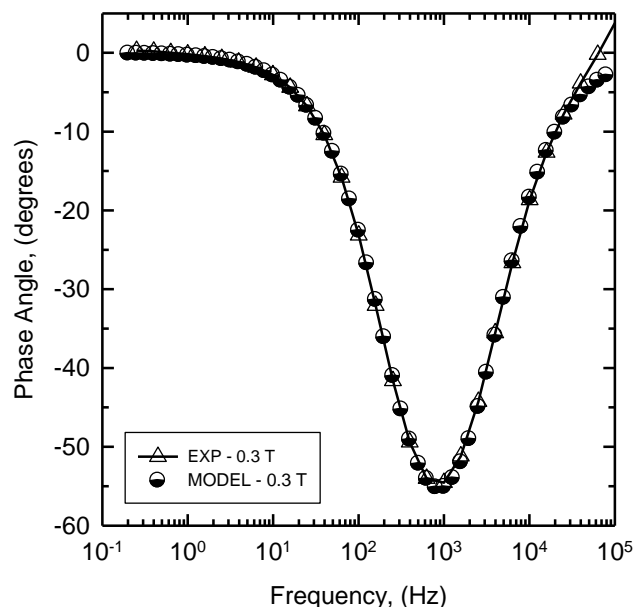


Figure 5.28: Phase angle plot comparing experimental data (triangles) and model data (black/white circles) using the equivalent circuit given in Figure 5.21. This data is for API X80 linepipe steel in 1 N H_2SO_4 .

The exchange current is a measure of the kinetics of the reaction at equilibrium and is an important kinetic parameter for use in the study of corrosion, Stansbury et al. (2004). The double layer capacitance is associated with adsorption processes occurring on the electrode surface, Sathiyarayanan et al. (2006), Orazem et al. (2008).

Figures 5.26 – 5.28 give a comparison of experimental data with model data at a magnetic field strength of 0.3 Tesla. Figure 5.26 gives a comparison of the experimental data and model data for the Nyquist plots. The model data underestimates the experimental data at the low frequency end of the spectrum. This is due to the asymmetry in the experimental impedance data at about twelve ohms. This type of behavior can be mistaken for an inductive response, but is likely due to an increasing corrosion rate. Figure 5.27 compares the experimental and model data of the impedance magnitude. Figure 5.28 shows the phase angle experimental and model data. The model data shows good agreement to the experimental data in Figure 5.28; this is good since the phase angle is most sensitive to changes in system parameters this sensitivity is useful when comparing model to experiment. The data was fit to the equivalent circuit in Figure 5.21 by complex nonlinear regression using a Levenberg-Marquardt method. This was done using the Gamry Echem Analyst software.

To determine the two unknown constants in Equation (5.28) further analysis of the impedance data needs to be done. It is difficult to know *a priori* if the experimental impedance data exhibits CPE behavior. Therefore, before fitting the experimental impedance data to an equivalent circuit with a CPE, the data should be analyzed to check for CPE behavior. The CPE behavior can be quantified and the numerical value of α can be obtained by plotting the impedance as shown in Figure 5.29.

Figure 5.29 shows the imaginary impedance as a function of frequency on a logarithmic scale. The imaginary part of the impedance is independent of solution resistance; therefore no correction for ohmic resistance is necessary, Jorcin et al. (2006). Notice that all of the data plotted in Figure 5.29 converges to a high frequency asymptote. The value of α is obtained from the slope of the high frequency asymptote for each magnetic field strength condition. Performing a linear regression of the high frequency impedance data gives the numerical value of α , see Figures 5.30 and 5.31. The results from this are given in Figure 5.32, which shows a plot of double layer capacitance as a function of magnetic field strength. The expected outcome of this analysis was to show decreasing double layer capacitance with increasing magnetic field strength. This result was expected due to the face that double layer capacitance is inversely proportional to charge transfer resistance, see Equation (5.22). Additional modeling results are shown in Table 5.2.

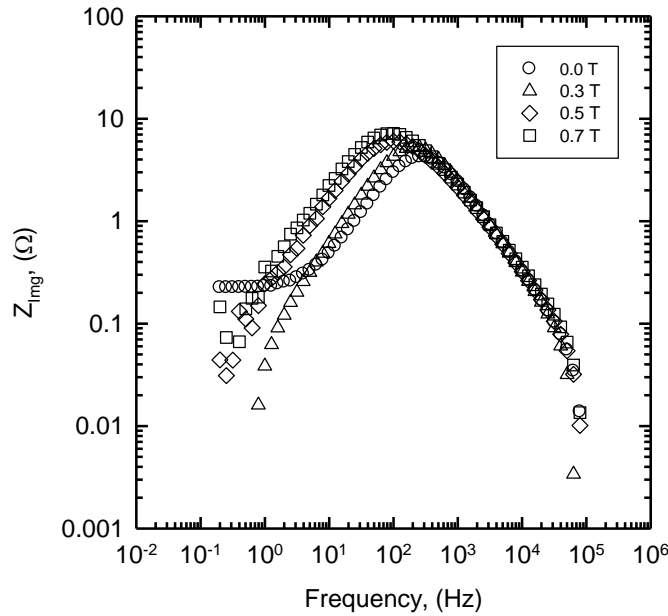


Figure 5.29: Plot of the imaginary impedance as a function of frequency. The high frequency impedance data converge to approximately the same slope, the slope gives the value of α .

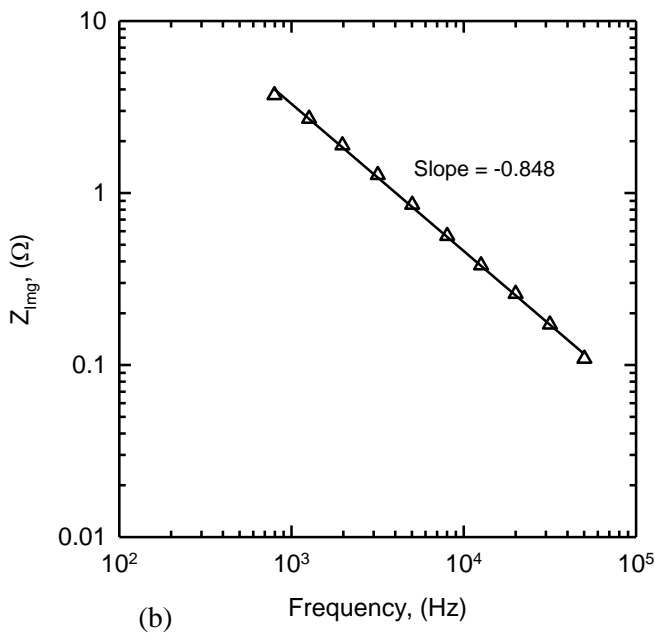
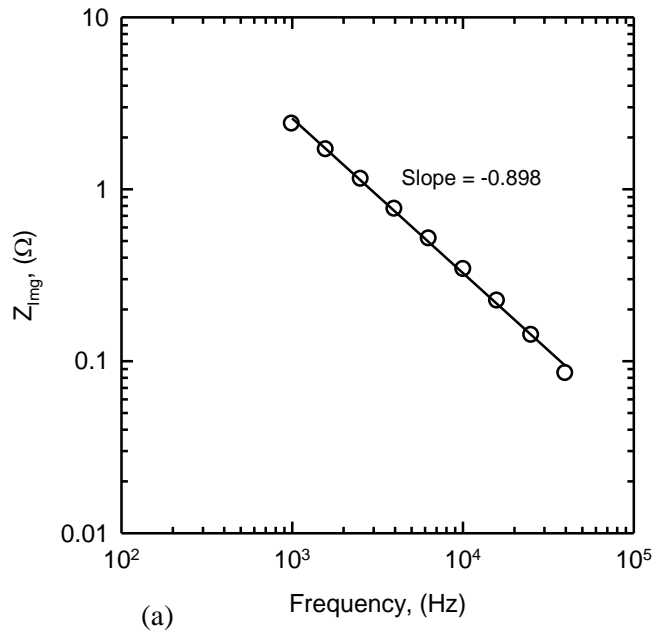


Figure 5.30: Linear regression analysis of the high frequency impedance data for API X80 linepipe steel at magnetic field strengths of: (a) 0.0 Tesla, and (b) 0.3 Tesla.

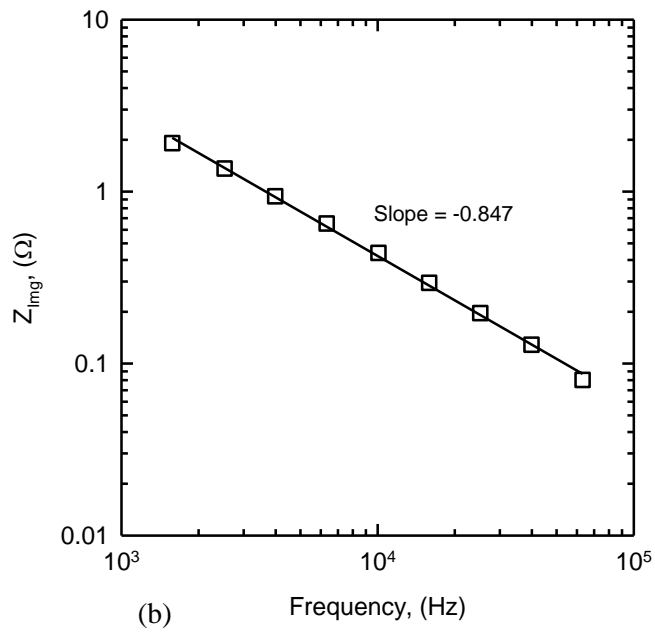
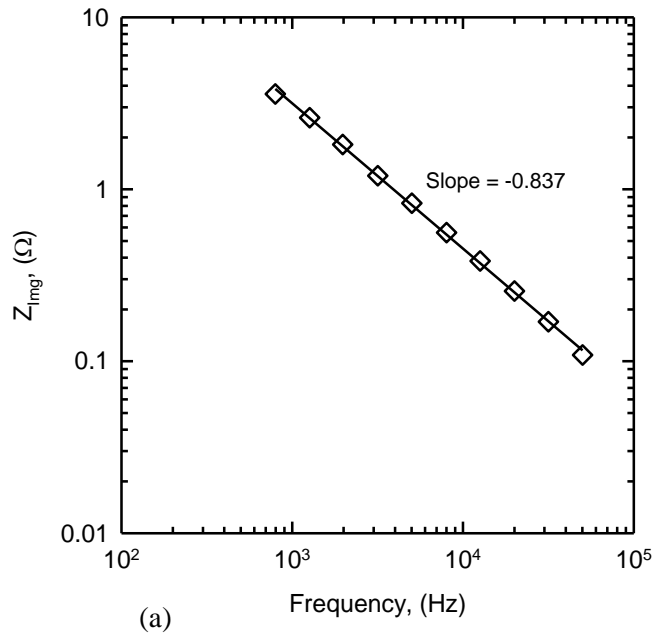


Figure 5.31: Linear regression analysis of the high frequency impedance data for API X80 linepipe steel at magnetic field strengths of: (a) 0.5 Tesla, and (b) 0.7 Tesla.

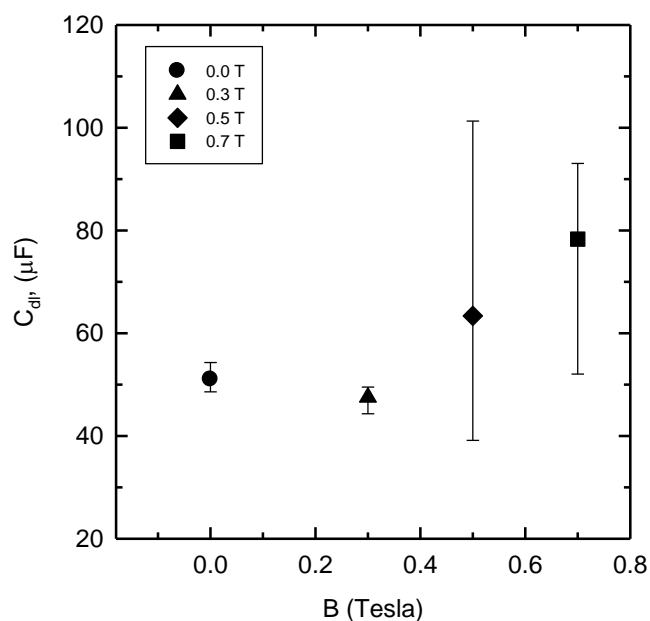


Figure 5.32: Variation in double layer capacitance as a function of magnetic field strength for API X80 linepipe steel in 1 N H₂SO₄.

The data presented in Figure 5.32 and Table 5.2 show a slightly decreasing double layer capacitance at low magnetic field strengths and slightly increasing double layer capacitance at higher magnetic field strengths. The scatter in the data at higher magnetic field strengths makes it difficult to interpret exactly what is occurring at the metal/electrolyte interface.

The variability in the double layer capacitance data at higher magnetic field strengths is due to the fact that the equivalent circuit model tends to underestimate or overestimate the charge transfer resistance. The model would underestimate the charge transfer resistance if there was an asymmetry at the low frequency end. The model would overestimate the charge transfer resistance if there was a low frequency ‘tail’. An asymmetry in impedance data indicates an increasing corrosion rate as the experiment proceeds. The asymmetry usually occurs at low frequency when the impedance response is dominated by R_{ct} , Cottis et al (1999). A low frequency tail is detected when the corrosion rate is decreasing during the experiment. The total impedance increases which is due to an increasing R_{ct} as the experiment proceeds. These two phenomena are shown in Figures 5.33 and 5.34.

From experimental results, however, there is a decrease in double layer capacitance with increasing magnetic field. This conclusion is based upon the results from the Nyquist plots given in Figure 5.11 and Equation (5.25).

Table 5.2: Equivalent circuit modeling results for API X80 linepipe steel in 1 N H₂SO₄

B, (T)	R _{ct} , (Ω)	R _Ω , (Ω)	Y ₀ , (μ Ω ⁻¹ s ^α)	α, (-)
0.0	9.825	0.486	109.2	0.924
	9.066	0.524	109.8	0.922
	6.839	0.549	114.2	0.919
	6.946	0.666	136.0	0.904
	6.445	0.612	132.8	0.911
0.3	11.41	0.896	98.09	0.939
	12.95	0.891	98.18	0.932
	12.59	0.879	96.47	0.931
	17.05	1.07	123	0.880
	14.13	1.101	131.4	0.874
0.5	15.26	0.728	261	0.842
	14.46	0.724	264.1	0.844
	14.44	0.751	260.3	0.640
	12.78	1.091	160.1	0.872
	18.93	1.130	124.5	0.870
0.7	18.63	1.020	256.4	0.863
	15.75	1.021	289.0	0.826
	16.16	1.028	286.7	0.829
	11.38	1.286	149.3	0.858
	12.24	1.195	150.5	0.864

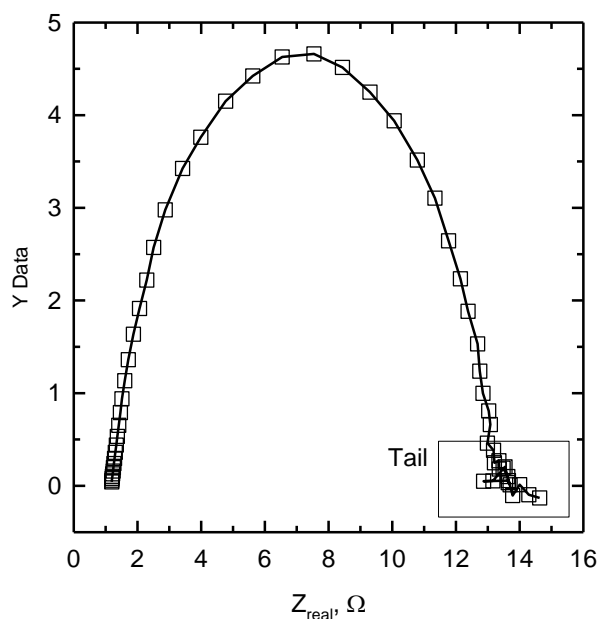


Figure 5.33: Nyquist plot of API X80 linepipe steel at a magnetic field strength of 0.7 Tesla in 1 N H₂SO₄. The low frequency tail is shown in the box labeled ‘Tail’. This behavior is due to a decreasing corrosion rate as the experiment progresses.

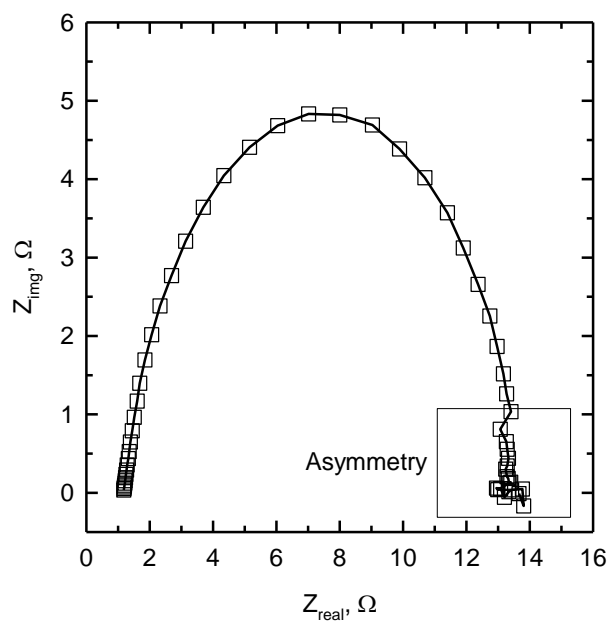


Figure 5.34: Nyquist plot of API X80 linepipe steel at a magnetic field strength of 0.7 Tesla in 1 N H₂SO₄. The low frequency asymmetry is shown in the box labeled ‘Asymmetry’. This behavior is due to an increasing corrosion rate as the experiment progresses. This behavior is evident at lower magnetic field strengths as well; see Figure 8(a).

5.6 Summary and Concluding Remarks

In this chapter it was shown that when a magnetic field is applied to an electrochemical system certain electrochemical processes are altered. From the potentiodynamic polarization experiments, it was shown that a magnetic field acts to increase the passivation potential, shift the corrosion potential (OCP), and decrease the limiting current density.

The shift in passivation potential was attributed to magneto-convection. The three forces responsible for magneto-convection are the Lorentz force, concentration gradient force, and the magnetic field gradient force. The most dominant of these three forces is the Lorentz force. The Lorentz force is directly proportional to the current density and therefore regions where the Lorentz force is dominant may be tracked along the potentiodynamic polarization curve. It was shown that the Lorentz force was strongest at the onset of passivation, or in terms of current density, the Lorentz force was strongest at i_{crit} . Elimination of concentration gradients, due to magneto-convection, results in a shift in the passivation potential.

A thermodynamic model was developed to account for the shift in open circuit potential. To account for the open circuit potential shift, a magnetic work term was added to the classical form of the Nernst equation. Lastly, the decrease in limiting current density with increasing magnetic field strength is not well understood since this result is counterintuitive to what is expected. Increasing solution agitation (stirring) should decrease the diffusion layer thickness which would result in increased limiting current density. In Chapter 6 it is proven mathematically that a magnetic field increases the limiting current density.

The data obtained from the electrochemical impedance spectroscopy experiments show three important results: (1) increase in charge transfer resistance with increasing magnetic field, (2) decrease in double layer capacitance, and (3) cathodic film formation. Increase in charge transfer resistance and decrease in double layer capacitance are both evidence of cathodic film formation. It is believed that cathodic film formation is responsible for the erratic hydrogen results given in Chapter 4.

CHAPTER 6

RESULTS AND DISCUSSION: MAGNETOHYDRODYNAMIC FLUID FLOW MODEL

6.1 Introduction

In this chapter, three fluid flow models will be presented. The models are based upon the boundary layer equations for magnetohydrodynamics. The first model accounts for a nonuniform magnetic field. The second model accounts for coupled fluid flow and mass transport in the boundary layer region of a vertical electrode. In the second model, the magnetic field is assumed constant. The purpose of the first model is two-fold: (1) present and discuss the effects of a magnetic field on the boundary layer structure and velocity profiles, and (2) introduce and discuss some of the finer points of the modeling technique used to solve the transport equation. The purpose of the third model is to derive relationships for the boundary layer thickness and transport correlations which take into account the magnetic field. These relationships are derived by the use of scaling analysis.

6.2 Mathematical Formulation for a Nonuniform Magnetic Field

The purpose of solving the system of equations given by Equations (6.1) and (6.2) is to discuss the effect of a magnetic field on fluid flow and to introduce the Adomian Decomposition Method (ADM). ADM is an analytical technique which can be used to solve many different types of equations (linear, nonlinear, partial differential equations). The ADM method will also be used later in this chapter to solve a fully coupled system of nonlinear differential equations which governs fluid flow and mass transport at a vertical electrode with a magnetic field applied parallel to the electrode surface.

Equations (6.1) – (6.6) are the boundary layer equations which govern the magnetohydrodynamic fluid flow of an electrically conducting fluid in the presence of a nonlinearly varying magnetic field over a flat plate, Gebhart et al. (1988). Equations (6.5) – (6.7) are the similarity variables. Equations (6.10) – (6.12) are the third order nonlinear differential

equation deduced by substituting the similarity variables into Equations (6.1) – (6.2). The governing equation for this model are given below

$$\frac{\partial u}{\partial x} + \frac{\partial v}{\partial y} = 0 \quad (6.1)$$

$$u \frac{\partial u}{\partial x} + v \frac{\partial v}{\partial y} = \nu \frac{\partial^2 u}{\partial y^2} - \frac{\sigma B^2(x)}{\rho} u \quad (6.2)$$

where u and v are the velocity components in the x and y directions, ν is the kinematic viscosity, ρ is the density and σ is the electrical conductivity of the solution. In Equation (6.2), the external electric field and polarization effects are considered negligible. Lastly, the induced magnetic field has been neglected. The magnetic field is given by the following equation

$$B(x) = B_0 x^{(n-1)/2} \quad (6.3)$$

The boundary conditions to this system of equations are given as

$$u(x, 0) = c x^n \quad (6.4)$$

$$v(x, 0) = 0 \quad (6.5)$$

$$u(x, y) \rightarrow 0 \text{ as } y \rightarrow \infty \quad (6.6)$$

using the following similarity variables

$$\eta = \sqrt{\frac{c(n+1)}{2\nu}} x^{(n-1)/2} y \quad (6.7)$$

$$u = c x^n f'(\eta) \quad (6.8)$$

and

$$v = -\sqrt{\frac{c\nu(n+1)}{2}} x^{(n-1)/2} \left[f(\eta) + \frac{n-1}{n+1} \eta f'(\eta) \right] \quad (6.9)$$

and substituting them into Equations (6.1)-(6.2), gives a system of nonlinear ordinary differential equations

$$f''' + f f'' - \beta f'^2 - M f' = 0 \quad (6.10)$$

with boundary conditions given as

$$f(0) = 0, \quad f'(0) = 1, \quad f'(\infty) = 0 \quad (6.11)$$

where

$$\beta = \frac{2n}{1+n}, \quad M = \frac{2\sigma B_0^2}{\rho c(1+n)} \quad (6.12)$$

This problem was chosen due to the fact that no similarity solution exists for a uniform magnetic field, (Gebhart et al. 1988), and there exists an exact solution for the special case when $\beta = 1$. The existence of an exact solution to Equation (6.10) allows for a comparison to be made between the analytical solution and the exact solution. The exact solution to Equation (6.10) is given by

$$f(\eta) = \frac{1 - \exp(-\sqrt{1+M} \eta)}{\sqrt{1+M}} \quad (6.13)$$

6.2.1 Solution by Adomian Decomposition Method (ADM)

The ADM technique is based upon decomposing the unknown function of any equation into the sum of an infinite number of components, (Wazwaz, 2002).

Rewriting Equation (6.10) in the following form

$$L f = -A_n + \beta B_n + M f' \quad (6.14)$$

where L is a linear operator and A_n and B_n are nonlinear operators. L is given by

$$L = \frac{d^3}{d\eta^3} \quad (6.15)$$

with the inverse of L is given by

$$L^{-1} = \int_0^\eta \int_0^\eta \int_0^\eta (\cdot) d\eta d\eta d\eta \quad (6.16)$$

applying Equation (6.16) to both sides of Equation (6.14) results in

$$L^{-1} L f = L^{-1} \left[-A_n + \beta B_n + M f' \right] \quad (6.17)$$

Focusing on the left hand side of Equation (6.17) and using the boundary conditions given in Equation (6.11) the following relationship is obtained

$$L^{-1} L f = f(\eta) - f(0) - \eta f'(0) - \frac{1}{2} \eta^2 f''(0) \quad (6.18)$$

Setting the right hand side of Equation (6.18) equal to the right side of Equation (6.17) and solving for $f(\eta)$ gives

$$f(\eta) = f(0) + \eta f'(0) + \frac{1}{2} \eta^2 f''(0) + L^{-1} \left[-A_n + \beta B_n + M f' \right] \quad (6.19)$$

substituting in the values for the boundary conditions of Equation (6.11) and letting $f''(0) = \alpha$, the following equation is obtained

$$f(\eta) = \eta + \frac{1}{2}\eta^2\alpha + L^{-1}\left[-A_n + \beta B_n + M f'\right] \quad (6.20)$$

The value of α is yet to be determined and the method of determining α will be discussed later in the chapter. A_n and B_n are nonlinear operators and represent the two nonlinear terms in Equation (6.10). In accordance with the Adomian decomposition method, the nonlinear terms are handled by constructing Adomian polynomials out of the nonlinear terms. Adomian polynomials A_n for a general nonlinear term $N(u)$ are evaluated by the following expression

$$A_n = \left(\frac{1}{n!}\right)\left(\frac{d^n}{d\lambda^n}\right)N(u(\lambda))\Big|_{\lambda=0} \quad (6.21)$$

and assuming that $N(u)$ is the nonlinear function, the Adomian polynomials are given as

$$A_0 = N(u_0) \quad (6.22)$$

$$A_1 = u_1 N'(u_0) \quad (6.23)$$

$$A_2 = u_2 N'(u_0) + \frac{1}{2!}u_1^2 N''(u_0) \quad (6.24)$$

and so on for as many terms as needed. Therefore, the nonlinear term $N(u)$ is given by the sum of the Adomian polynomials

$$N(u) = A_0 + A_1 + A_2 + \dots \quad (6.25)$$

Adomian polynomials are really a Taylor series expansion about the function u_0 and not about a point as is usually the case, (Wazwaz, 2002).

According to the Adomian decomposition method, $f(\eta)$ can be expressed as the sum of an infinite series

$$f(\eta) = \sum_{n=0}^{\infty} f_n(\eta) \quad (6.26)$$

with each component in the series being determined by the following recursive relationship

$$\sum_{n=0}^{\infty} f_n(\eta) = \eta + \frac{1}{2}\alpha\eta^2 + L^{-1}\left(M f' - \sum_{n=0}^{\infty} A_n + \beta \sum_{n=0}^{\infty} B_n\right) \quad (6.27)$$

the recursive relationship given by Equation (6.27) and the Adomian polynomials are easily programmed in an environment such as Mathematica or Maple. The first three Adomian polynomials are given below for each nonlinear operator

$$A_0 = f_0(\eta) f_0''(\eta) \quad (6.28)$$

$$A_1 = f_0(\eta) f_1''(\eta) + f_1(\eta) f_0''(\eta) \quad (6.29)$$

$$A_2 = f_0(\eta) f_2''(\eta) + f_1(\eta) f_1''(\eta) + f_2(\eta) f_0''(\eta) \quad (6.30)$$

$$A_3 = f_0(\eta) f_3''(\eta) + f_1(\eta) f_2''(\eta) + f_2(\eta) f_1''(\eta) + f_3(\eta) f_0''(\eta) \quad (6.31)$$

$$B_0 = (f_0')^2(\eta) \quad (6.32)$$

$$B_1 = 2 f_0'(\eta) f_1'(\eta) \quad (6.33)$$

$$B_2 = (f_1')^2(\eta) + 2 f_0'(\eta) f_2'(\eta) \quad (6.34)$$

$$B_3 = 2 f_1'(\eta) f_2'(\eta) + 2 f_0'(\eta) f_3'(\eta) \quad (6.35)$$

Using Equation (6.27), along with Equations (6.28) – (6.34), the series solution to Equation (6.10) can be obtained. Begin by letting

$$f_0(\eta) = \eta + \frac{1}{2} \alpha \eta^2 \quad (6.36)$$

and letting

$$f_1(\eta) = L^{-1}(M f_0' - A_0 + \beta B_0) \quad (6.37)$$

with the remaining terms in the series being obtained by the following recursive relationship

$$f_{n+1}(\eta) = L^{-1}(M f_n' - A_n + \beta B_n), \quad n \geq 1 \quad (6.38)$$

the first three terms of the series solution are given below

$$f_0(\eta) = \eta \quad (6.39)$$

$$f_1(\eta) = \frac{\alpha \eta^2}{2} + \left(\frac{M}{6} + \frac{\beta}{6} \right) \eta^3 \quad (6.40)$$

$$f_2(\eta) = \left(-\frac{\alpha}{24} + \frac{M \alpha}{24} \right) \eta^4 + \left(\frac{\beta^2}{60} + \frac{M \beta}{40} - \frac{\beta}{60} + \frac{M^2}{120} - \frac{M}{60} \right) \eta^5 \quad (6.41)$$

for this model, the series was taken out to eight-order. Only the first three terms of the series were given above.

6.2.2 Pade Approximants and Boundary Conditions at Infinity

Pade approximants transform a polynomial expression, such as those given by Equation (6.38), into rational functions of polynomials, Baker (1975). In addition, transforming the power series into a rational function of polynomials affords us with more information about the behavior of the solution. As was shown by Boyd (1997), power series alone are not very useful for solving boundary-value problems, which is due to the fact that the radius of convergence is not large enough to account for both boundaries of the domain. Therefore, combining a series solution obtained through the Adomian decomposition method, with Pade approximants is an effective and elegant tool for handling boundary value problems on infinite or semi-infinite domains, Hayat et al. (2009). As was also shown by Boyd (1997), the Pade approximant will converge on the entire real axis if the function, $f(\eta)$ in this case, is free of discontinuities. Furthermore, the diagonal approximants are the most accurate approximants, Boyd (1997) and were the only type of approximants used in obtaining a solution to this fluid flow model.

The value of α is obtained by using the boundary condition at infinity $f'(\infty) = 0$, taking the Pade approximant of the series solution of $f(\eta)$, taking the limit of the Pade approximant as $\eta \rightarrow \infty$, setting that equal to zero and solving for α . This procedure would be done for various orders of Pade approximants until α converges to a solution. For example, the second order Pade approximant for $\beta = 1$ and $M = 0$ is given by

$$f(\eta)_{[2/2]} = \frac{6\eta(4 - 6\alpha^2 + 3\alpha\eta - 3\alpha^3\eta)}{6\alpha\eta - 4(-6 + \eta^2) + \alpha^2(-36 + 3\eta^2)} \quad (6.42)$$

then

$$\lim_{\eta \rightarrow \infty} f(\eta)_{[2/2]} = 0 \quad (6.43)$$

gives the values of α . For this case α had three roots: $\alpha = -1$, $\alpha = 0$, and $\alpha = 1$. Following the procedure given by Equations (6.42)-(6.43) out to a fifth-order Pade Approximant, gives a convergent value of $\alpha = -1$. This analysis was carried out for two different values of β and six different values of M . Tables 6.1 and 6.2 show the error between the exact and analytical solution for two different cases of M and $\beta = 1$. Figures 6.1 – 6.5 give the boundary layer profiles and velocity profiles calculated from this analysis

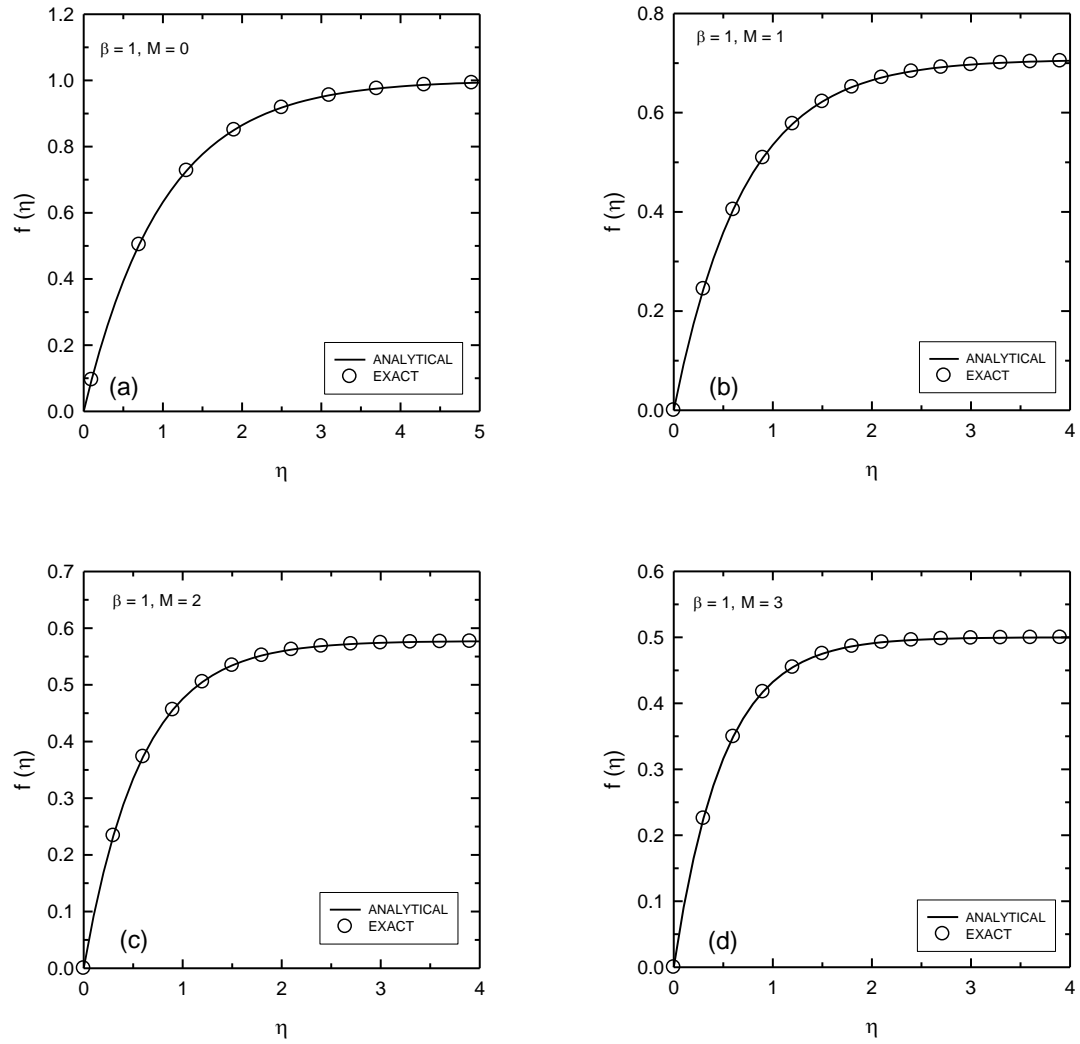


Figure 6.1: Plots of boundary layer thickness as a function of distance down the plate. The solid line represents the analytical solution while the open circles represent the exact solution. (a) $\beta = 1$ and $M = 0$, (b) $\beta = 1$ and $M = 1$, (c) $\beta = 1$ and $M = 2$, (d) $\beta = 1$ and $M = 3$. The analytical solution is in very good agreement with exact solution.

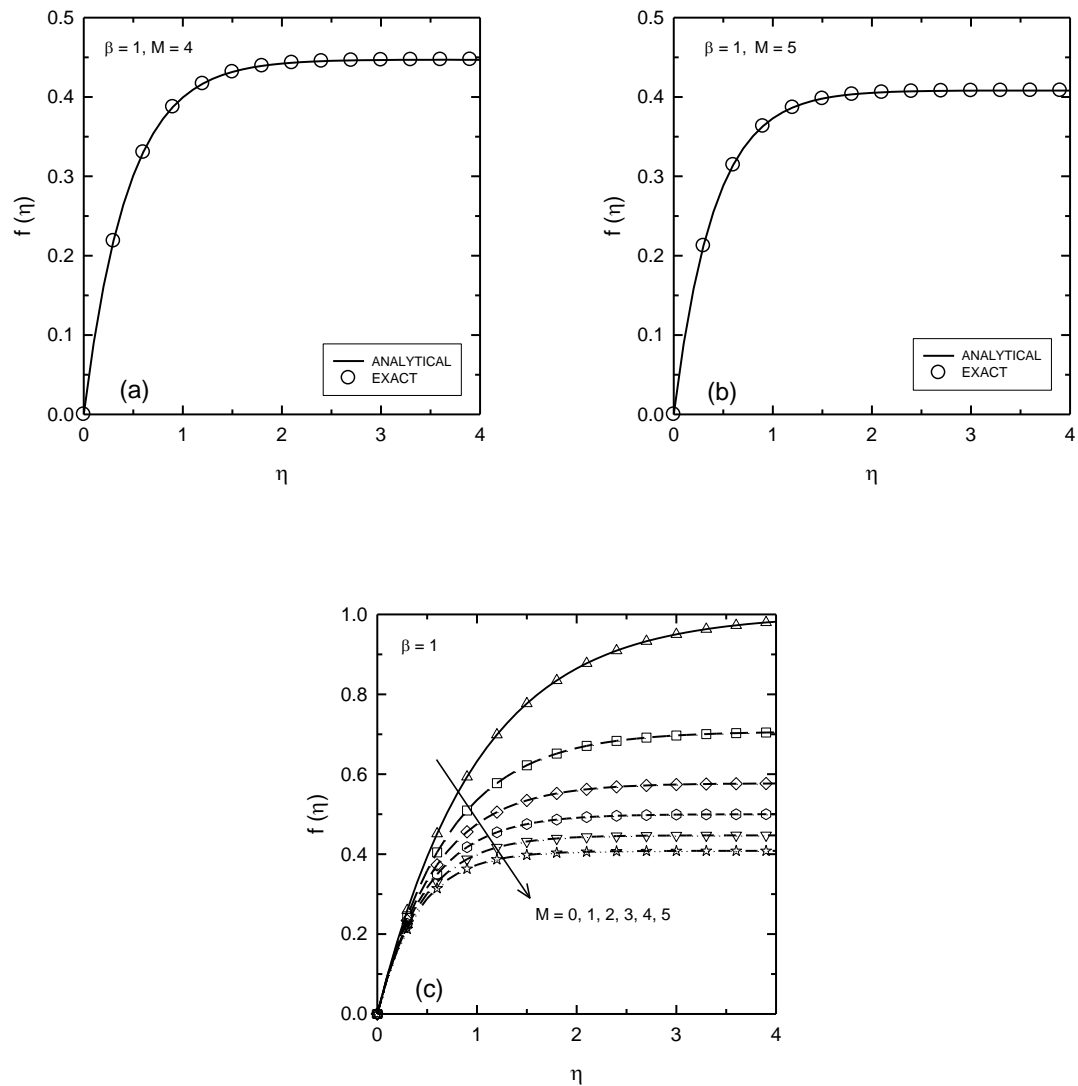


Figure 6.2: Plot of the boundary layer thickness as a function of distance down the plate. The solid line represents the analytical solution while the open circles represent the exact solution. (a) $\beta = 1$ and $M = 4$, (b) $\beta = 1$ and $M = 5$, (c) $\beta = 1$ and a comparison of all M values. Note the good agreement between the analytical and exact solution for all cases. The overall effect of a magnetic field is to decrease the boundary layer thickness.

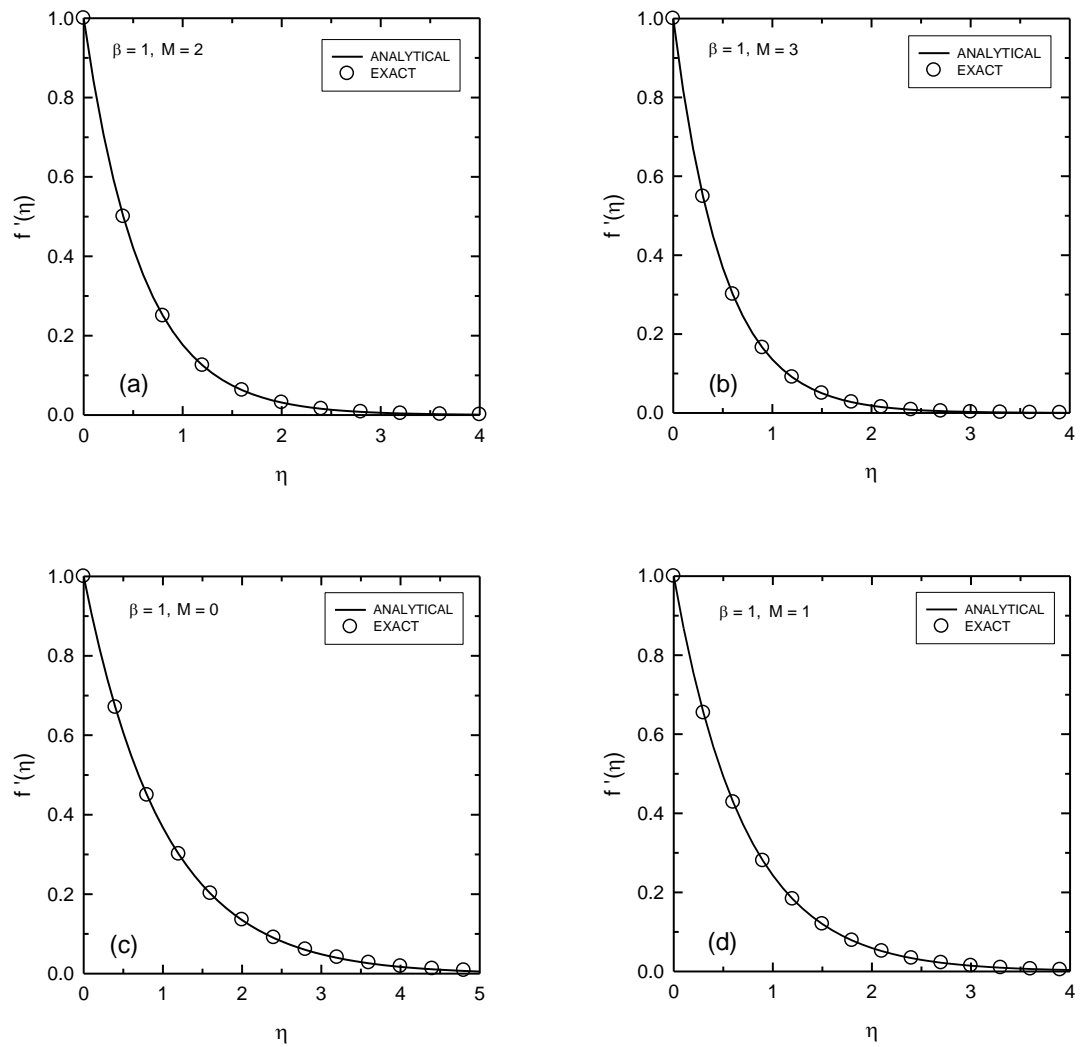


Figure 6.3: Plot velocity profiles as a function of distance down the plate. The solid line represents the analytical solution and open circles represent the exact solution. (a) $\beta = 1$ and $M = 2$, (b) $\beta = 1$ and $M = 3$, (c) $\beta = 1$ and $M = 2$, (d) $\beta = 1$ and $M = 1$. The analytical solution is in very good agreement with exact solution.

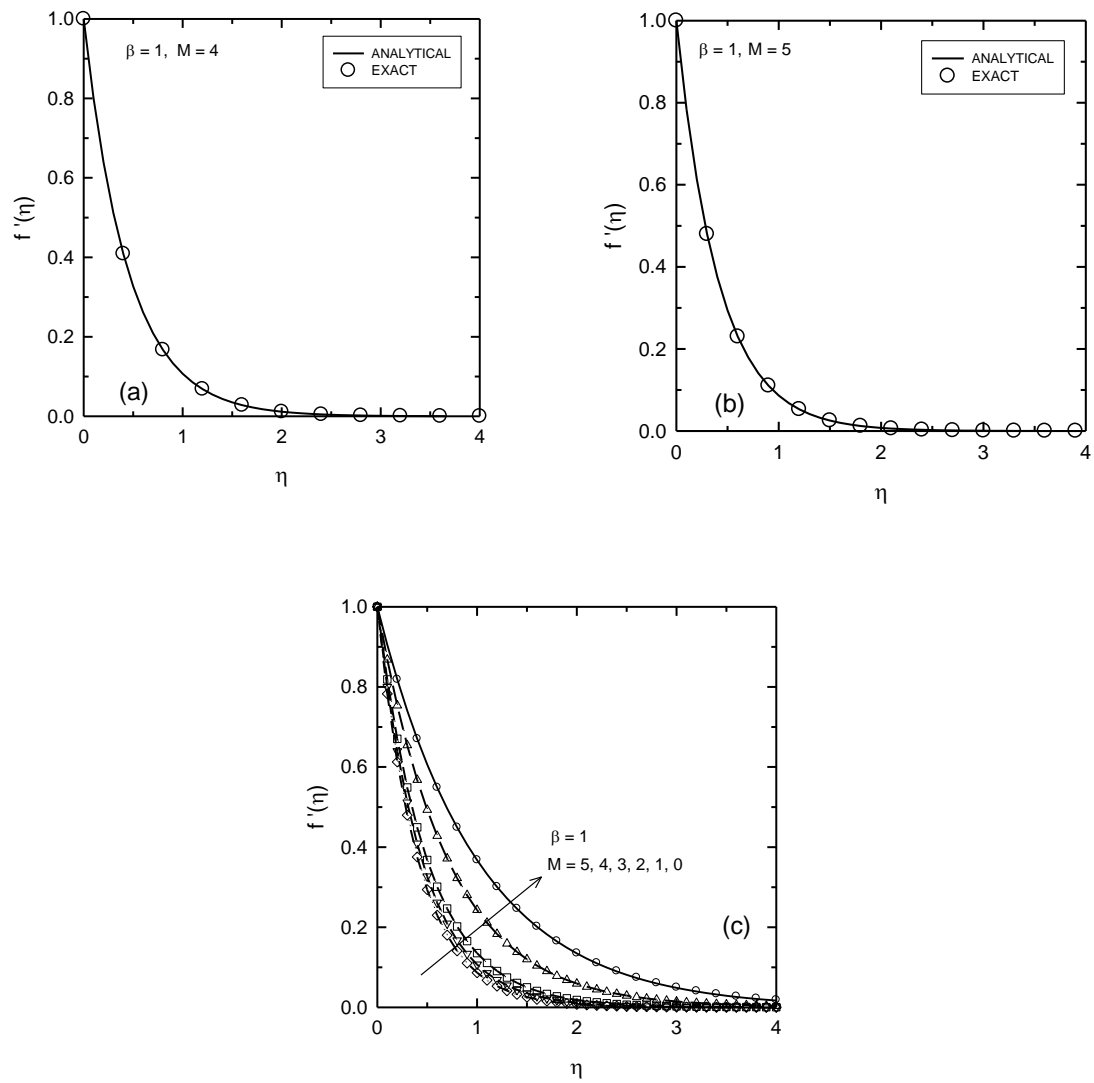


Figure 6.4: Plots of the velocity profiles as a function of distance down the plate. The solid line represents the analytical solution and open circles represent the exact solution. (a) $\beta = 1$ and $M = 4$, (b) $\beta = 1$ and $M = 5$, (c) Comparison of all velocity profiles for all values of M . Note the good agreement between the analytical and exact solution for all cases.

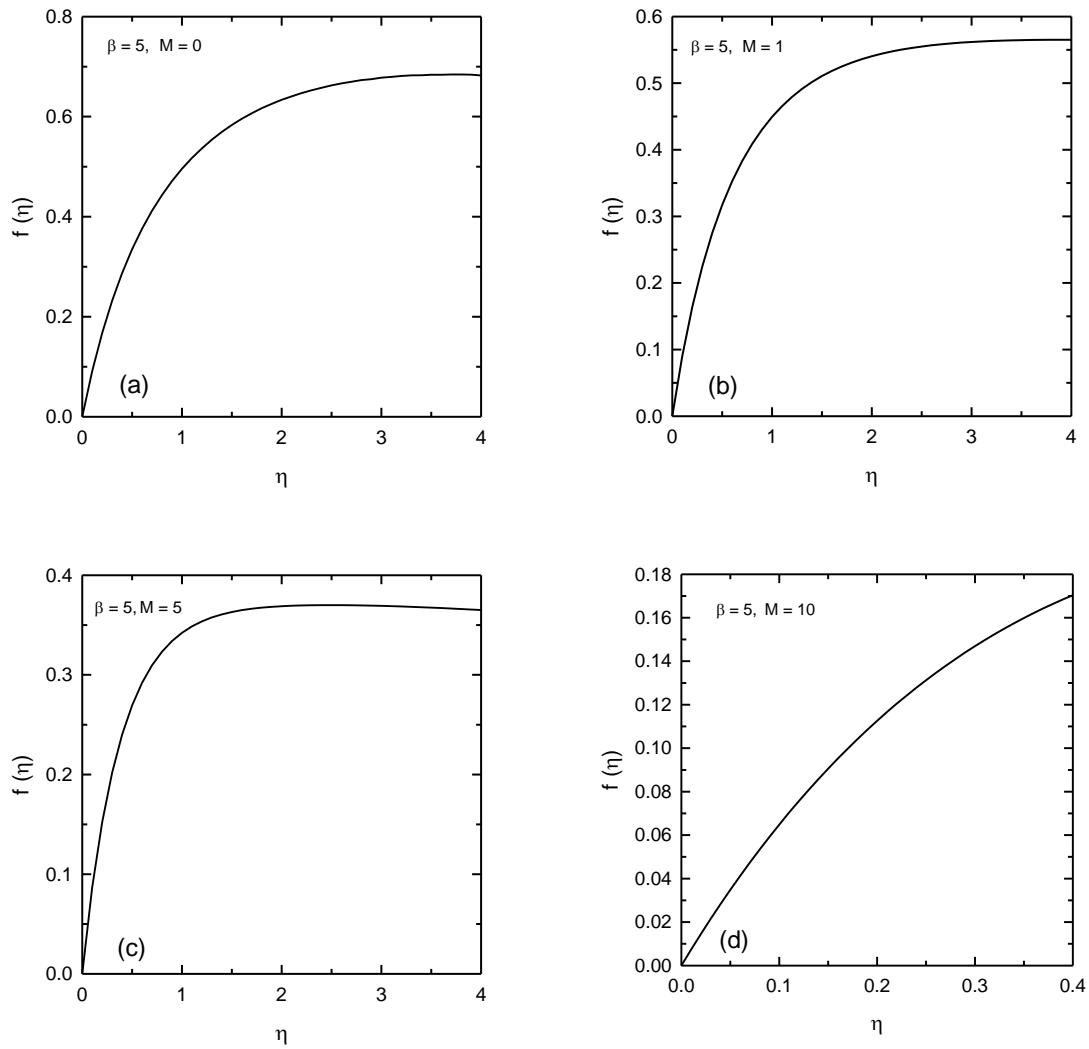


Figure 6.5: Plots of boundary layer thickness as a function of distance down the plate. The solid line represents the analytical solution. No exact solution exists for $\beta \neq 1$. (a) $\beta = 5$ and $M = 0$, (b) $\beta = 5$ and $M = 1$, (c) $\beta = 5$ and $M = 2$, (d) $\beta = 10$ and $M = 10$. Note the decreased range of validity for the last case (d).

Table 6.1: Percent error for $\beta = 1$ and $M = 1$ velocity profile given in Figure 6.3(d)

Analytical Solution	Exact Solution	Percent Error
1	1	0
0.868125	0.868123	0.000191961
0.75364	0.753638	0.000182275
0.654252	0.654251	0.000175895
0.567972	0.567971	0.000240716
0.493071	0.493069	0.000371505
0.428047	0.428044	0.000607727
0.371599	0.371595	0.000850682
0.322594	0.322591	0.00102022
0.280053	0.280049	0.00141589
0.243121	0.243117	0.00192508
0.211061	0.211055	0.00252695
0.183228	0.183222	0.00302068
0.159066	0.159059	0.00424433
0.138091	0.138083	0.00554773
0.119881	0.119873	0.0067248
0.104074	0.104065	0.00870891
0.090351	0.0903411	0.0109508
0.0784378	0.0784272	0.0134475
0.0680973	0.0680845	0.01874
0.0591188	0.0591057	0.0220717
0.0513256	0.0513111	0.028332
0.0445591	0.0445444	0.0330012
0.0386866	0.03867	0.0430466
0.033589	0.0335703	0.0557121
0.0291628	0.0291432	0.0674099
0.0253203	0.0252999	0.0808164
0.0219858	0.0219634	0.101838
0.0190899	0.019067	0.120445
0.0165778	0.0165525	0.152717
0.0143959	0.0143696	0.182892
0.0125052	0.0124746	0.245715
0.0108606	0.0108295	0.287217
0.00943843	0.00940132	0.394722
0.00819868	0.00816151	0.455421
0.00712289	0.0070852	0.532048
0.00619141	0.00615083	0.65984
0.0053802	0.00533968	0.758998
0.0046856	0.0046355	1.08078
0.00406891	0.00402418	1.11139

Table 6.2: Percent error for $\beta = 1$ and $M = 2$ velocity profile given in Figure 6.3(a)

Analytical Solution	Exact Solution	Percent Error
1	1	0
0.840965	0.840965	8.63338×10^{-6}
0.707223	0.707222	0.0000221536
0.59475	0.594749	0.0000420724
0.500164	0.500163	0.0000697424
0.42062	0.42062	0.000106289
0.353727	0.353727	0.000160622
0.297473	0.297472	0.000231342
0.250164	0.250163	0.000334832
0.21038	0.210379	0.000461077
0.176922	0.176921	0.000653526
0.148786	0.148785	0.000898852
0.125124	0.125123	0.00124924
0.105226	0.105224	0.00167273
0.0884916	0.0884895	0.00233538
0.074419	0.0744166	0.00316355
0.0625845	0.0625818	0.00429114
0.0526321	0.0526291	0.00573427
0.0442626	0.0442592	0.00756393
0.0372243	0.0372205	0.0102077
0.0313053	0.0313011	0.0134194
0.0263279	0.0263231	0.0180891
0.0221419	0.0221368	0.0230024
0.0186219	0.0186163	0.0300032
0.0156619	0.0156557	0.0397903
0.0131724	0.0131659	0.0494378
0.0110791	0.011072	0.0635272
0.00931858	0.0093112	0.0792694
0.00783789	0.0078304	0.0957481
0.00659288	0.00658509	0.118255
0.00554572	0.00553783	0.142404
0.00466489	0.00465712	0.166714
0.00392389	0.00391648	0.189222
0.00330053	0.00329362	0.209779
0.0027759	0.00276982	0.21949
0.00233429	0.00232932	0.21319
0.00196218	0.00195888	0.168733
0.00164861	0.00164735	0.0767352
0.00138452	0.00138536	0.0610291
0.0011612	0.00116504	0.330045

6.3 Coupled Fluid Flow and Mass Transport at a Vertical Electrode

In this section of the chapter a model is proposed that accounts for mass transfer and fluid flow at a vertical electrode. The model is based upon the boundary layer equations for mass transfer in natural convection at a vertical plate under the influence of a magnetic field. The original boundary layer equations and similarity transformation was proposed by Levich (1962). In the formulation by Levich however, the effect of a magnetic field was not taken into account. In the work by Fahidy (1973), the same boundary layer equations proposed by Levich were used, but with a slight modification to the similarity equations in which the effect of a magnetic field was included. Fahidy obtained a first order perturbation solution to the coupled system of nonlinear differential equations and was able to derive relationships for predicting the effect of a magnetic field on the limiting current density. Figure 6.6 gives a schematic representation of the velocity and concentration profiles next to vertical electrode with a magnetic field parallel to the surface.

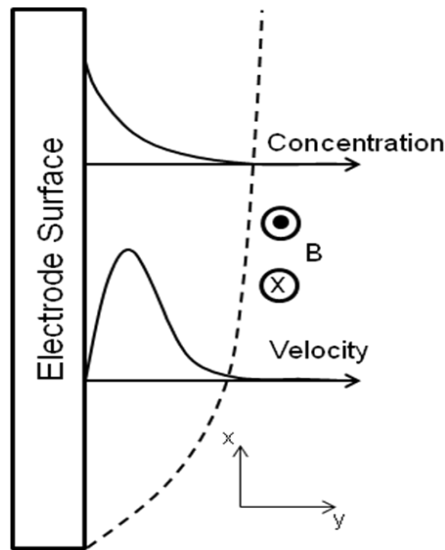


Figure 6.6: Schematic representation of natural convective boundary layer on a vertical electrode. The magnetic field is parallel to the electrode surface.

For the modeling being done in this section, the same equations Proposed by Levich and Fahidy will be used here. However, the main difference between the model given by Fahidy and the model given presently is that a higher order solution was obtained by use of the Adomian

decomposition method and Fahidy made no attempt to quantify his results. The main objectives of this model are to understand the effect of a magnetic field on fluid flow, mass transport, and understand the effect of a magnetic field on the limiting current density.

6.3.1 Mathematical Formulation of the Coupled Model

The following equations describe a magneto-electrolytic system, Fahidy (1973) and Shercliff (1965).

$$\text{div } \mathbf{v} = 0 \quad (6.44)$$

$$\text{div } \mathbf{B} = 0 \quad (6.45)$$

$$\mathbf{j} = \text{curl } \mathbf{B} \quad (6.46)$$

$$\mathbf{j} = \sigma (\mathbf{E} + \mathbf{v} \times \mathbf{B}) \quad (6.47)$$

$$\frac{\partial \mathbf{B}}{\partial t} + (\mathbf{v} \text{ grad}) \mathbf{B} = (\mathbf{B} \text{ grad}) \mathbf{v} + \lambda \text{ div grad } \mathbf{B} \quad (6.48)$$

$$\rho \frac{\partial \mathbf{v}}{\partial t} + (\mathbf{v} \text{ grad}) \mathbf{v} + \text{grad } p = (\mathbf{B} \text{ grad}) \frac{\mathbf{B}}{\mu} + \mathbf{F} + \nu \rho \text{ div grad } \mathbf{v} \quad (6.49)$$

Given the fact that aqueous electrolytes have low electrical conductivities, the induced magnetic field and electric currents may be neglected. The approximation is known as the low magnetic Reynolds number approximation. In accordance with this assumption, \mathbf{B} can be replaced with the uniform magnetic field strength, B_0 and \mathbf{j} can be replaced by the uniform electric current density j_0 . Equations (6.47) and (6.48) can be ignored and the MHD effects are accounted for by the term $j_0 B_0$, which represents the MHD force density. At steady state, Equation (6.49) reduces to

$$(\mathbf{v} \text{ grad}) \mathbf{v} + \text{grad } p = \frac{1}{\rho} \mathbf{j} \times \mathbf{B} + \nu \text{ div grad } \mathbf{v} + \mathbf{F} \quad (6.50)$$

The concentration distribution across the two-dimensional boundary layer is given as, Levich (1962)

$$D \frac{\partial^2 c}{\partial y^2} = v_x \frac{\partial c}{\partial x} + v_y \frac{\partial c}{\partial y} \quad (6.51)$$

Therefore, Equation (6.44), (6.50), and (6.51) along with the appropriate boundary conditions, completely describe the mass transfer occurring at a vertical electrode, Fahidy (1973). Equations (6.50) and (6.51) can be furthered simplified to give the following equations

$$v_x \frac{\partial v_x}{\partial x} + v_y \frac{\partial v_x}{\partial y} = \nu \frac{\partial^2 v_x}{\partial y^2} + g\alpha\phi + \frac{j_0 B_0}{\rho} \quad (6.52)$$

$$v_x \frac{\partial \phi}{\partial x} + v_y \frac{\partial \phi}{\partial y} = D \frac{\partial^2 \phi}{\partial y^2} \quad (6.53)$$

with boundary conditions defined as

$$y = 0; \quad v_x = v_y = 0; \quad \phi = 1$$

$$y \rightarrow \infty; \quad v_x = 0; \quad \phi = 0$$

ϕ is the dimensionless concentration, and α is the densification coefficient. The similarity transformation used by Levich (1962) to reduce the system of partial differential equations to a system of coupled nonlinear ordinary differential equations is reproduced below.

Introducing the following similarity variable

$$\eta = \left(\frac{g\alpha}{4\nu^2} \right)^{1/4} \frac{y}{x^{1/4}} \quad (6.54)$$

and the stream function

$$\psi = 4\nu \left(\frac{g\alpha}{4\nu^2} \right)^{1/4} x^{3/4} f(\eta) \quad (6.55)$$

in terms of the new variables, the velocity components are

$$v_x = 4\nu \left(\frac{g\alpha x}{4\nu^2} \right)^{1/2} f'(\eta) \quad (6.56)$$

$$v_y = -\frac{\partial \psi}{\partial x} = \nu \left(\frac{g\alpha}{4\nu^2} \right)^{1/4} \frac{(\eta f' - 3f)}{x^{1/4}} \quad (6.57)$$

gives the following system of nonlinear differential equations

$$f''' + 3ff'' - 2(f')^2 + \phi = 0 \quad (6.58)$$

$$\phi'' + 3Pr f \phi' = 0 \quad (6.59)$$

with boundary conditions given as

$$f(\eta=0) = 0, \quad f'(\eta=0) = 0, \quad \text{and,} \quad f'(\eta \rightarrow \infty) = 0 \quad (6.60)$$

$$\phi(\eta=0) = 1, \quad \text{and} \quad \phi(\eta \rightarrow \infty) = 0 \quad (6.61)$$

This was the set of coupled differential equations that Levich derived for free convective mass transfer at a vertical plate. Equations (6.58) – (6.59) were slightly modified by Fahidy to account for the effect of a magnetic field on fluid flow and mass transport. The equations derived by Fahidy are given below

$$f''' + 3f f'' - 2(f')^2 + \phi = -\frac{j_0 B_0}{\rho g \alpha} \quad (6.62)$$

$$\phi'' + 3Pr f \phi' = 0 \quad (6.63)$$

with the same boundary conditions given by Equations (6.60) and (6.61).

In the analysis by Fahidy, a series expansion technique was used to obtain functions for the boundary layer profile and concentration profile. The boundary layer profile is give by

$$f(\eta) = \frac{\beta \eta^2}{2!} - \frac{\eta^3}{3!} \left(1 + \frac{j_0 B_0}{\rho g \alpha} \right) + \eta^4 \frac{\left(\frac{1}{2} \beta Pr \right)^{1/3}}{4 \Gamma(3/4)} \quad (6.64)$$

and the concentration profile, to first order, is given by

$$\phi \approx 1 - \frac{\left(\frac{1}{2} \beta Pr \right)^{1/3} \eta}{\Gamma(4/3)} \quad (6.65)$$

additionally, Fahidy also derived expressions for the boundary layer thickness and the limiting current density. The boundary layer thickness was determined to be

$$\delta_M = \frac{x^{1/4}}{a \left(\frac{1}{3} + \frac{1}{2} \frac{j_0 B_0}{\rho g \alpha} \right)^{1/4} Pr^{1/4} \left(\frac{g \alpha}{4 \nu} \right)^{1/4}} \quad (6.66)$$

using

$$Nu = a' \left(\frac{1}{3} + \frac{1}{2} \frac{j_0 B_0}{\rho g \alpha} \right)^{1/4} Pr^{1/4} Gr^{1/4} \quad (6.67)$$

with the expression for limiting current density given as

$$j_0 = 1.105 a' \frac{n F D}{F_1(\beta, \gamma)} \left(\frac{g \alpha}{4 \nu^2 h} \right)^{1/4} c_0 \quad (6.68)$$

where Nu is the Nusselt number, Pr is the Prandtl number, j_0 is the current density, Gr is the Grashof number, g is the acceleration due to gravity, a and a' are constants, β is a parameter

related to the MHD force, $F_1(\beta, \gamma)$ is a complex function of α and β , B_0 is the magnetic field strength, ν is the kinematic viscosity, ρ is the density, F is Faraday's constant, D is the diffusivity of the electrolyte, Γ is the gamma function, and c_0 is the bulk electrolyte concentration.

6.4 Solution by Adomian Decomposition Method

To obtain a solution through the Adomian decomposition method, Equations (6.62) – (6.63) are rewritten in operator form as

$$L_1 f = 2(f')^2 - 3ff'' - \phi - \frac{j_0 B_0}{\rho g \alpha} \quad (6.69)$$

$$L_2 \phi = -3Pr f \phi' \quad (6.70)$$

with the boundary conditions give as

$$f(\eta=0)=0, \quad f'(\eta=0)=0, \quad \text{and,} \quad f'(\eta \rightarrow \infty)=0 \quad (6.71)$$

$$\phi(\eta=0)=1, \quad \text{and} \quad \phi(\eta \rightarrow \infty)=0 \quad (6.72)$$

where

$$L_1 = \frac{d^3}{d\eta^3} \quad (6.73)$$

and

$$L_2 = \frac{d^2}{d\eta^2} \quad (6.74)$$

with the inverse of the linear differential operators, L_1 and L_2 , defined as

$$L_1^{-1} = \int_0^\eta \int_0^\eta \int_0^\eta (\cdot) d\eta d\eta d\eta \quad (6.75)$$

and

$$L_2^{-1} = \int_0^\eta \int_0^\eta (\cdot) d\eta d\eta \quad (6.76)$$

applying Equation (6.75) to both sides Equation (6.69) and applying Equation (6.76) to both sides of Equation (6.70), using the boundary condition given by Equations (6.71) and (6.72), and solving for $f(\eta)$ and $\phi(\eta)$ gives

$$f(\eta) = \frac{\eta^2}{2} \alpha_1 + L_1^{-1} \left[2(f')^2 - 3f f'' - \phi - \gamma \right] \quad (6.77)$$

$$\phi(\eta) = 1 + \alpha_2 \eta + L_2^{-1} \left[-3 \text{Pr} f \phi' \right] \quad (6.78)$$

where $\gamma = j_0 B_0 / \rho g \alpha$ and α_1 and α_2 are undetermined constants which are used to handle the boundary conditions at infinity, Equations (6.71) and (6.72). Solving for the constants, α_1 and α_2 , and accounting for the boundary conditions at infinity will be discussed later in the chapter.

The second term on the right hand side of Equation (6.77) and the third term on the right hand side of Equation (6.78) contain nonlinear operators. The nonlinear operator are defined as

$$N(f) = (f')^2 \quad (6.79)$$

$$R(f) = f f'' \quad (6.80)$$

for Equation (6.77) and

$$J(f, \phi) = f \phi' \quad (6.81)$$

for Equation (6.78). The nonlinear operators are decomposed as

$$N(f) = \sum_{n=0}^{\infty} A_n \quad (6.82)$$

$$R(f) = \sum_{n=0}^{\infty} B_n \quad (6.83)$$

$$J(f, \phi) = \sum_{n=0}^{\infty} C_n \quad (6.84)$$

where A_n , B_n , and C_n are the Adomian polynomials for each nonlinear operator. The Adomian polynomial for a general nonlinear operator is defined as

$$A_n = \frac{1}{n!} \left[\frac{d^n}{d\lambda^n} N \left(\sum_{n=0}^{\infty} \lambda^n f_n \right) \right]_{\lambda=0}, \quad n \geq 0 \quad (6.85)$$

defining an Adomian polynomial for each nonlinear term, which can be done quite easily in Mathematica, yields the following

$$A_0 = (f'_0(\eta))^2 \quad (6.86)$$

$$A_1 = 2 f'_0(\eta) f'_1(\eta) \quad (6.87)$$

$$A_2 = (f'_1(\eta))^2 + 2 f'_0(\eta) f'_2(\eta) \quad (6.88)$$

⋮

$$B_0 = f_0(\eta) f''_0(\eta) \quad (6.89)$$

$$B_1 = f_1(\eta) f''_0(\eta) + f_0(\eta) f''_1(\eta) \quad (6.90)$$

$$B_2 = f_2(\eta) f''_0(\eta) + f_1(\eta) f''_1(\eta) + f_0(\eta) f''_2(\eta) \quad (6.91)$$

⋮

$$C_0 = f_0(\eta) \phi'_0(\eta) \quad (6.92)$$

$$C_1 = f_1(\eta) \phi'_0(\eta) + f_0(\eta) \phi'_1(\eta) \quad (6.93)$$

$$C_2 = f_2(\eta) \phi'_0(\eta) + f_1(\eta) \phi'_1(\eta) + f_0(\eta) \phi'_2(\eta) \quad (6.94)$$

⋮

the terms A_n , B_n , and J_n can be computed for as many terms as deemed necessary or for higher accuracy in the approximation.

In the ADM method, it is assumed that $f(\eta)$ and $\phi(\eta)$ can be expanded as an infinite series

$$f(\eta) = \sum_{n=0}^{\infty} f_n(\eta) \quad (6.95)$$

$$\phi(\eta) = \sum_{n=0}^{\infty} \phi_n(\eta) \quad (6.96)$$

using Equations (6.95), (6.96), and (6.85) a set of relationship can be defined for each function, $f(\eta)$ and $\phi(\eta)$ as

$$\sum_{n=0}^{\infty} f_n(\eta) = \frac{\eta^2}{2} \alpha_1 + L_1^{-1} \left[\sum_{n=0}^{\infty} 2 A_n - \sum_{n=0}^{\infty} 3 B_n - \sum_{n=0}^{\infty} \phi_n(\eta) - \gamma \right] \quad (6.97)$$

$$\sum_{n=0}^{\infty} \phi_n(\eta) = 1 + \alpha_2 \eta - L_2^{-1} \left[\sum_{n=0}^{\infty} 3 \text{Pr } C_n \right] \quad (6.98)$$

with the individual terms of the Adomian series solution being given by the following recursive relationships

$$f_0(\eta) = \frac{\eta^2 \alpha_1}{2} - L_1^{-1}[\Omega] = \frac{\eta^2 \alpha_1}{2} - \frac{\eta^3 \gamma}{6} \quad (6.99)$$

$$\phi_0(\eta) = 1 + \alpha_2 \eta \quad (6.100)$$

$$f_{n+1}(\eta) = L_1^{-1}[2 A_n - 3 B_n - \phi_n], \quad n \geq 0 \quad (6.101)$$

$$\phi_{n+1}(\eta) = -L_2^{-1}[3 Pr C_n], \quad n \geq 0 \quad (6.102)$$

the recursive Equations (6.101) and (6.201) are coded into the computer algebra package Mathematica. For this model, the 11-term and 12-term approximations to $f(\eta)$ and $\phi(\eta)$ were obtained, respectively. However, only the first three terms are given below.

$$f_0(\eta) = \frac{\eta^2 \alpha_1}{2} - \frac{\eta^3 \gamma}{6} \quad (6.103)$$

$$f_1(\eta) = -\frac{\eta^3}{6} - \frac{\alpha_2 \eta^4}{24} + \frac{\alpha_1^2 \eta^5}{120} \quad (6.104)$$

$$f_2(\eta) = \left(\frac{\alpha_1 \alpha_2}{1008} + \frac{\alpha_1 \alpha_2 Sc}{1680} \right) \eta^7 - \left(\frac{13 \alpha_1^3}{40320} + \frac{\alpha_2 \gamma}{8064} + \frac{\alpha_2 Sc \gamma}{13440} \right) \eta^8 + \frac{\alpha_1 \gamma}{20160} \eta^9 \quad (6.105)$$

⋮

$$\phi_0(\eta) = 1 + \alpha_2 \eta \quad (6.106)$$

$$\phi_1(\eta) = -\frac{\alpha_1 \alpha_2 Sc \eta^4}{8} + \frac{\alpha_2 Sc \gamma \eta^5}{40} \quad (6.107)$$

$$\phi_2(\eta) = \frac{\alpha_2 Sc}{40} \eta^5 + \frac{\alpha_2^2 Sc}{240} \eta^6 - \left(\frac{\alpha_1^2 \alpha_2 Sc}{1680} - \frac{\alpha_1^2 \alpha_2 Sc^2}{56} \right) \eta^7 - \frac{\alpha_1 \alpha_2 Sc^2 \gamma}{28} \eta^8 + \frac{\alpha_2 Sc^2 \gamma^2}{1152} \eta^9 \quad (6.108)$$

⋮

in Equations (6.103) – (6.108), the Prandtl number has been replaced by the Schmidt number. The approximations were taken to 11th -order for the boundary layer thickness solution and to 12th – order for the species distribution from the vertical electrode.

The next step is to determine the unknown constants, α_1 and α_2 , and as was shown in a previous section, Pade approximants must be used. However, since Equations (6.69) and (6.70) are coupled, this requires considerable more computational work.

6.4.1 Pade Approximants for a Coupled System of Equations

Following the same procedure that was used in Section 6.1.2, the values of α_1 and α_2 are obtained by using boundary conditions at infinity for $f'(\infty) = 0$ and $\phi(\infty) = 0$. Taking the Pade approximant of the series solution for $f(\eta)$ and $\phi(\eta)$, taking the limit of the Pade approximants as $\eta \rightarrow \infty$, setting each Pade Approximant equal to zero and solving for α_1 and α_2 simultaneously gives the numerical values of α_1 and α_2 . Repeating this procedure for various orders of Pade approximant will lead to convergent values for α_1 and α_2 .

First, the Pade approximant of each Adomian series solution is taken as shown below

$$\text{PADE}_1[\eta] = \text{Simplify}[\text{PadeApproximant}[f(\eta), \{\eta, 0, 3, 3\}]] \quad (6.109)$$

$$\text{PADE}_2[\eta] = \text{Simplify}[\text{PadeApproximant}[\phi(\eta), \{\eta, 0, 3, 3\}]] \quad (6.110)$$

In Equations (6.109) and (6.110) two new functions have been defined, PADE_1 and PADE_2 , which give the third order Pade approximants of $f(\eta)$ and $\phi(\eta)$. Next, the limit of PADE_1 and PADE_2 must be taken as $\eta \rightarrow \infty$, and then each function is equated to zero, and finally solve for α_1 and α_2 simultaneously. This computational procedure can be coded in one line in Mathematic, as shown below

$$\text{sol1} = \text{Solve}[\{\text{Limit}[\text{PADE}_1[\eta], \eta \rightarrow \infty] = 0, \text{Limit}[\text{PADE}_2[\eta], \eta \rightarrow \infty] = 0\}, \{\alpha_1, \alpha_2\}]$$

therefore, determining α_1 and α_2 is equivalent to solving two equations in two unknowns; a computation that is handled rather elegantly in Mathematica. It should be noted that PADE_1 and PADE_2 are not built-in functions in Mathematica, they are functions defined by the author. However, built-in functions in Mathematica are: Simplify, PadeApproximant, Limit, and Solve. The results for this analytical model are shown below in Figures 6.7 and 6.7.

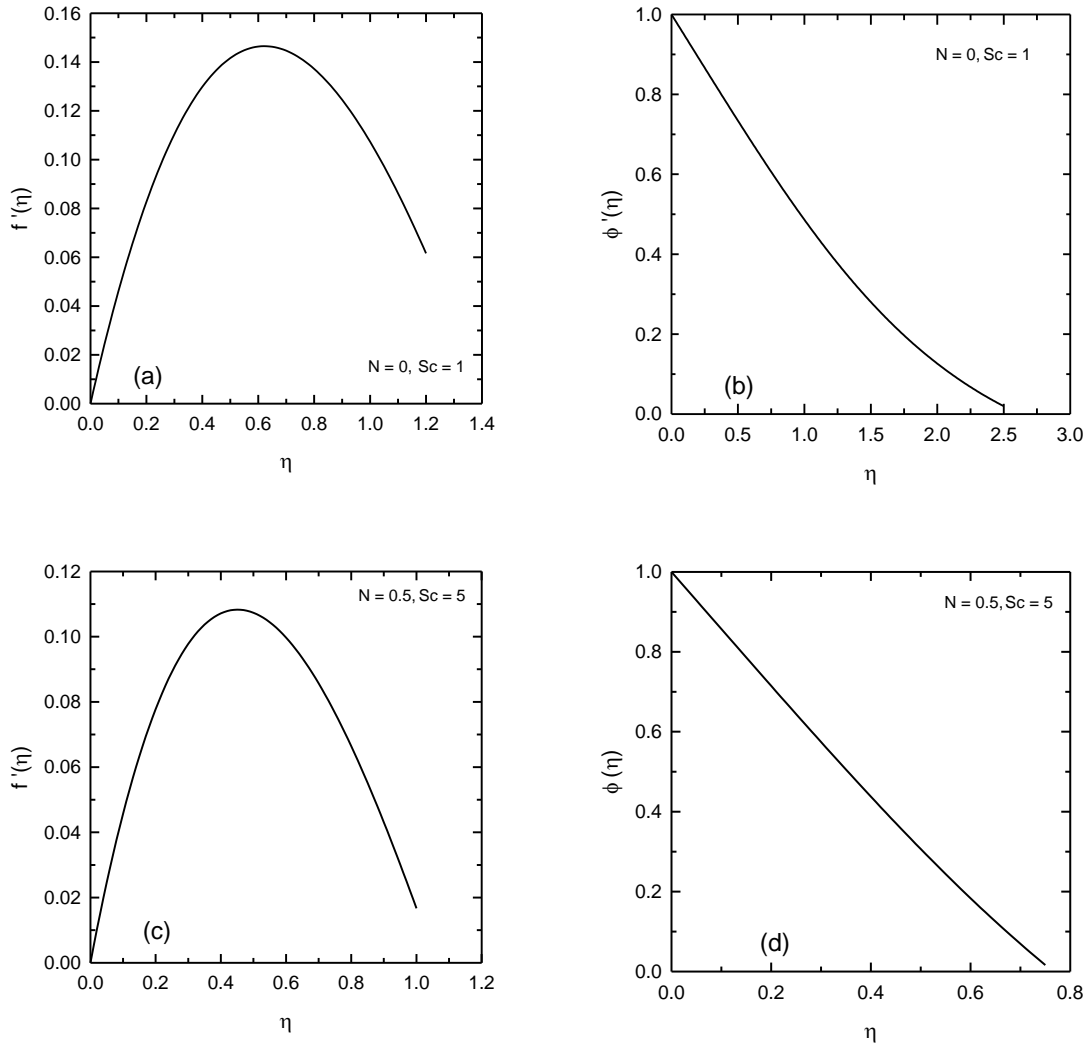


Figure 6.7: Velocity and concentration profiles for different values of the magnetic parameter N and Schmidt number, Sc ; (a) velocity profile: $N = 0$ and $Sc = 1$, (b) concentration profile: $N = 0$ and $Sc = 1$, (c) velocity profile: $N = 0.5$ and $Sc = 5$, (d) concentration profile: $N = 0.5$ and $Sc = 5$.

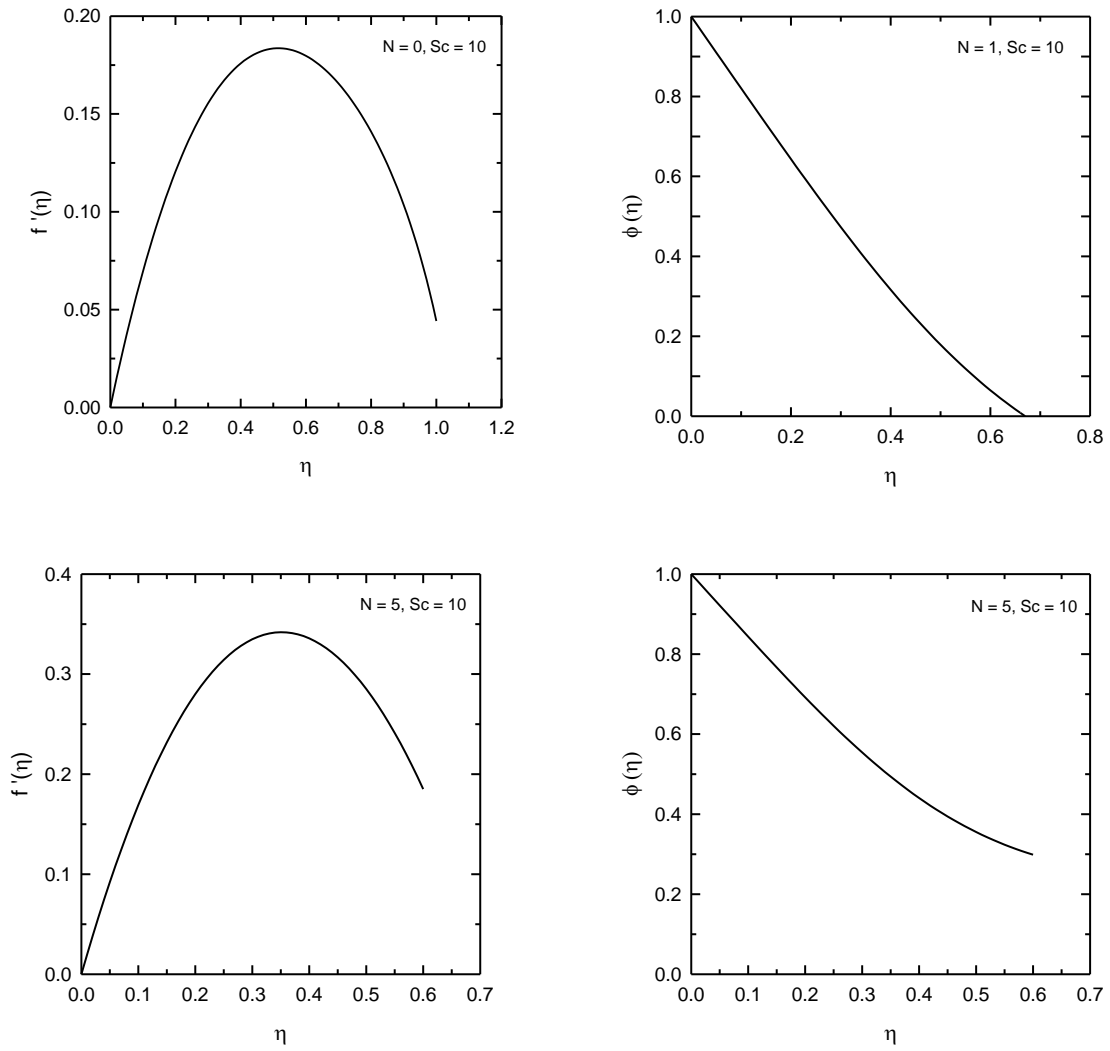


Figure 6.8: Velocity and concentration profiles for different values of the magnetic parameter, N and Schmidt number, Sc ; (a) velocity profile: $N = 0$ and $Sc = 10$, (b) concentration profile: $N = 1$ and $Sc = 10$, (c) velocity profile: $N = 5$ and $Sc = 10$, (d) concentration profile: $N = 5$ and $Sc = 10$.

6.5 Scaling Analysis

The term ‘scaling’ describes a simple situation: the existence of a power-law relationship between certain variables y and x

$$y = A x^\alpha \quad (6.111)$$

where A and α are constants. Scaling laws always reveal an important property of the model or system under investigation: its self-similarity. Self-similar means that the model or system reproduces itself on different time and length scales, Barenblatt (2003). Scaling analysis is also a method for systematically simplifying the governing equations by determining which terms can be ignored in a given problem. Through scaling analysis, the characteristic values of all of the problem variables can be obtained. Additionally, dimensionless parameters that have physical meaning for the particular system being researched can be derived, Dantzig et al. (2001).

6.5.1 Coupled Fluid Flow and Mass Transport

In this Section Equations (6.52) and (6.53) will be used again to derive relationships for the limiting current density and boundary layer thickness. However, instead of solving this system of equations using the ADM, scaling techniques will be employed. The solution technique is based on scaling methods developed by Ruckenstein, (1987). In the scaling analysis methodology developed by Ruckenstein, the transport equations are not solved in the traditional way. Instead, the transport equations are replaced by algebraic expressions, which are obtained by scaling the transport equations. The constants involved in the algebraic expressions are determined by comparing them with exact asymptotic solutions, Ruckenstein (1987).

The laminar convection from a vertical electrode with a magnetic field applied parallel to the surface of the electrode can be described by the following equations

$$\frac{\partial u}{\partial x} + \frac{\partial v}{\partial y} = 0 \quad (6.112)$$

$$u \frac{\partial u}{\partial x} + v \frac{\partial u}{\partial y} = g\beta(C - C_\infty) + \nu \frac{\partial^2 u}{\partial y^2} + \frac{j_0 B_0}{\rho} \quad (6.113)$$

$$u \frac{\partial C}{\partial x} + v \frac{\partial C}{\partial y} = D \frac{\partial^2 C}{\partial y^2} \quad (6.114)$$

Equation (6.112) is the continuity equation, Equation (6.113) is the momentum equation, and Equation (6.114) is the species transport equation. In these equations u and v are the x and

y components of velocity, x is the distance up the electrode, y is the distance to the electrode surface, C is the concentration, C_∞ is the concentration of hydrogen in the bulk electrolyte, g is the acceleration due to gravity, ν is the kinematic viscosity, j_0 is the current density, B_0 is the magnetic field strength, D is the diffusion coefficient and ρ is the density. The fluid flow and mass transport situation is shown schematically in Figure 6.9.

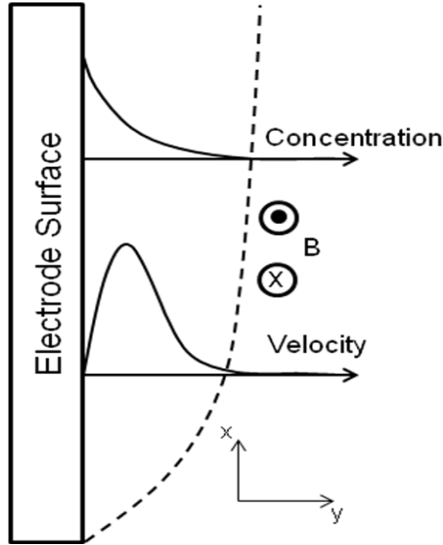


Figure 6.9: This shows a schematic of a natural convective boundary layer on a vertical electrode. The magnetic field is parallel to the electrode surface.

6.5.2 Mathematical Formulation of the Scaling Solution

The velocity field is caused in free convection by the concentration field. Therefore, the concentration boundary layer thickness δ can be used as the length scale that characterizes both the velocity and concentration fields. Denoting the velocity scale in the x direction by u_0 , the continuity equation shows that the velocity scale v_0 in the y direction is of the order of $u_0 \delta / x$ as shown below. Defining the following scales

$$\hat{x} = \frac{x}{x_L} \quad \text{and} \quad \hat{y} = \frac{y}{\delta} \quad (6.115)$$

the individual terms in the continuity equation can be written as

$$\frac{\partial u}{\partial x} \approx \frac{u_0}{x_L} \quad (6.116)$$

$$\frac{\partial v}{\partial y} \approx \frac{v_0}{\delta} \quad (6.117)$$

this gives an order of magnitude algebraic expression for the continuity equation

$$\frac{u_0}{x_L} + \frac{v_0}{\delta} = 0 \quad (6.118)$$

solving for v_0 gives an order of magnitude estimate for the velocity scale in the y direction

$$v_0 \approx \frac{u_0 \delta}{x_L} \quad (6.119)$$

replacing x_L , the distance up the electrode, by x gives the final form of the velocity scale in the in the y direction as

$$v_0 \approx \frac{u_0 \delta}{x} \quad (6.120)$$

the terms of Equations (6.113) and (6.114) can be evaluated by replacing u and ∂u by u_0 , ∂x by x , ∂y by δ , ∂C and $C - C_\infty$ by $\Delta C = C_w - C_\infty$ where C_w is the concentration at the surface of the electrode. Making these substitutions leads to the following set of equations

$$u \frac{\partial u}{\partial x} + v \frac{\partial u}{\partial y} \approx u_0 \frac{u_0}{x} + \frac{u_0 \delta}{x} \frac{u_0}{\delta} \approx \frac{u_0^2}{x} + \frac{u_0^2}{x} = \frac{u_0^2}{x} \quad (6.121)$$

$$v \frac{\partial^2 u}{\partial y^2} \approx v \frac{u_0}{\delta^2} \quad (6.122)$$

$$D \frac{\partial^2 C}{\partial y^2} \approx D \frac{\Delta C}{\delta^2} \quad (6.123)$$

$$u_0 \frac{\partial C}{\partial x} + v \frac{\partial C}{\partial y} \approx u_0 \frac{\Delta C}{x} + \frac{u_0 \delta}{x} \frac{\Delta C}{\delta} \approx \frac{u_0 \Delta C}{x} \quad (6.124)$$

Following the methods developed by Ruckenstein, (1987) each term in the transport equations is replaced by the evaluations given in Equation (6.121) – (6.124) multiplied by a constant to give a set of algebraic equations

$$A_1 \left(\frac{u_0^2}{x} \right) + B_1 \left(v \frac{u_0}{\delta^2} \right) = g \beta \Delta C + \frac{j_0 B_0}{\rho} \quad (6.125)$$

$$C_1 \left(\frac{u_0}{x} \right) = \frac{D}{\delta^2} \quad (6.126)$$

where A_1 , B_1 , and C_1 are all constants. An expression for the boundary layer thickness can be found by eliminating u_0 from Equations (6.125) and (6.126). Solving for u_0 in Equation (6.126) and substituting the expression into Equation (6.125) gives the following expression for the boundary layer thickness

$$\delta^4 = \frac{D^2 x [A + B Sc]}{\left(g \beta \Delta C + \frac{j_0 B_0}{\rho} \right)} \quad (6.127)$$

Rearranging Equation (6.127) to get

$$\left(\frac{g \beta \Delta C}{D} + \frac{j_0 B_0}{\rho D} \right) \left(\frac{1}{D} \right) [A + B Sc]^{-1} = \frac{x}{\delta^4} \quad (6.128)$$

the local mass transfer coefficient is defined as

$$h = \frac{k}{\delta} \quad (6.129)$$

raising everything in Equation (6.129) to the fourth power and solving for $1/\delta^4$ gives

$$\frac{h^4}{k^4} = \frac{1}{\delta^4} \quad (6.130)$$

substituting Equation (6.130) into Equation (6.128), and multiplying by x^3 gives

$$\left(\frac{g \beta \Delta C x^3}{D} + \frac{j_0 B_0 x^3}{\rho D} \right) \left(\frac{1}{D} \right) [A + B Sc]^{-1} = \frac{h^4 x^4}{k^4} \quad (6.131)$$

since the Sherwood number is defined $h x / k$, Equation (6.131) can be rewritten as

$$\left(\frac{g \beta \Delta C x^3}{D} + \frac{j_0 B_0 x^3}{\rho D} \right) \left(\frac{1}{D} \right) [A + B Sc]^{-1} = Sh^4 \quad (6.132)$$

the final form of the transport correlation is obtained

$$Sh = [Ra + \Omega]^{1/4} Sc^{1/4} [A + B Sc]^{-1/4} \quad (6.133)$$

to obtain an equation that predicts the effect of a magnetic on the limiting current density, the Sherwood number is rewritten as

$$Sh = \frac{j_L L}{n F D C_0} \quad (6.134)$$

where j_L is the limiting current density, L is the length of the electrode, n is the number of electrons involved in the reaction, F is Faraday's constant, D is the diffusion coefficient, and C_0 is the bulk concentration. Solving for j_L gives an equation that provides a prediction for the effect of a magnetic field on the limiting current density

$$j_L = \frac{n F D}{L} [Ra + \Omega]^{1/4} Sc^{1/4} [A + B Sc]^{-1/4} C_0 \quad (6.135)$$

where Ra is the Rayleigh number, Sc is the Schmidt number, and A and B are constants. In summary, three equations have been proposed that can be used to predict boundary layer thickness, enhancement of mass transport due to a magnetic field, and limiting current density.

These equations are given below

$$\delta = \left[D^2 x \right]^{1/4} \left[A + B Sc \right]^{1/4} \left[g \beta \Delta C + \frac{j_0 B_0}{\rho} \right]^{-1/4} \quad (6.136)$$

$$Sh = \left[Ra + \Omega \right]^{1/4} Sc^{1/4} \left[A + B Sc \right]^{-1/4} \quad (6.137)$$

$$j_L = \frac{n F D}{L} \left[Ra + \Omega \right]^{1/4} Sc^{1/4} \left[A + B Sc \right]^{-1/4} C_0 \quad (6.138)$$

6.6 Discussion of the Modeling Results

In this section the three fluid flow models will be discussed. For the first model the Adomian Decomposition method was used to solve a magnetohydrodynamic fluid flow problem with a nonlinearly varying magnetic field. In the second model, the Adomian Decomposition method was used to solve a coupled fluid flow and mass transport problem at a vertical electrode with a constant magnetic field applied parallel to the electrode surface. In the third model, scaling analysis was used to derive equations that predict boundary layer thickness, mass transport enhancement due to a magnetic field, and the limiting current density.

6.6.1 Discussion of Nonlinearly Varying Magnetic Field Model

For this model, the system of equations given by Equations (6.1) and (6.2) were solved using the Adomian Decomposition method (ADM). Equations (6.1) and (6.2) are the governing equations for magnetohydrodynamic fluid flow over a flat plate with a nonlinearly varying magnetic field. Equations (6.1) and (6.2) were transformed into Equation (6.10) by a similarity transformation. Equation (6.10) is third order nonlinear ordinary differential equation.

The reasons for modeling this fluid flow situation are three fold: (1) introduce the ADM, (2) discuss the effect of a magnetic field on transport properties, and (3) the modeling results can be compared to an exact solution. The exact solution to Equation (6.10), for $\beta = 1$ is given by

$$f(\eta) = \frac{1 - \exp\left(-\sqrt{1+M} \eta\right)}{\sqrt{1+M}} \quad (6.139)$$

as can be seen in Figures 6.1, 6.2, 6.3, 6.4 and Tables 6.1 and 6.2 the analytical results are in very good agreement to the exact solution. For certain values of β and M the analytical solution shows a limited range stability, see Figure 6.5. The stability problem at larger values of β and M could possible by solved by including additional terms in the ADM series solution.

The main results from this model are given in Figures 6.10 and 6.11. Figure 6.10 shows the magnetohydrodynamic boundary layer profiles for fluid flow over a flat plate. A magnetic field applied to a flow field acts to decrease the boundary layer thickness. As can be seen in Figure 6.10, with increasing values of M , the boundary layer profile flattens out. Figure 6.11 gives the velocity profiles for magnetohydrodynamic fluid for over a flat plate. The application of a magnetic field reduces the velocity profiles which are a consequence of the Lorentz force.

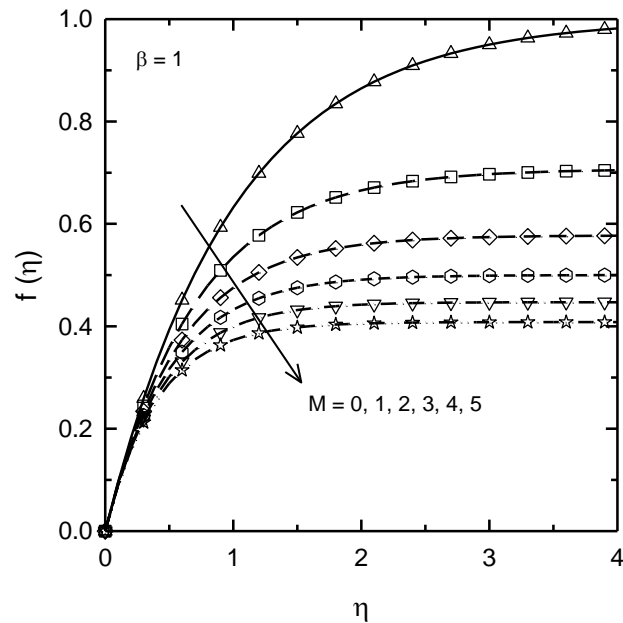


Figure 6.10: This plot gives the boundary layer profiles for a nonlinearly varying magnetic field over a flat plate at $\beta = 1$ and $M = 0, 1, 2, 3, 4,$ and 5 (increasing in the direction of the arrow).

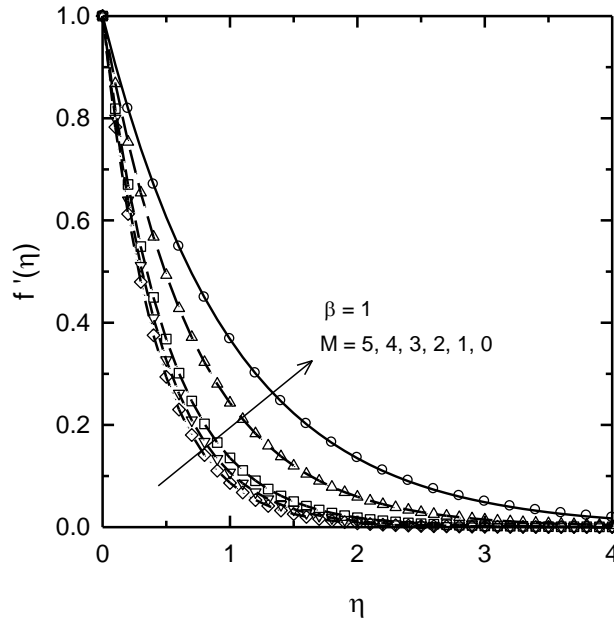


Figure 6.11: This plot gives the velocity profiles for a nonlinearly varying magnetic field over a flat plate at $\beta = 1$ and $M = 5, 4, 3, 2, 1$ (decreasing in the direction of the arrow).

6.6.2 Discussion of the Coupled fluid flow and Mass Transport Model

Equations (6.52) – (6.53) govern the coupled fluid flow and mass transport at a vertical electrode with a magnetic field applied parallel to the electrode surface. Equations (6.52) – (6.53) were transformed into Equations (6.58) and (6.59) by a similarity transformation. The similarity transformation was first derived by Levich (1962) and then modified by Fahidy (1973) to account for a magnetic field. In the work by Fahidy, a perturbation technique was used to arrive at first order estimates for the concentration profiles, velocity profiles, and limiting current density.

This modeling work built upon the work by Fahidy to obtain higher order estimates of the effect of a magnetic field on the concentration profiles, and velocity profiles. This objective was achieved and the modeling results showed enhanced mass transport to the metal/electrolyte interface when the magnetic field is applied parallel to the electrode surface. The limitation to this modeling work lies in the fact that the solutions for the concentration field and velocity field do not satisfy the boundary conditions at infinity

$$f'(\eta \rightarrow \infty) = 0 \quad (6.140)$$

$$\phi(\eta \rightarrow \infty) = 0 \quad (6.141)$$

However, this is not a limitation of the Adomian Decomposition method; this is due to the fact that no similarity solution exists for a constant magnetic field Gebhart et al. (1988).

6.6.3 Discussion of the Scaling Analysis Model

For this model scaling analysis was performed on Equations (6.112) – (6.114) to obtain relationships for the effect of a magnetic field on the limiting current density, mass transport, and the boundary layer thickness. The scaling techniques used to obtain these scaling approximations are based upon methods developed by Ruckenstein (1987). The scaling approximations are given below

$$\delta = [D^2 x]^{1/4} [A + B Sc]^{1/4} \left[g \beta \Delta C + \frac{j_0 B_0}{\rho} \right]^{-1/4} \quad (6.142)$$

$$Sh = [Ra + \Omega]^{1/4} Sc^{1/4} [A + B Sc]^{-1/4} \quad (6.143)$$

$$j_L = \frac{n F D}{L} [Ra + \Omega]^{1/4} Sc^{1/4} [A + B Sc]^{-1/4} C_0 \quad (6.144)$$

Equation (6.142) gives the scaling approximation for boundary layer thickness. Equation (6.143) gives the Sherwood number in terms of the Rayleigh number, Schmidt number, the magnetic parameter, and two constants A and B. Equation (6.143) gives the scaling approximation for the effect of a magnetic field on the limiting current density. Equation (6.142) shows that the magnetic field acts to decrease the thickness of the boundary layer; this effect can be seen in the term in the last set of brackets. Equation (6.143) shows that a magnetic enhances mass transport to the metal/electrolyte interface. Equation (6.144) predicts that a magnetic field will increase the limiting current density. The enhancement in transport properties can be attributed to the Lorentz force.

The two constants A and B are undetermined since two limiting cases could not be found in the literature for mass transport at a vertical electrode in the presence of a magnetic field. The methodology for determining the constants A and B is the following: (1) find two relationships in the literature, and take the limit as Sc number goes to infinity and zero, (2) solve the system of equations for which there are two equations and two unknowns. The result of this analysis would give the numeric values of A and B.

The parameter Ω is a dimensionless number that is a result of this scaling analysis. It is defined as

$$\Omega = \frac{j_0 B_0 x^3}{\rho D \nu} \quad (6.145)$$

where j_0 is the current density, B_0 is the magnetic field strength, x is the length of the electrode, ρ is the density, D is the diffusion coefficient, and ν is the kinematic viscosity (momentum diffusivity). Therefore, this parameter is a ratio of the Lorentz force to diffusive forces. Equation (2.143) could be written more generally as

$$\Omega = \frac{j_0 B_0 H^3}{\rho D \nu} \quad (6.146)$$

where H is the height of the electrode. In conclusion, it was shown that a magnetic field decreases the boundary layer thickness, enhances mass transport, and increases the limiting current density. The changes in transport behavior can be attributed the Lorentz force.

CHAPTER 7

CONCLUSIONS AND FUTURE WORK

7.1 Introduction

At the end of Chapter 2 a list of questions were given which served as a guide to experimentation and inquiry throughout the course of this research project. In this Chapter, the answers to these questions will be provided and will serve as the conclusions to this research project.

7.2 Answers to the Guiding Questions

The driving force behind this research project was to gain a fundamental understanding of the effect of a magnetic field on the hydrogen absorption and corrosion behavior of API X80, X70, and X52 linepipe steel grades. To that end, a set of fundamental questions were formulated

1. Why does there exist a discrepancy in the hydrogen charging data obtained by Sanchez and that obtained by the author when the experimental conditions were identical?

The experimental conditions used in this research approximated those used by Sanchez (2005) as closely as possible. However, the main difference in experimental setup is the strength of the magnetic field. Sanchez used a magnetic field strength of 2.0 Tesla, while the maximum magnetic field strength used in this research was 0.7 Tesla. It is believed that this is one of the main reasons for the discrepancy in experimental data. The other would be the formation of a cathodic film during the hydrogen charging experiments.

2. What effect would changing the magnetic field strength have on the hydrogen absorption behavior of high-strength linepipe steel?

The data given in Figure 7.1 shows the hydrogen content in API X80 linepipe steel increasing with increasing magnetic field strength. A reason for the increase in hydrogen content with increasing magnetic field strength could be due to the increase in magnetostatic energy. The energy stored per unit volume (magnetostatic energy) is given below

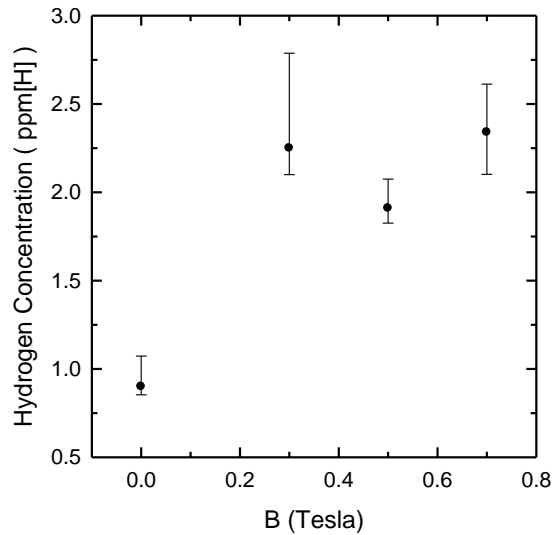


Figure 7.1: Plot showing hydrogen concentration as a function of magnetic field strength. The magnetic field strength was varied from 0.0 to 0.7 Tesla. A magnetic field strength of 0.7 Tesla alters the hydrogen absorption behavior most significantly. This data is for API X80 linepipe steel in 1 N H₂SO₄.

$$E = \frac{1}{2 \mu_0} N I^2 v \quad (7.1)$$

where μ_0 is the permeability of free space, N is the magnetizing factor, I is the intensity, and v is the volume of the magnetic body, Chikazumi (1997).

3. What is the effect of temperature on hydrogen absorption?

The temperature effect could not be assessed due to complications in experimental setup. At elevated temperatures, the water in the sulfuric acid solution boils off, and the solution becomes more concentrated as time progresses. The end result is dissolution of the steel sample into the solution not allowing a hydrogen concentration measurement to be obtained.

4. What is the effect of stress on hydrogen absorption?

From the data given in Figure 7.2 it can be seen that there is no real correlation between hydrogen content and stress.

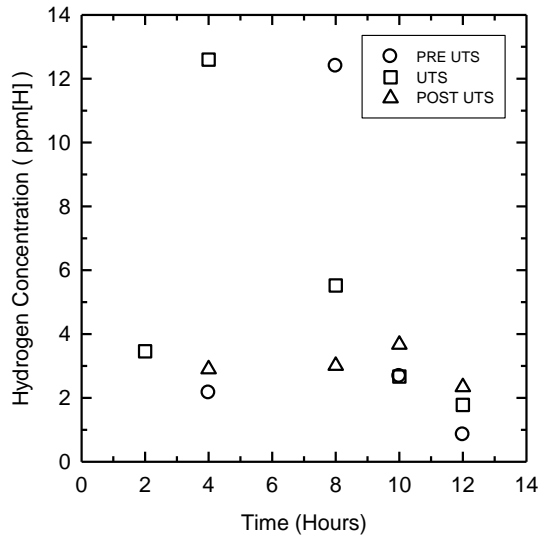


Figure 7.2: Comparison plot of all Hydrogen charging results for X80 high-strength linepipe steel in 1 N H₂SO₄. This plot shows total hydrogen concentration as a function of time. All of the stress levels are represented on this plot.

5. Does a magnetic field alter the electron transfer kinetics associated with the electrochemical processes occurring on the sample surface?

Yes. The effect of a magnetic field on electron transfer processes is evident from the Nyquist plots show below in Figure 7.3(a). Figure 7.3(a) shows one capacitive loop which is indicative of a charge transfer reaction. The charge transfer reaction is the reduction of hydrogen occurring on the surface of the electrode. The capacitive loops also indicate that passivating film has formed at cathodic potentials. This is important since it is believed that a passive film is responsible for the erratic hydrogen charging behavior. There is experimental evidence of cathodic film formation from X-ray electron spectroscopy and Auger electron spectroscopy experiments. Figure 7.3(b) gives the charge transfer resistance as a function of magnetic field strength. Charge transfer resistance is inversely proportional to the exchange current density. The exchange current density is a measure of the kinetics at equilibrium.

Figure 7.4 shows i_{CORR} as a function of magnetic field strength. This shows that a magnetic field decreases the corrosion current up to 0.5 Tesla and then increases again a 0.7 Tesla.

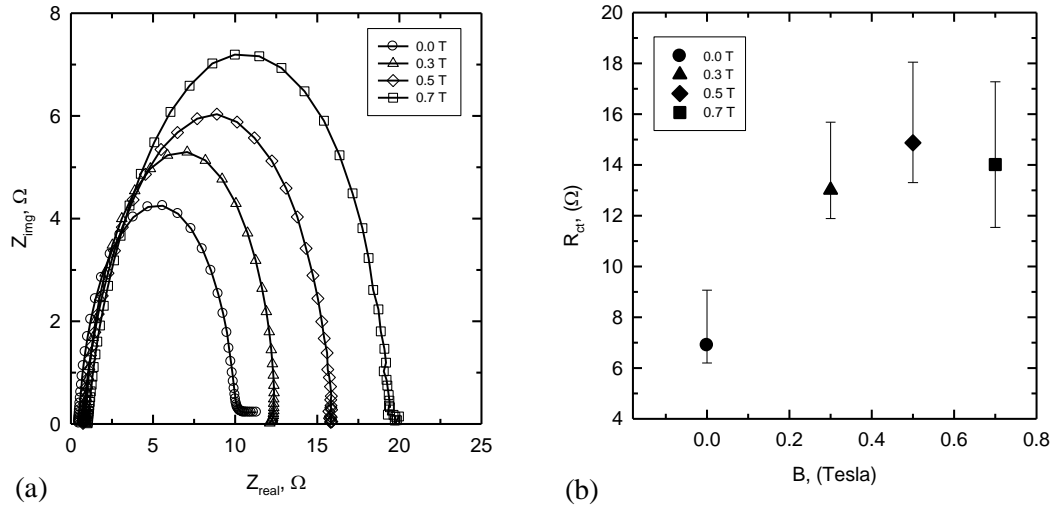


Figure 7.3: These figures show; (a) Nyquist plots of API X80 linepipe steel at different magnetic field strengths, (b) variation in charge transfer resistance with magnetic field strength of API X80 linepipe steel.

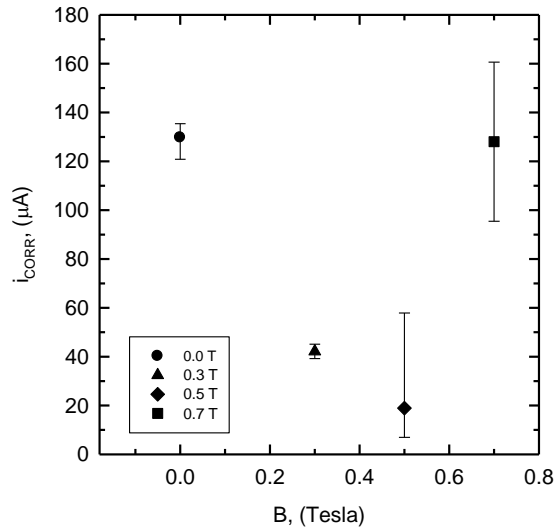


Figure 7.4: This is a plot of corrosion current as a function of magnetic field strength for API X80 linepipe steel in 1 N H_2SO_4 .

6. Why is there no observable potential shift in the potentiodynamic polarization curve at the open circuit potential (OCP) but the OCP is known to shift, from OCP measurements, when a magnetic is present in the electrochemical system?

The first part of this statement is not true. There is an observable shift in the potentiodynamic polarization curve with applied magnetic field, as shown in Figure 7.5. The shift in OCP can be explained by the following thermodynamic equation

$$E = E^0 - \frac{R T}{n F} \ln[H^+] - \frac{\Delta M B}{n F} \quad (7.2)$$

where $\Delta M B$ is the magnetic work term responsible for the potential shift in the OCP.

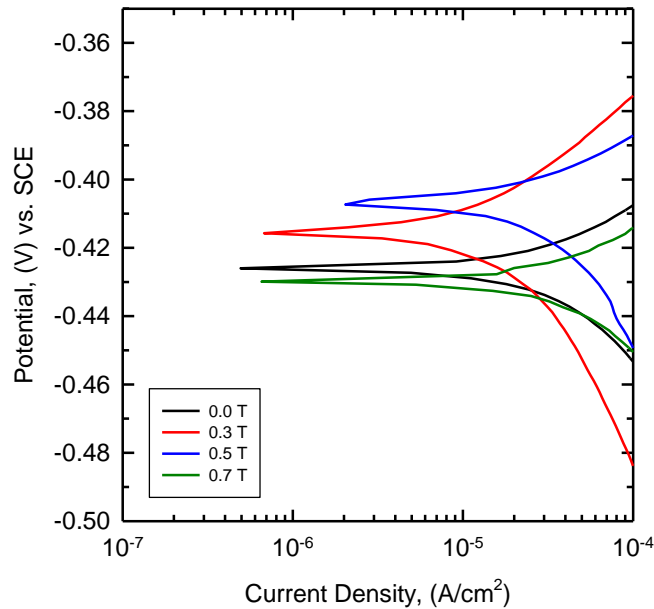


Figure 7.5: This plot shows the variation in open circuit potential and corrosion current with applied magnetic field.

7. Why does the passivation potential of the API X80 linepipe steel sample change when a magnetic field is present in the electrochemical cell?

The shift in passivation potential can be attributed to magneto-convection created by the Lorentz force, the concentration gradient force, and the magnetic field gradient force. These magnetic forces act to eliminate concentration gradients in the solution adjacent to the

electrode surface. Elimination of concentration gradients promotes anodic dissolution of the iron electrode, which results in a positive shift in the passivation potential and an increase in the critical current density. The most dominant of these forces is the Lorentz force. The Lorentz force is directly proportional to the current density and therefore regions where the Lorentz force is strong can be tracked along the polarization curve, as can be seen in Figure 7.6. Figure 7.6 shows that the Lorentz force is strongest at the passivation potential.

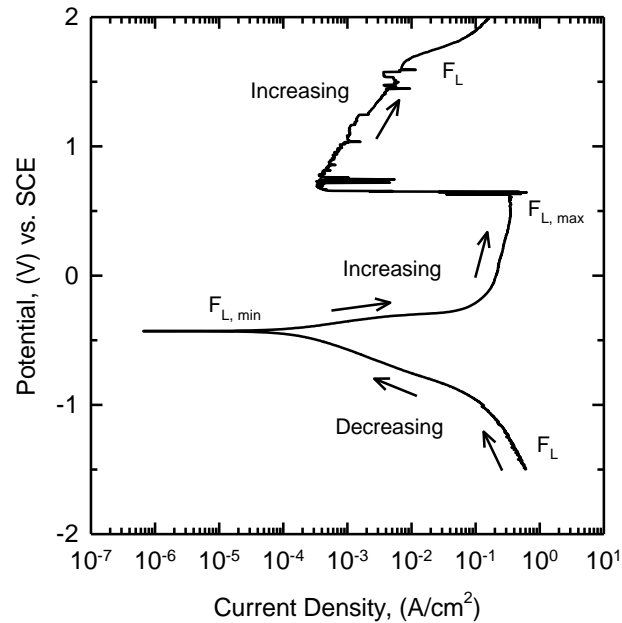


Figure 7.6: Potentiodynamic polarization curve for API X80 at a magnetic field strength of 0.7 Tesla. F_L represents the Lorentz force and this schematic shows regions on the polarization curve where the Lorentz force is dominant. On the anodic branch, the Lorentz force is greatest at the passivation potential.

8. What is the nature of the passivating film that forms during cathodic hydrogen charging experiments?

The cathodic film is composed of FeO, Fe₂O₃, and FeSO₄ which was verified by X-ray photoelectron spectroscopy (XPS) and Auger electron spectroscopy (AES).

9. What is the fluid flow and mass transport behavior of the electrolyte next to the sample surface and what does this mean in terms of hydrogen absorption?

Three fluid flow models were solved in order to gain insight into the fluid flow and mass transport behavior in the presence of a magnetic field. Two models were solved by the Adomian Decomposition method to show that a magnetic field enhanced mass transport. The third model was solved using scaling analysis techniques. The third model gave the most important results, which are given below

$$\delta = [D^2 x]^{1/4} [A + B Sc]^{1/4} \left[g \beta \Delta C + \frac{j_0 B_0}{\rho} \right]^{-1/4} \quad (7.3)$$

$$Sh = [Ra + \Omega]^{1/4} Sc^{1/4} [A + B Sc]^{-1/4} \quad (7.4)$$

$$j_L = \frac{n F D}{L} [Ra + \Omega]^{1/4} Sc^{1/4} [A + B Sc]^{-1/4} C_0 \quad (7.5)$$

Equation (7.3) shows that a magnetic decreases boundary layer thickness. Equation (7.4) predicts that a magnetic field enhances mass transport. Equation (7.5) shows that a magnetic field increases the limiting current density. Another important aspect of this scaling analysis is the appearance of the dimensionless number Ω . Ω is given by the following relationship

$$\Omega = \frac{j_0 B_0 H^3}{\rho D \nu} \quad (7.6)$$

Ω is a ratio of the Lorentz force to diffusive forces (mass diffusion and momentum diffusion).

Equations (7.3) – (7.5) show unequivocally that a magnetic field enhances mass transport to the electrode/electrolyte interface. In terms of hydrogen absorption, this means that there is always a supply of hydrogen ions that can participate in the hydrogen reduction reaction. Therefore, from a mass transport perspective, the scaling analysis model provides a reason as to how a magnetic field could increase hydrogen absorption.

7.3 Future Work

There are two main areas of this research that need to be investigated more thoroughly: (1) the formation of passive films at cathodic potentials, and (2) the effect of a magnetic field on electrode kinetics. The formation of a passive film at cathodic potentials was first observed by

Jackson, (2008). From SEM analysis, Jackson was able to look at the morphology of the passivating film. For this research, X-ray photoelectron spectroscopy (XPS) and Auger electron spectroscopy (AES) was used to show that the film was composed of FeO, Fe₂O₃, and FeSO₄. However, other than composition, nothing conclusive can be said about the thickness of the film due to difficulties in sample extraction. From the electrochemical impedance spectroscopy experiments it was also shown that a passivating film exists at cathodic potentials. The experimental work that needs to be done to characterize the passive film more accurately are additional SEM, XPS, and AES experiments.

It was shown in this research that a magnetic field changes the kinetics of the system, see Figures 7.3 and 7.4. An accurate kinetic theory of any process must, in the limit of equilibrium, give an equation of thermodynamic form and for electrode reactions, equilibrium is given by the Nernst equation, Bard et al. (2002). As a starting point to developing a kinetic theory for the effect of a magnetic field on electrode reactions, one could start with Equation (7.2)

$$E = E^0 - \frac{R T}{n F} \ln[H^+] - \frac{\Delta M B}{n F} \quad (7.7)$$

rewriting Equation (7.7) as

$$E = E^0 + \frac{R T}{n F} \ln \frac{[H]}{[H^+]} - \frac{\Delta M B}{n F} \quad (7.8)$$

it should be noted that all terms in Equation (7.8) have units of volts. Rearranging Equation (7.8) further to show

$$E - E^0 + \frac{\Delta M B}{n F} = \frac{R T}{n F} \ln \frac{[H]}{[H^+]} \quad (7.9)$$

defining a new variable, η which incorporates the potential shift due to a magnetic field and letting $n = 1$ the following equation is obtained

$$\eta_{MAG} = E - E^0 + \frac{\Delta M B}{F} \quad (7.10)$$

$$\eta_{MAG} = \frac{R T}{F} \ln \frac{[H]}{[H^+]} \quad (7.11)$$

multiplying both sides of Equation (7.11) by $F/R T$ and letting $f = F/R T$ gives

$$f \eta_{MAG} = \ln \frac{[H]}{[H^+]} \quad (7.12)$$

taking the exponential to both sides of Equation (7.12) gives

$$\exp(f \eta_{MAG}) = \frac{C_H}{C_{H^+}} \quad (7.13)$$

Equation (7.13) is nothing more than the exponential form of the Nernst equation. Continuing with this analysis, it would be logical to assume that Equation (7.13) could be put into the form of the Butler-Volmer equation

$$i = i_0 \left(\exp \left[\frac{\eta_{MAG}}{\beta_a} \right] - \exp \left[-\frac{\eta_{MAG}}{\beta_c} \right] \right) \quad (7.14)$$

or

$$i = i_0 \left(\exp \left[\frac{\left(E - E^0 + \frac{\Delta M B}{F} \right)}{\beta_a} \right] - \exp \left[-\frac{\left(E - E^0 + \frac{\Delta M B}{F} \right)}{\beta_c} \right] \right) \quad (7.15)$$

where $\beta_a = R T / \alpha n F$ and $\beta_c = R T / (1 - \alpha) n F$ it is also assumed that the solution is well stirred so that the surface concentration and bulk concentration are approximately the same. As a first approximation, Equation (7.15) appears to capture the physics and also satisfy the criterion stated by Bard et al. (2002): when $B = 0$, the normal form of the Nernst and Butler – Volmer equations are obtained.

REFERENCES CITED

- Aaboubi, O.; Chopart, J. P.; Olivier, A.; Los, P.: "Magnetohydrodynamic transfer function applied to ultramicroelectrode systems", *Energy Conversion and Management*, p. 373-381, 43 (2002).
- Atherton, D. L.; Daly, M. G.: "Finite element calculations of magnetic flux leakage detector signals", *NDT International*, p. 235-238, (20)4 (1987).
- Barbier, F.; Alemany, A.; Martemianov, S.: "On the Influence of a high magnetic field on the corrosion and deposition processes in the liquid Pb-17Li alloy", *Fusion Engineering and Design*, p. 199-208, 43 (1998).
- Bard, A. J. and Faulkner, L. R.: "Electrochemical Methods: Fundamentals and Applications", John Wiley & Sons, 2001.
- Beachem, C. D.: "Hydrogen Damage", American Society for Metals (1977).
- Bockris, J. O'M; Reddy, A. K. N.: *Modern Electrochemistry*, vol. 2, Macdonald & Co. Ltd., 1970.
- Boum, N. G. B.; Alemany, A.: "Numerical simulations of electrochemical mass transfer in electromagnetically forced channel flows", *Electrochimica Acta*, p. 1749-1760, 44 (1999).
- Bund, A.; Koehler, S.; Kuehnlein, H.H.; Plieth, W.: "Magnetic field effects in electrochemical reactions", *Electrochimica Acta*, p. 147-152, 49 (2003).
- Chaudhari, B. S.; Radhakrishnan, T. P.: "Evaluation of Hydrogen Diffusivity in Mild Steel from Electropermeation Transients under Conditions of Galvanostatic Charging", *Surface and Coatings Technology*, p. 261-280, 28 (1986).
- Chopart, J. P.; Aaboubi, O.; Merieene, E.; Olivier, A.; Amblard, J.: "MHD-control on limiting Faradaic currents", *Energy Conversion and Management*, p. 365-371, 43 (2002).
- Chouchane, S.; Levesque, A.; Douglade, J.; Rehamnia, R; Chopart, J. P.: "Microstructural analysis of low Ni content Zn alloy electrodeposited under applied magnetic field", *Surface and Coatings Technology*, p. 6212-6216, 201 (2007).
- Davidson, P. A.: "An Introduction to Magnetohydrodynamics", Cambridge Texts in Applied Mathematics, Cambridge University Press, 2001.
- Dey, S; Mandhyan, A. K.; Sondhi, S. K.; Chattoraj, I.: "Hydrogen Entry into pipeline steel under freely corroding conditions in two corroding media", *Corrosion Science*, p. 2676-2688, 48 (2006).

- Dong, C. F.; Liu, Z. Y.; Li, X. G.; Cheng, Y. F.: "Effects of hydrogen-charging on the susceptibility of X100 pipeline steel to hydrogen-induced cracking", *International Journal of Hydrogen Energy*, p. 9879-9884, 34 (2009).
- Dong, C. F.; Li, X. G.; Liu, Z. Y.; Zhang, Y. R.: "Hydrogen-induced cracking and healing behavior of X70 steel", *Journal of Alloys and Compounds*, p. 966-972, 484 (2009).
- Esmailzadeh, F.; Mowla, D.; Asemani, M.: "Mathematical Modeling and Simulation of Pigging Operation gas and liquid pipelines", *Journal of Petroleum Science and Engineering*, p. 100-106, 69 (2009).
- Fahidy, T. Z.: "Hydrodynamic Models in Magneto-electrolysis", *Electrochimica Acta*, p. 607-614, 18 (1973).
- Fahidy, T. Z.: "Wave Phenomena in Magneto-electrolytic Systems", *Electrochimica Acta*, p. 21-24, 21 (1974).
- Fahidy, T. Z.: "Magneto-electrolysis in Steady Hartmann-Flow Cells", *The Chemical Engineering Journal*, p. 23-28, 12 (1976).
- Fahidy, T. Z.: "The Application of Plasma Dynamics to the study of Flow Generation in Magneto-electrolysis", *Electrochimica Acta*, p. 549-555, 23 (1978).
- Fahidy, T. Z.: "Experimental verification of an estimation method for mass transport in magneto-electrolysis", *The Chemical Engineering Journal*, p. 245-246, 17 (1979).
- Fahidy, T. Z.: "On the Optimization of a certain class of Magneto-electrolytic Reactors", *Electrochimica Acta*, p. 1907-1909, 13 (1991).
- Fahidy, T. Z.: "On the magnetohydrodynamics of natural convective diffusion boundary layers in coupled horizontal electric and magnetic fields", *Chemical Engineering Journal*, p. 79-82, 72 (1999).
- Fahidy, T. Z.: "Characteristics of surfaces produced via Magneto-electrolytic deposition", *Progress in Surface Science*, p. 155-188, 68 (2001).
- Faulkner, F. R.: "Get this title", *Journal of Chemical Education*, (60)262, (1983).
- Hiltscher, G; Muhlthaler, W; and Smits, J: "Industrial Pigging Technology", Wiley-VCH, 2003.
- Hopkins, P.: "Transmission Pipelines: how to improve their integrity and prevent failures", In Denys R, editor Pipeline technology. Proceedings of the 2nd international pipeline technology conference, p. 683-706 1 (1995).
- Interrante, C. G.; Pressouyre, G. M.: "Current Solutions to Hydrogen Problems in Steels", Proceedings of the First International Conference. 1982.
- Ispas, A; Matsushima, H.; Plieth, W.; Bund, A.: "Influence of a magnetic field on the electrodeposition of nickel iron alloys", *Electrochimica Acta*, p. 2785-2795, 52 (2007).

- Jiles, D. C.: "Review of magnetic methods for nondestructive evaluation", *NDT International*, p. 311-319, (21)5, (1988).
- Kim, K.; Fahidy, T. Z.: "On the numerical solution of an electrolytic convective-diffusion problem in an externally imposed force field", *Chemical Engineering Journal*, p. 69-72, 68 (1997).
- Koza, J. A.; Uhlemann, M.; Mickel, C.; Gebert, A.; Schultz, L.: "The effect of magnetic field on the electrodeposition of CoFe Alloys", *Journal of Magnetism and Magnetic Materials*, p. 2265-2268, 321 (2009).
- Krause, A.; Koza, J.; Ispas, A.; Uhlemann, M.; Gebert, A.; Bund, A.: "Magnetic field induced micro-convective phenomena inside the diffusion layer during the electrodeposition of Co, Ni, and Cu", *Electrochimica Acta*, p. 6338-6345, 52 (2007).
- Krause, T. W.; Mandal, K.; Hauge, C.; Weyman, P.; Sijgers, B.; Atherton, D. L.: "Correlation between magnetic flux leakage and magnetic Barkhausen noise: Stress dependence in pipeline steel", *Journal of Magnetism and Magnetic Materials*, p. 207-219, 169 (1997).
- Krause, T. W.; Donaldson, R. M.; Barnes, R.; Atherton, D. L.: "Variation of the stress dependent magnetic flux leakage signal with defect and flux density", *NDT & E International*, p. 79-86, (29)2, (1996).
- Legeai, S.; Chatelut, M.; Vittori, O.; Chopart, J. P.; Asboubi, O.: "Magnetic field influence on mass transport phenomena", *Electrochimica Acta*, p.51-57, 50 (2004).
- Levensque, A.; Chouchane, S.; Douglade, J.; Rehamnia, R.; and Chopart, J. P.: "Effect of natural and magnetic convection on the structure of electrodeposited zinc-nickel alloy", *Applied Surface Science*, p. 8040-8053, 255 (2009).
- Leventis, N.; and Gao, X.: "Magnetohydrodynamic Electrochemistry in the Field of Nd-Fe-B Magnets: Theory, Experiment, and Application in Self-Powered Flow Delivery Systems", *Analytical Chemistry*, p. 3981-3992, 73 (2001).
- Lorbeer, P.; Lorentz, W. J.: "The Kinetics of iron dissolution and passivation", *Passivation of Metals*, Electrochemistry Society, Princeton, NJ, (1978).
- Lu, Z.; Huang, D.; Yang, W.; Congleton, J.: "Effects of an applied magnetic field on the dissolution and passivation of iron in sulphuric acid", *Corrosion Science*, p. 2233-2249, 45 (2003).
- Lu, Z.; Yang, W.: "In situ monitoring the effects of a magnetic field on the open-circuit corrosion rates of iron in acidic and neutral solutions", *Corrosion Science*, p. 510-522, 50 (2008).
- Lu, Z.; Huang, D.; Yang, W.: "Probing into the effects of a magnetic field on the electrode processes of iron in sulphuric acid solutions with dichromate based on the fundamental electrochemistry kinetics", *Corrosion Science*, p. 1471-1492, 47 (2005).
- McMurry, J.; Fay, R. C.: "Chemistry", Third Edition, Prentice Hall, 2001.

- Mohanta, S.; Fahidy, T. Z.: "Magnetoelectrolysis with Rough Cathode Surfaces", *Electrochimica Acta*, p. 771-775, 19 (1974).
- Mohanta, S.; Fahidy, T. Z.: "Mass Transfer in Cylindrical Magnetoelectrolytic Cells", *Electrochimica Acta*, p. 149-152, 21 (1976).
- Mohanta, S.; Fahidy, T. Z.: "The Effect of a Magnetic Field on Electrolyte Conductivity", *Electrochimica Acta*, p. 25-27, 21 (1976).
- Mori, S.; Kumita, M.; Schichida, S.; Shigaki, H.: "Mass Transfer enhancement during electrolysis with cylindrical electrodes by magnetic field exposure and its dependency on electrode positions", *Energy Conversion and Management*, p. 383-397, 43 (2002).
- Motoyama, M.; Fukunaka, Y.; Kikuchi, S.: "Bi electrodeposition under Magnetic Field", *Electrochimica Acta*, p. 897-905, 51 (2005).
- Muller, U; and Buhler, L: "Magnetofluidynamics in Channels and Containers", Springer-Verlag, 2001.
- Ohno, I.; Mukai, M.: "The effect of a Magnetic Field on the Electrodeposition of Iron-Nickel Alloy", *Electrodeposition and Surface Treatment*, p. 213-218, 3 (1975).
- Olden, V.; Thaulow, C.; Johnsen, R.: "Modelling of hydrogen diffusion and hydrogen induced cracking in supermartensitic and duplex stainless steels", *Materials and Design*, p. 1934-1948, 29 (2008).
- Pikas, J. L.: "In-line inspection of large diameter pipelines using enhanced collapsible pigs", *The NACE International Annual Conference and Exposition, Corrosion 96*, Paper No. 39 (1996).
- Quraishi, M. S.; Fahidy, T. Z.: "A flow visualization technique using analytical indicators: Theory and some applications", *Chemical Engineering Science*, p. 775-780, 37(5) (1982).
- Quraishi; M. S.; Fahidy, T. Z.: "The Effect of Magnetic Fields on Natural Convective Mass Transport at Inclined Circular Disk Electrodes", *Electrochimica Acta*, p. 591-599, 25 (1980).
- Rhen, F. M.; Coey, J. M. D.: "Magnetic Field Induced Modulation of Anodic Area: Rest Potential Analysis of Zn and Fe", *Journal of Physical Chemistry*, p. 3412-3416, 111 (2007).
- Shipilov, S. A.; Le May, I.: "Structural Integrity of aging buried pipelines having cathodic protection", *Engineering Failure Analysis*, p.1159-1176, 13 (2006).
- Snaskii, A. A.; Zhenirovskyy, M.; Meinert, D.; Schulte, M.: "An integral equation model for the magnetic flux leakage method", *NDT&E International*, 2010, doi:10.1016/j.ndteint.2010.01.008
- Stansbury, E.E., and Buchanan, R. A.: "Fundamentals of Electrochemical Corrosion", ASM International, 2000.
- Sterm, W.; Makrides, A. C.: "Electrode Assembly for electrochemical measurements", p. 782, 107 (1960).

- Tacken, R. A.; Janssen, L. J. J.: "Applications of Magneto-electrolysis", *Journal of Applied Electrochemistry*, p. 1-5, 25 (1995).
- Tolmasquim, S.T.; Nieckele, A.O.: "Design and Control of Pig Operations through Pipelines", *Journal of Petroleum Science and Engineering*, p. 102-110, 62 (2008).
- Tsukada, K.; Yoshioka, M.; Kawasaki, Y.; Kiwa, T.: "Detection of back-side pit on a ferrous plate by magnetic flux leakage method with analyzing magnetic field vector", *NDT&E International*, 2010, doi:10.1016/j.ndteint.2010.01.004
- Wassef, O.; Fahidy, T. Z.: "Magneto-electrolysis in the presence of bubble formation at the cathode", *Electrochimica Acta*, p. 727-730, 21 (1976).
- Waskass M; Kharkats, Y. I.: "Magnetoconvective Phenomena: A Mechanism for Influence of Magnetic Fields on Electrochemical Processes", *Journal of Physical Chemistry B*, p. 4876-4883, 103 (1999).
- Weier, T.; Huller, J.; Gerbeth, G.; Weiss, F. P.: "Lorentz force influence on momentum and mass transfer in natural convection copper electrolysis", *Chemical Engineering Science*, p. 293-298, 60 (2005).
- Weier, T.; Eckert, K.; Muhlenhoff, S.; Cierpka, C.; Bund, A.; Uhlemann, M.: "Confinement of paramagnetic ions under magnetic field influence: Lorentz versus concentration gradient force based explanations", *Electrochemistry Communications*, p. 2479-2483, 9 (2007).